

# Insights into the turbulent flow of dense gases through high-fidelity simulations

P. Cinnella<sup>a</sup>, X. Gloerfelt<sup>b</sup>

<sup>a</sup>Jean Le Rond D'Alembert Institute, Sorbonne University, 4 place Jussieu, Paris, 75005, , France  
<sup>b</sup>DynFluid Laboratory, Arts et Métiers Institute of Technology, 151 bd. de l'Hôpital, Paris, 75013, , France

---

## Abstract

This article reviews recent advances in the understanding of turbulent flows of non-ideal gases through the use of high-fidelity direct and large eddy simulations. In particular, the focus is on so-called dense gases, i.e. flows of organic vapours, which are characterised by moderate to high molecular complexity and weight, making them deviate from the thermophysical behaviour of a thermally and calorically perfect gas significantly. Dense gas flows, which are of interest for a wide range of applications, have been studied in particular because of their important role in several energy conversion systems. However, their behaviour in the transitional and turbulent regimes has long remained poorly understood due to the difficulty of performing detailed experiments on flows characterised by high density and temperature conditions. Recently, advances in high-fidelity numerical solvers for dense gases have made it possible to unravel the influence of complex thermodynamic effects and variations in transport properties on the hydrodynamic stability and transition to turbulence of dense gases, as well as on the dynamics of compressible turbulence. A variety of flow configurations, ranging from canonical flows to 3D turbine configurations, have then been studied, shedding light on the relevant physical mechanisms, but also allowing the evaluation of lower-fidelity models. The high-fidelity databases are also paving the way for the development of improved turbulence and transition models for non-ideal gases, and are expected to provide new impetus to the design of next-generation energy conversion systems.

**Keywords:** Dense gases, High-fidelity simulations

---

## 1. Introduction

In recent years, compressible flows of thermodynamically complex gases have received considerable attention in the scientific community. Applications range from energy production [1, 2, 3], to refrigeration [4, 5], and chemical processing [6]. Recent advances in computational fluid dynamics (CFD) as a fundamental research and design tool in aerodynamics and energetics have motivated the development of numerical solvers for non-reacting flows of gases operating in thermodynamic conditions deviating from the ideal-gas regime, i.e. flows of gases that do not follow the well-known  $p = \rho RT$  equation of state (with  $p$  the fluid pressure,  $\rho$  the density,  $T$  the absolute temperature and  $R$  the gas constant). The increasing number of applications of non-ideal gas flows has led to the development of a new branch of fluid mechanics called Non-Ideal Compressible Fluid Dynamics (NICFD), which is a very active area of research. This is evidenced, for example, by a successful series of conferences launched in 2016 [7, 8, 9, 10].

Accurate numerical tools are required to predict compressible flows with complex thermodynamics for industrial applications over a range of operating conditions, including close to saturation conditions [1, 2, 3], in the supercritical region [11, 12, 13, 14, 15], or with phase changes [16, 17, 18, 19, 20]. In typical applications, non-ideal gas flows often exhibit high characteristic Reynolds numbers, due to the high working pressures and densities and/or to the moderate to high molecular weight of the working fluids at stake. In such conditions, the flow is generally transitional or, most often, turbulent.

A concerted effort by the scientific community has been made in the last two decades to develop NICFD solvers, see [21, 17, 22, 23, 24, 25] to cite some. Most of the studies have initially focused on the solution of the compressible inviscid flow governing equations or the Reynolds-Averaged Navier–Stokes (RANS) equations. The latter remain by far the most widespread model for the design of NICFD systems, and more particularly of non-ideal-gas turbomachinery [e.g. 26, 27, 28]. Unfortunately, by their nature, RANS models are not suited to capture flow transition, separation,

and for non-equilibrium flow conditions involving strong pressure gradients, rotation and streamline curvature (see e.g. [29]).

Experimental data for non-ideal gas flows having been unavailable for a long time, or limited to global measurements of turbine performance (e.g. [30]), the assessment of the predictive capabilities of NICFD solvers has become possible only recently, thanks to significant progress in NICFD experimental facilities. Various teams have developed test benches. The facilities [31, 32, 33] are blow-down wind tunnels, while [34, 35] are closed-loop, allowing the measurement of long signals, e.g. for the generation of turbulence statistics. In all cases, the characteristic Reynolds numbers are very high (in the range  $10^5 - 10^7$ ) while the test sections are rather small (typically, 50 mm), making the measurement of near-wall flow quantities a formidable challenge, because of the extremely thin boundary layers  $O(10^{-1})$  mm [36], which requires the development of miniaturized sensors [37]. Most of the data produced to date are pressure measurements and visualizations of simplified flow configurations like nozzles [32] and airfoils [38] with attached boundary layers, generally well captured by steady and inviscid flow models [39], provided that a suitable thermodynamic model of the gas is used. A notable exception is represented by recent experiments of high-subsonic separated flows past cylinders achieved in the CLOW wind tunnel of FH Muenster [34]. Pressure measurements allowed the first ever assessment of RANS and URANS for an organic vapor (Novec649). RANS matched well the experimental pressure distribution in the attached flow region, but failed in providing an accurate estimate of the base pressure, a quantity of crucial importance for the estimation of turbomachinery losses [40]. Interestingly, the time-averaged URANS solution was shown to improve predictions of the back pressure, even if discrepancies remained, claiming for higher fidelity simulations. More comprehensive experimental data, including some turbulence statistics, are starting to become available to the scientific community. A recent review of experimental techniques for NICFD can be found in [37]. Despite significant progress, the experiments remain difficult and limited, especially concerning fine details of laminar-to-turbulent transition and turbulent dynamics, and their interplay with non-ideal gas phenomena.

Increasingly stringent efficiency requirements and technological challenges associated with the energy transition demand for even more accurate and detailed NICFD models. For that purpose, numerical models resolving at least part of the turbulent content represent an attractive tool to enlarge fundamental knowledge of transitional and turbulent non-ideal gas flows, to support the development of experimental devices and to guide the design of improved energy conversion systems. Specifically, direct numerical simulations (DNS), which resolve all of the turbulent scales, are essential to shed light on how fine-scale turbulence is affected by non-ideal gas thermodynamics and transport properties, while large eddy simulations (LES) and hybrid RANS/LES models, may provide numerical benchmarks for the validation and assessment of lower fidelity RANS models or used for the design of more advanced components.

In the literature, DNS have been carried out for low-Mach-number turbulent flows of light supercritical fluids like carbon dioxide and nitrogen [41, 12, 13, 42, 43, 44, 45, 15, 46, 47]. In most of the considered cases, compressibility effects are negligible or small, yet low fidelity RANS turbulence models strive in reproducing turbulent production mechanisms, and DNS appears an essential tool to shed light into the interaction of supercritical fluid effects and turbulence, and design better models [48]. Another large body of literature deals with direct numerical simulations of two-phase flows with bubbles or droplets (see [49] for a review), even if studies addressing non-ideal thermodynamic effects in turbulent motion are more recent and mostly focus on cavitating or condensing flows using LES [50, 51].

On the other hand, turbulence in molecularly complex organic heat transfer fluids, characterized by strong non-ideal gas effects and high compressibility, has only recently been studied. Understanding non-ideal effects in compressible turbulent flows is of paramount importance for applications in energy conversion and refrigeration systems, such as Organic Rankine Cycles (ORC) and heat pumps, in industrial processes, and for high-Reynolds wind tunnels. The present review summarizes in particular recent progress in high-fidelity simulations of so-called dense gases, i.e. gases with moderate to high molecular complexity and medium to high molecular weight, often constituted of organic compounds, such as heavy hydrocarbons, fluorocarbons, siloxanes, and several kinds of refrigerants. Such fluids can exhibit, in certain ranges of thermodynamic conditions of practical interest, some peculiar thermodynamic and transport properties, which have a profound impact on their gas dynamic behavior, especially in the transonic and supersonic flow regimes. As we will show, dense gas flow properties can also interact with turbulent dynamics, leading to radically different phenomena compared to, for example, standard light fluids such as air. Despite advances in experimental facilities for dense gas flows, the best available tool for understanding the interplay of dense gas effects and turbulence is represented by high-fidelity simulations, for reasons that will be discussed in more detail below. For this reason, we will first review numerical models and methods for high-fidelity simulations of dense gases, and then

discuss the physical insights gained from such simulations.

The remainder of this article begins with a reminder of the properties and the dynamics of dense gases (Section 2). In Section 3, we discuss the numerical models employed in dense gas flow simulations: the governing equations and thermodynamic models, their numerical discretization, and the turbulence modeling strategies. Section 4, illustrates recent results about the stability and transition to turbulence of dense gas flows. Finally, Section 5 reviews studies of turbulent dense gas flows using high-fidelity simulations, spanning from simple canonical flows to turbomachines, and illustrates progress in the understanding of the physical mechanics achieved thanks to the use of advanced numerical methods.

## 2. Dense gas dynamics

This section reviews briefly the main properties of gas flows in the dense regime. For more details, we refer the reader to the review articles of Cramer [52], and Menikoff and Plohr [53].

Dense gases (DG) are usually defined as single-phase fluids, characterized by sufficiently complex molecules and moderate to high molecular weight, working in pressure and temperature conditions of the same order of magnitude of their thermodynamic critical point (see, e.g., [54] and references cited therein). For such fluids, real gas effects play a crucial role in the dynamic behavior of the fluid [55], in a manner that strongly depends on their molecular complexity and molecular weight, which in turn determines the number of active vibrational degrees of freedom according to the fluid working temperature. Dense gas fluid dynamics is governed by a thermodynamic parameter known as the fundamental derivative of gas dynamics [56], defined as

$$\Gamma := \frac{v^3}{2c^2} \left. \frac{\partial^2 p}{\partial v^2} \right|_s = 1 + \left. \frac{\rho}{c} \frac{\partial c}{\partial \rho} \right|_s, \quad (1)$$

where  $\rho$  is the density,  $v$  the specific volume,  $p$  the pressure,  $s$  the entropy, and  $c = \sqrt{\partial p / \partial \rho|_s}$  the sound speed. The first equality in the preceding definition shows that  $\Gamma$  is related to the curvature of isentropic lines in the  $p$ - $v$  plane; according to the second definition,  $\Gamma$  is a measure of the rate of change of the speed of sound in isentropic transformations. From (1),  $\Gamma < 1$  implies  $\partial c / \partial \rho|_s < 0$ , meaning that the speed of sound increases in isentropic expansions and decreases in isentropic compressions, in contrast to the case of perfect gases, where:

$$\Gamma = \frac{\gamma + 1}{2}, \quad (2)$$

$\gamma = c_p / c_v$  being the ratio of the isobaric specific heat  $c_p$  to the isochoric specific heat  $c_v$ . For thermodynamic stability,  $\gamma$  is always greater than unity, hence  $\Gamma > 1$  for perfect gases. On the contrary, heavy gases characterized by high  $c_v/R$  ratios ( $R$  being the gas constant), exhibit extended ranges of density and pressures in which  $\Gamma$  is less than unity, or even negative, the perfect gas behavior being recovered in the low-density limit. Even in this limit, however, the molecular complexity of the gas plays a role, leading to a specific heat ratio  $\gamma$  very close to 1: for  $\gamma \rightarrow 1$  isentropic transformations of ideal gases, for which the well known isentropic law of Laplace ( $pv^\gamma = \text{const}$ ) is valid, also became isothermal ( $pv = \text{const}$ ).

For expanding flows, an important parameter is the ratio of relative Mach number variations to relative density variations at constant entropy. In quasi-1D flow conditions this writes [57]:

$$J := \left. \frac{\rho}{M} \frac{\partial M}{\partial \rho} \right|_s = 1 - \Gamma - \frac{1}{M^2} \quad (3)$$

For a perfect gas,  $J < 0$  at any point in the flow, and the Mach number,  $M$ , can only increase during an isentropic expansion. On the contrary, for a dense gas with  $\Gamma < 1$  it is possible to identify flow conditions such that the Mach number decreases during an expansion.

Dense gas flows exhibit interesting physical behaviours that are not yet fully understood. The most exotic phenomena are expected for a family of heavy polyatomic compounds named Bethe–Zel’dovich–Thompson (BZT) fluids [58, 59, 56], which are theoretically predicted to exhibit a region of negative  $\Gamma$  values (called the “inversion zone”, see [60]) in the vapor phase close to the liquid/vapor coexistence curve. This is theoretically predicted to result in

non-classical compressibility effects in the transonic and supersonic flow regimes, like rarefaction shock waves, mixed shock/fan waves, and shock splitting (see e.g. [60, 61, 52, 62]), although no reliable experimental evidence has been provided yet [63]. BZT properties can be encountered in heavy fluids characterized by large  $c_v/R$  ratios (e.g. [64]), where  $c_v$  is the constant volume specific heat and  $R$  the gas constant.

From a mathematical point of view, the appearance of non-classical nonlinearities in dense gas flow is related to the change in convexity of the inviscid fluxes [53] occurring in regions where  $\Gamma < 0$ . This is illustrated hereafter for the system of 1D Euler equations:

$$\frac{\partial w}{\partial t} + \frac{\partial f(w)}{\partial x} = 0 \quad (4)$$

In the above,  $w = [\rho, \rho u, \rho E]^T$  denotes the vector of conservative variables (i.e. the mass, momentum and energy per unit volume, respectively given by  $\rho$ ,  $\rho u$  and  $\rho E$ , with  $u$  the velocity and  $E$  the specific total energy), and  $f(w) = [\rho u, \rho u^2 + p, \rho u E]^T$  is the flux function. Let us consider the *nonlinearity factor*,  $\alpha_k$ , associated to the  $k$ -th characteristic field of system (4):

$$\alpha_k(w) := \frac{\partial \lambda_k}{\partial w}(w) \cdot r_k(w),$$

where  $\lambda_k$  is the  $k$ -th eigenvalue and  $r_k$  is the  $k$ -th right eigenvector of the flux Jacobian  $A(w) = \partial f / \partial w$ . The  $k$ -th characteristic field is said to be *genuinely nonlinear* if  $\alpha_k \neq 0$ , and *linearly degenerate* if  $\alpha_k = 0$ . The factor  $\alpha_k$  can be expressed as a function of the fundamental derivative  $\Gamma$  [53]:

$$\alpha_k(w) = \epsilon_k \Gamma(w) c(w) \rho,$$

where  $\epsilon_1 = -1$ ,  $\epsilon_2 = 0$ , and  $\epsilon_3 = 1$ . If  $\Gamma \neq 0$ , only the second characteristic field (corresponding to contact discontinuities) is linearly degenerate, and the hyperbolic system of conservation laws (4) is said to be *convex*. On the contrary, for thermodynamic states such that  $\Gamma \approx 0$ ,  $\alpha_k$  vanishes on all characteristic fields and genuine nonlinearity is then lost. Finally, for  $\Gamma < 0$ , the genuinely nonlinear characteristic fields change their sign. Thompson [56] showed that, for 1D unsteady flows,  $\Gamma$  is related to the rate of change of the propagation speed of a simple right-running wave:

$$\Gamma = \frac{\rho}{c} \left( \frac{\partial(u + c)}{\partial \rho} \right)_s.$$

Thus, if  $\Gamma > 0$  compression waves tend to steepen, and rarefaction waves spread out; if  $\Gamma < 0$  rarefaction waves steepen, whereas compression waves spread out; finally, if  $\Gamma = 0$ , waves have fixed form (all characteristic fields are linearly degenerate). For a left-running wave:

$$\Gamma = -\frac{\rho}{c} \left( \frac{\partial(u - c)}{\partial \rho} \right)_s,$$

leading to similar conclusions.

For 2D steady flows,  $\Gamma$  is related to the slope of the flow Mach lines [56]:

$$d(\mu + \theta) = \frac{\Gamma M^2}{(M^2 - 1)} d\theta,$$

$\mu = \sin^{-1}(1/M)$  being the Mach angle,  $M$  the Mach number, and  $\theta$  is the flow deflection angle. If  $\Gamma > 0$ , the Mach lines steepen during compressions past concave walls and spread out for flows past convex walls. The opposite is true if  $\Gamma < 0$ .

For inviscid flows at supersonic speeds, the dense gas behavior affects the entropy change across shocks. For a weak shock wave, Bethe [58] demonstrated that:

$$\Delta s = -\frac{c^2 \Gamma (\Delta v)^3}{v^3 6T} + O((\Delta v)^4) \quad (5)$$

where  $\Delta$  represents the jump in a given fluid property through the shock, and  $T$  is the absolute temperature. For perfect gases,  $\Gamma > 1$ , and a negative change in the specific volume through the shock, i.e. a compression, is required in order

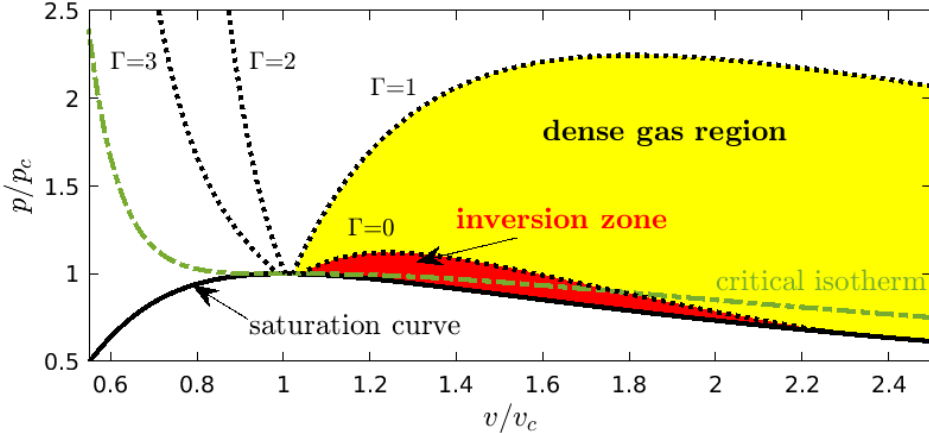


Figure 1: Clapeyron diagram for a BZT Van der Waals gas with  $\gamma = 1.0125$ . The iso- $\Gamma$  (thick dotted lines) are reported as a function of  $v/v_c$ . The dash-dotted line represents the critical isotherm  $T/T_c=1$ . The dense-gas region ( $\Gamma < 1$ ) and the inversion zone ( $\Gamma < 0$ ) correspond to the yellow and red regions, respectively.

to satisfy the second law of thermodynamics. For dense gases with  $\Gamma \ll 1$ , the entropy change is small, leading to reduced shock losses. Note that, if  $\Gamma < 0$  then  $\Delta s > 0$  only if  $\Delta v > 0$ , meaning that expansion shocks are admissible according to the second principle of thermodynamics.

Dense gas phenomena are excluded by the perfect gas (PFG) model, for which isotherms are convex hyperbolae in the  $p$ - $v$  plane, and more complex equations of state (EoS) are used to account for their peculiar thermodynamic behavior. One of the simplest models for dense gases is the Van der Waals (VDW) EoS [65], which takes into account the co-volume occupied by the molecules and the two-body collision interactions. The VDW EoS allows to predict the inflection of the critical isotherm at the critical point ( $p/p_c=1$ ,  $v/v_c=1$ ; subscript  $(\cdot)_c$  indicates the critical conditions) and the change of curvature of the isotherms in the Clapeyron plane  $p$ - $v$  for  $\Gamma = 0$ . As a consequence, VDW is also the simplest possible EoS allowing to account for BZT effects ([58]). Figure 1 displays the Clapeyron  $p$ - $v$  diagram for a Van der Waals gas with  $\gamma = \text{const} = 1.0125$ , representative of a heavy fluorocarbon. The Van der Waals gas model predicts a BZT region (nonclassical or inversion region) and an extended region with  $\Gamma > 1$  (dense gas region).

Considerable progress has been made in the past 30 years about the study of inviscid dense gas flows. Inviscid flows of dense gases have been extensively studied analytically, with focus on the generation of non-classical compressibility effects like expansion shocks, sonic and double-sonic shocks, and shock splitting [66, 60, 67, 64, 61, 53, 52, 68, 69, 62, 70, 71], both for one-dimensional unsteady and two-dimensional steady configurations.

In the case of viscous dense gases, analytical studies have been performed to investigate the dissipative structure of shock waves and the impact of dense gas effects on laminar boundary layers and laminar shock/boundary layer interactions [72, 73, 74, 75, 76, 77, 78]. These studies have shown that it is possible to greatly reduce or even suppress the separation induced by shock/boundary layer interactions for an optimal choice of the operating thermodynamic state. An important consideration is that the molar isobaric heat capacity becomes large as the molecular complexity of the fluid increases. This effect combines with the fact that the heat capacities tend to diverge in the neighborhood of the critical point [73]. Kluwick [75] used the ratio of the specific heat at constant volume over the gas constant,  $c_v/R$ , to characterize the molecular complexity. He found that the Eckert number ( $Ec = U_0^2/2 c_{p0} T_0$ , defined at a suitable reference state with velocity  $U_0$ , temperature  $T_0$  and isobaric specific heat  $c_{p0}$ ), which is the ratio of the kinetic energy over the fluid enthalpy, is proportional to the square of the Mach number  $M$  in the ideal gas limit, whereas it scales with  $M^2 \times R/c_v$  for real gases. Typical molecular complexity values for heavy organic vapors (potentially BZT fluids) range from 100 to 150, so dissipation due to internal friction and heat conduction is negligibly small for dense gases, even at relatively large supersonic Mach numbers. This has dramatic effects on the behavior of shear layers, as discussed later. In addition to smallness of the Eckert number, dense gases also exhibit non conventional variations of the transport coefficients. Specifically, the viscosity  $\mu$  is no longer independent of pressure (or density) [79], and it can decrease with the temperature as in liquids (the behavior of  $\mu$  is in general a transition between the liquid-like

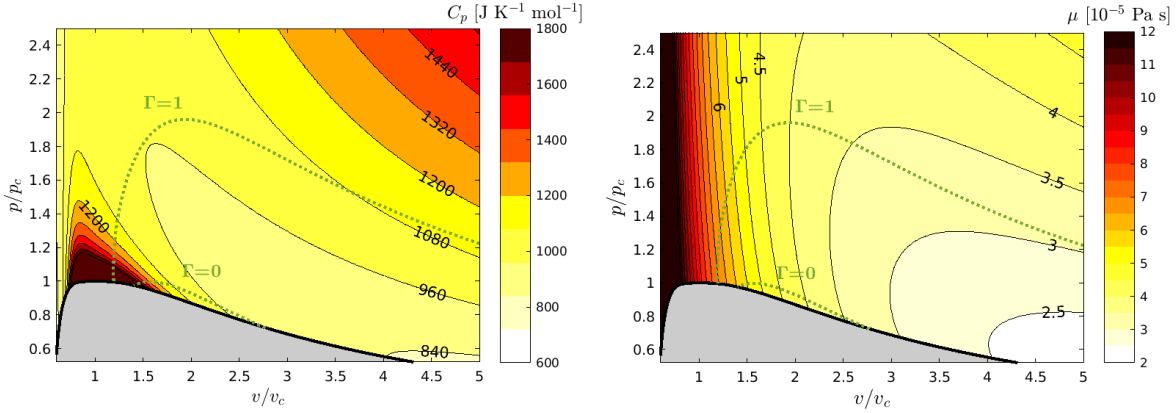


Figure 2: Isocontours of the molar heat capacity  $C_p$  (left) and viscosity  $\mu$  (right) in the Clapeyron diagram for the heavy fluorocarbon PP11 (modeled with Martin-Hou EoS). For air at normal conditions,  $C_p = 3.5 \text{ J K}^{-1} \text{ mol}^{-1}$  and  $\mu = 1.179 \times 10^{-5} \text{ Pa s}$ .

and gas-like regimes). The thermal conductivity  $\kappa$  follows the same trends, and large variations of  $c_p$  induce strong variations of the Prandtl number ( $Pr = \mu c_p / \kappa$ ). Therefore, a dense gas behaves very differently than an ideal gas, where the constant  $Pr$  assumption is generally a reasonable approximation. Figure 2 illustrates the variations of the molar heat capacity  $C_p$  and dynamic viscosity  $\mu$  for the heavy fluorocarbon PP11.

	$\mathcal{M}$ g mol $^{-1}$	$T_c$ K	$\rho_c$ kg m $^{-3}$	$p_c$ MPa	$Z_c$ -	$N$ -	$\gamma_{eq}$ -
R134a (C <sub>2</sub> H <sub>2</sub> F <sub>4</sub> )	102.03	374.2	511.9	4.06	0.262	21.6	1.092
R1233zd(E) (C <sub>3</sub> H <sub>2</sub> ClF <sub>3</sub> )	130.50	439.6	480.2	3.62	0.269	28.8	1.070
R245fa (C <sub>3</sub> H <sub>3</sub> F <sub>5</sub> )	134.05	427.2	516.1	3.65	0.267	32.9	1.061
Toluene (C <sub>7</sub> H <sub>8</sub> )	92.14	591.8	295.2	4.13	0.265	45.2	1.044
Novec649 (C <sub>6</sub> F <sub>12</sub> O)	316.04	441.8	606.8	1.87	0.265	74.2	1.027
MM (C <sub>6</sub> H <sub>18</sub> OSi <sub>2</sub> )	162.38	518.7	268.4	1.93	0.271	77.4	1.026
MDM (C <sub>8</sub> H <sub>24</sub> O <sub>2</sub> Si <sub>3</sub> )	236.53	564.1	256.7	1.42	0.278	115.8	1.017
PP11 (C <sub>14</sub> F <sub>24</sub> )	624.11	650.2	627.1	1.46	0.269	194.6	1.010
D6 (C <sub>12</sub> H <sub>36</sub> O <sub>6</sub> Si <sub>6</sub> )	444.92	645.8	279.1	0.96	0.285	211.8	1.009
FC-70 (C <sub>15</sub> F <sub>33</sub> N)	821.11	608.2	621.4	1.03	0.270	237.4	1.008

Table 1: Thermodynamic properties of some dense gases used in high-fidelity simulations (by increasing molecular complexity): molecular weight ( $\mathcal{M}$ ), critical temperature ( $T_c$ ), critical density ( $\rho_c$ ), critical pressure ( $p_c$ ), critical compressibility factor ( $Z_c = p_c / (\rho_c R T_c)$ ), molecular complexity ( $N$ ) in terms of the number of active degrees of freedom and equivalent ratio of ideal-gas specific heat at constant pressure and volume ( $c_{p,\infty}(T_c)/c_{v,\infty}(T_c)$ ).

In Tab. 1, we report as an example some thermodynamic properties for dense gases used in high-fidelity simulations. The list includes: various refrigerants in the family of hydrofluorocarbons that are used in ORC applications, such as R134a (1,1,1,2-tetrafluoroethane), R1233zd(E) (trans-1-Chloro-3,3,3-trifluoropropene), and R245fa (1,1,1,3,3-pentafluoropropane); the aromatic hydrocarbon Toluene (methylbenzene), the fluoroketone Novec649 (dodecafluoro-2-methylpentan-3-one); the siloxanes MM (hexamethyldisiloxane), MDM (octamethyltrisiloxane) and D6 (dodecamethylcyclohexasiloxane); and the fluorocarbons PP11 (perfluoro-perhydrophenanthrene) and FC-70 (pftripenylamine). Three of such fluids are predicted to exhibit a BZT regions, namely, PP11, D6 and FC-70. Some thermodynamic properties of these gases are given in table 1. In the table we also report the number of active degrees of freedom ( $N$ ) of the gas evaluated at its critical temperature, which is an indication of the molecular complexity of the gas and is defined as [80]:

$$N = 2 \frac{c_{v,\infty}(T_c)}{R} \quad \text{with} \quad c_{v,\infty}(T) = \lim_{v \rightarrow \infty} c_v(v, T) \quad (6)$$

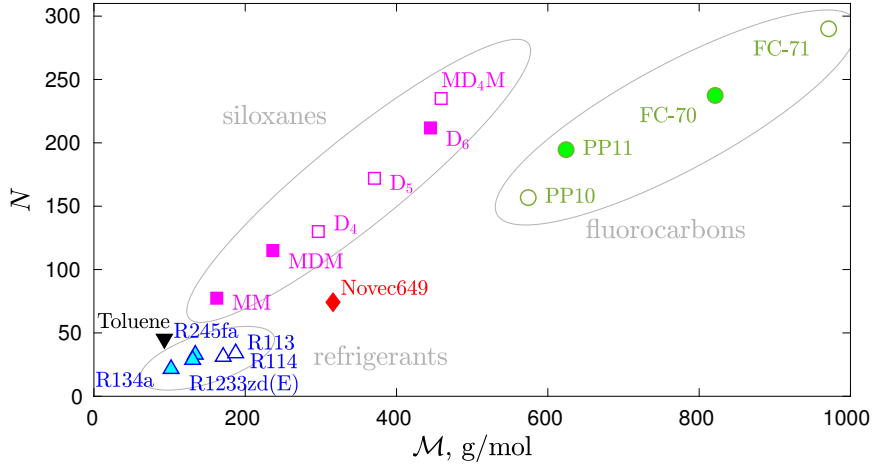


Figure 3: Molecular complexity as a function of molecular weight for some dense gases. Filled symbols correspond to compounds listed in table1. Data for fluorocarbons from [64] and for refrigerants and siloxanes from [55].

and  $\nu = 1/\rho$  the specific volume. It can be seen that the molecular complexity increases moving from top to the bottom of the list. It is related to the equivalent isentropic exponent as  $\gamma_{eq} = 1 + 2/N$ . Note that the heavy compounds  $D_6$  and  $PP11$  have roughly similar values of  $N$  and  $\gamma_{eq}$ , even though  $D_6$  has a lower molecular weight than  $PP11$ . Figure 3 shows the dependency of the molecular complexity  $N$  on the molecular weight for the different families of dense gases. For the heaviest and more complex fluids,  $N$  varies nearly linearly with  $M$ .

### 3. Dense gas flow models

#### 3.1. Governing equations

Dense gas flows are governed by the conservation equations for single-phase, single-species flows. Their differential form for a general curvilinear system of coordinates  $(\xi, \eta, \zeta)$ , mapping the physical space  $(x, y, z)$  reads:

$$\frac{\partial \mathbf{U}}{\partial t} + \frac{1}{J} \left( \frac{\partial \mathbf{F}_c}{\partial \xi} + \frac{\partial \mathbf{G}_c}{\partial \eta} + \frac{\partial \mathbf{H}_c}{\partial \zeta} \right) = 0 \quad (7)$$

with  $J = \partial(x, y, z)/\partial(\xi, \eta, \zeta)$  the Jacobian of the coordinate transformation. The curvilinear fluxes  $\mathbf{F}_c$ ,  $\mathbf{G}_c$ ,  $\mathbf{H}_c$  are the sum of the inviscid (superscript  $e$ ) and visco-thermal fluxes (superscript  $v$ ):

$$\begin{aligned} \mathbf{F}_c^e &= J \begin{pmatrix} \rho \Theta_\xi \\ \rho \mathbf{u} \Theta_\xi + p \nabla \xi \\ (\rho E + p) \Theta_\xi \end{pmatrix}, & \mathbf{G}_c^e &= J \begin{pmatrix} \rho \Theta_\eta \\ \rho \mathbf{u} \Theta_\eta - p \nabla \eta \\ (\rho E + p) \Theta_\eta \end{pmatrix}, & \mathbf{H}_c^e &= J \begin{pmatrix} \rho \Theta_\zeta \\ \rho \mathbf{u} \Theta_\zeta - p \nabla \zeta \\ (\rho E + p) \Theta_\zeta \end{pmatrix}, \\ \mathbf{F}_c^v &= \begin{pmatrix} 0 \\ \boldsymbol{\tau}_\xi \\ \mathbf{u} \cdot \boldsymbol{\tau}_\xi - \mathbf{q} \cdot \nabla \xi \end{pmatrix}, & \mathbf{G}_c^v &= \begin{pmatrix} 0 \\ \boldsymbol{\tau}_\eta \\ \mathbf{u} \cdot \boldsymbol{\tau}_\eta - \mathbf{q} \cdot \nabla \eta \end{pmatrix}, & \mathbf{H}_c^v &= \begin{pmatrix} 0 \\ \boldsymbol{\tau}_\zeta \\ \mathbf{u} \cdot \boldsymbol{\tau}_\zeta - \mathbf{q} \cdot \nabla \zeta \end{pmatrix}, \end{aligned} \quad (8)$$

with  $\mathbf{u} = (u, v, w)^T$  denotes the velocity vector,  $\rho$  the density,  $p$  the pressure and  $E = e + (u^2 + v^2 + w^2)/2$  the total specific energy ( $e$  being the internal specific energy), and with  $\Theta_\xi = \mathbf{u} \cdot \nabla \xi$ ,  $\Theta_\eta = \mathbf{u} \cdot \nabla \eta$ , and  $\Theta_\zeta = \mathbf{u} \cdot \nabla \zeta$  the contravariant velocities. In the preceding equations, we have noted  $\boldsymbol{\tau}_\xi = \mathcal{D} \cdot \nabla \xi$ ,  $\boldsymbol{\tau}_\eta = \mathcal{D} \cdot \nabla \eta$ , and  $\boldsymbol{\tau}_\zeta = \mathcal{D} \cdot \nabla \zeta$ , where  $\mathcal{D}$  is the viscous stress tensor. The tensor  $\mathcal{D}$  follows the Newtonian fluid constitutive relation, with the second viscosity set according to Stokes' hypothesis,  $\lambda = -2\mu/3$ , assuming a zero bulk viscosity. This approximation is well verified for a dense gas (see Appendix B of [81]). The heat flux components are modelled with Fourier's law,  $\mathbf{q} = -\kappa \nabla T$ . The dynamic viscosity  $\mu$  and the thermal conductivity  $\kappa$  are typically functions of the temperature and, for dense gas conditions, also of fluid density (or pressure).

The preceding equations must be supplemented with equations of state and transport-property models for non ideal gases, discussed in Sections 3.2, 3.3. Additionally, for large eddy simulations, the Favre filtered counterpart of Eqs (7),(8) is considered, which contains unclosed terms needing modelling. A discussion of LES models for dense gas flows can be found in Section 4.3.

### 3.2. Equations of state

The governing equations must be supplemented by a model relating the thermodynamic variables  $\rho$ ,  $p$  and  $e$ , i.e., an EoS, of the form:

$$p = p(\rho, e)$$

For perfect gases with constant heat capacities, the latter can be explicitly expressed as:

$$p = (\gamma - 1)\rho e$$

However, for the complex gases at stake, the EoS takes more complex expressions. In this case, it is usual to consider a so-called thermal equation of state, relating the pressure to the density and absolute temperature:

$$p = p(\rho, T) \quad (9)$$

and a caloric equation of state for the energy

$$e = e(\rho, T) \quad (10)$$

The thermal and caloric EoS are related through the compatibility relation:

$$e = e_{ref} + \int_{T_{ref}}^T c_{v,\infty}(T')dT' - \int_{\rho_{ref}}^\rho \left[ T \frac{\partial p}{\partial T} \Big|_\rho - p \right] \frac{d\rho'}{\rho'^2},$$

where the subscript  $(\cdot)_{ref}$  indicates a reference state, the superscript  $(\cdot)'$  denotes integration variables, and  $c_{v,\infty}$  is the isochoric specific heat in the ideal gas limit, for which a suitable expression must be specified. Note that, in numerical simulations, additional thermodynamic relations may be needed to express the boundary conditions or to determine the Jacobians of the flux functions. To efficiently perform numerical simulations of compressible flows with complex thermodynamic behavior, thermodynamic models must be selected that are sufficiently accurate to correctly describe the thermodynamic response of the fluid over a range of conditions of interest, while keeping the overall simulation cost at an acceptable level. This implies that the complexity of implementation in a numerical solver and the resulting computational effort required must be taken into account when selecting the model. The search for a cost/efficiency tradeoff has led to two alternative approaches: the use of analytical thermodynamic functions (either hard-coded in the numerical solver or coupled to external libraries, such as the NIST REFPROP [82]), and look-up tables. The most common models are discussed below.

#### 3.2.1. Analytical equations of state

When large amounts of high-accurate thermodynamic data are available, highly complex multi-parameter reference equations of state can be developed that are capable of describing the thermodynamic behavior of the fluid to within experimental uncertainties of the calibration data. These high accurate equations are usually explicit fundamental equations expressed in terms of a thermodynamic potential, most often the Helmholtz energy, as a function of two other thermodynamic variables (for the present case of simple thermodynamic systems):

$$e = e(\rho, s), \Phi = \Phi(T, p), \Psi = \Psi(\rho, T), \text{ or } h = h(p, s) \quad (11)$$

where  $\Phi$  is the Gibbs free energy,  $\Psi$  is the Helmholtz free energy,  $h$  is the specific enthalpy and  $s$  is the entropy. The advantage of this formulation is that all single-phase thermodynamic properties can be calculated by taking derivatives of the thermodynamic potential. High accurate fundamental equations of state for well-documented fluids such as nitrogen or carbon dioxide, have been developed by fitting very precise experimental measurements for density, phase equilibrium, heat capacity, and speed of sound. Some fluids fitting into this category are listed in [83] and [84]. Reference EoS are generally very complex expressions combining 20 to 60 fluid-specific terms to describe fluid

properties to the order of 0.01% to 0.1%. Unfortunately, such EoS require large amounts of high accurate data, which are generally unavailable or confidential for industrial fluids.

As an alternative to fluid-specific reference EoS, shorter fundamental (i.e. based on thermodynamic potentials) equations using fixed functional forms to determine the fluid properties have been developed for groups of fluids. A fixed functional form means that the number of terms and the temperature and density exponents are the same for all fluids, and only the coefficients are modified. For instance, Span and Wagner [85, 86, 87] developed two short (12-term) fundamental equations with fixed functional forms, one for non-polar or slightly polar substances and one for polar fluids, and fitted them to substances for which highly accurate fundamental equations of state are available. Although the shorter fundamental EoS suffer a slight loss in accuracy, their computational cost is 2 to 10 times less than the more complex forms used in the reference EoS. Lemmon and Span [88] fitted the short equations to 20 fluids of technical use, including several organic fluids often used in energy conversion and refrigeration cycles. The non-polar form of the Span-Wagner equation has also been fitted to two families of linear and cyclic siloxanes by Colonna *et al.* [89, 90, 91]. The 12-term Span-Wagner model takes the following general form:

$$\begin{aligned}\psi(\tau, \delta) &= \psi^0(\tau, \delta) + \psi^{\text{real}}(\tau, \delta) \\ &= \psi^0(\tau, \delta) + n_1 \delta \tau^{0.250} + n_2 \delta \tau^{1.125} + n_3 \delta \tau^{1.500} \\ &\quad + n_4 \delta^2 \tau^{1.375} + n_5 \delta^3 \tau^{0.250} + n_6 \delta^7 \tau^{0.875} \\ &\quad + n_7 \delta^2 \tau^{0.625} e^{-\delta} + n_8 \delta^5 \tau^{1.750} e^{-\delta} + n_9 \delta \tau^{3.625} e^{-\delta^2} \\ &\quad + n_{10} \delta^4 \tau^{3.625} e^{-\delta^2} + n_{11} \delta^3 \tau^{14.5} e^{-\delta^3} + n_{12} \delta^4 \tau^{12.0} e^{-\delta^3}\end{aligned}\quad (12)$$

where  $\psi$  is the reduced Helmholtz energy (i.e. normalized with  $RT$ ),  $\psi^0$  is the ideal-gas contribution to the Helmholtz free energy, and the remaining term  $\psi^{\text{real}}$  represents a real-gas correction, which depends on the reduced density  $\delta = \rho/\rho_c$  and on the inverse of the reduced temperature  $\tau = T_c/T$ . In equation (12), the coefficients  $n_1$  to  $n_{12}$  represent substance-specific coefficients.

To compute the ideal-gas Helmholtz energy, the model is supplemented by additional equations describing the caloric behavior of the fluid. Precisely, the dimensionless Helmholtz energy of the ideal gas is given by:

$$\psi^0 = \frac{h_r^0}{R T_c} - \frac{s_r^0}{R} - 1 + \ln\left(\frac{\delta \tau_r}{\delta_r \tau}\right) - \frac{\tau}{R} \int_{\tau_r}^{\tau} \frac{c_{p,\infty}}{\tau^2} d\tau + \frac{1}{R} \int_{\tau_r}^{\tau} \frac{c_{p,\infty}}{\tau} d\tau \quad (13)$$

where  $c_{p,\infty}$  is the isobaric heat capacity.

A common approximation for the ideal gas contribution to the specific heat at constant pressure is given as a polynomial function of the temperature:

$$c_{p,\infty}(T) = c_{v,\infty}(T) + R = A + BT + CT^2 + DT^3 \quad (14)$$

where the polynomial coefficients  $A$  to  $D$  depend on the substance under consideration. More accurate models based on kinetic gas theory exist, such as the Aly-Lee [92] and the Marsh *et al.* [93] models.

Once the complete relation for the Helmholtz energy has been determined, all other relevant thermodynamic quantities can be derived from its derivatives. For instance, the thermal equation of state is obtained from:

$$\frac{p}{\rho RT} = 1 + \delta \left( \frac{\partial \psi^{\text{real}}}{\partial \delta} \right)_{\tau} \quad (15)$$

and the caloric equation of state is given by:

$$\frac{e}{RT} = \tau \left[ \left( \frac{\partial \psi^0}{\partial \tau} \right)_{\delta} + \left( \frac{\partial \psi^{\text{real}}}{\partial \tau} \right)_{\delta} \right] \quad (16)$$

For less common industrial fluids, data is even scarcer or unreliable. In this case, equations of state based on theoretical and analytical criteria, such as the Van der Waals [65], Redlich-Kwong [94], Peng-Robinson [95], Martin-Hou [96], Benedict-Webb-Rubin [97] equations, and many others (see [98]) are preferred because they require only a

few thermodynamic inputs (e.g. critical temperature, critical pressure, acentric factor) and can be applied to potentially any substance. However, this flexibility is usually obtained at the cost of a loss of accuracy, at least in some ranges of thermodynamic conditions. As an example, we present below two models that have been extensively used in the literature for dense gas flow simulations. The first one is the cubic Peng-Robinson EoS [95], here reported with the modification proposed by Stryjek and Vera [99] (hereafter abbreviated as PRSV). It is given as:

$$p = \frac{RT}{v - b} - \frac{a\alpha(T)}{v^2 + 2bv - b^2} \quad (17)$$

where  $v = 1/\rho$  is the specific volume and  $R$  the gas constant. By enforcing the critical-point conditions, the constants  $a, b$  are given by:

$$a = \underbrace{0.457235}_{a'} \frac{R^2 T_c^2}{p_c} \quad b = \underbrace{0.077796}_{b'} \frac{RT_c}{p_c} \quad \alpha(T) = [1 + K(1 - \sqrt{T_r})]^2 \quad (18)$$

with  $T_r = T/T_c$  the reduced temperature. In the [99] modification, the parameter  $K$  is  $K_0 + K_1(1 + \sqrt{T_r})(0.7 - T_r)$  with  $K_0 = 0.378893 + 1.4897153\bar{\omega} - 0.17131848\bar{\omega}^2 + 0.196554\bar{\omega}^3$ ,  $\bar{\omega}$  being the acentric factor. For  $T_r > 0.7$ , the authors suggest that  $K_1 = 0$ . For cubic EoS, the critical quantities cannot be set independently and, introducing the compressibility factor  $Z_c = p_c/(R\rho_c T_c)$ , the compatibility at critical condition yields

$$1 = \frac{1}{Z_c - b'} - \frac{a'}{Z_c^2 + 2b'Z_c - b'^2} \Rightarrow Z_c \approx 0.3112 \quad (19)$$

For the calculation of caloric properties, the PRSV EoS is supplemented with a model for the ideal gas contribution to the specific heat at constant volume. This can be represented by a polynomial expression, similar to Eq.(14) or, alternatively, by a simple power law of the form:

$$c_{v,\infty}(T) = c_{v,\infty}(T_c) \left( \frac{T}{T_c} \right)^n \quad (20)$$

where the exponent  $n$  is regressed for the fluid and the range of operating conditions at stake.

The second example is given by the thermal equation of state of Martin & Hou (MAH) [96], which has been chosen in several previous works for fluorocarbons [66, 64, 52, 100] in the absence of more validated EoS. This equation is based on a virial expansion of terms and ensures high accuracy with a minimum amount of experimental information:

$$p = \frac{RT}{(v - b)} + \sum_{i=2}^5 \frac{f_i(T)}{(v - b)^i}, \quad (21)$$

with  $b = v_c(1 - \beta/Z_c)$ ,  $\beta = 20.533Z_c - 31.883Z_c^2$ , and

$$f_i(T) = A_i + B_i T + C_i \exp(-kT/T_c), \quad (22)$$

where  $v_c$ ,  $T_c$  and  $Z_c$  are the critical specific volume, temperature and compressibility factor, respectively, and  $k=5.475$ .  $A_i$ ,  $B_i$  and  $C_i$  are gas-dependent coefficients that can be expressed in terms of the critical temperature and pressure, the critical compressibility factor, the Boyle temperature (which may be expressed as a function of the critical temperature) and one point on the vapor pressure curve. Also in this case, the temperature dependence of the low-density specific heat is approximated by a power law or by a polynomial.

In Fig.4 we compare the saturation curves and isotherms calculated using the PRSV and MAH models against the REFPROP data for three typical fluids of moderate (R134a), medium (Novec649) and large (PP11) molecular complexity. As expected, the size of the dense gas region increases with molecular complexity. All three models are in good agreement for dilute gas conditions, while the deviations become more important at supercritical conditions.

While the accuracy of equations of state for real gases is an important aspect, its computational efficiency is also crucial in view of its implementation within a fluid dynamics solver. Computational and memory efficiency are even more critical for high-fidelity simulations, which are already intrinsically computationally intensive for ideal gases. Equations of state expressed in the form of equations (9,10) or through the fundamental relations (11) are

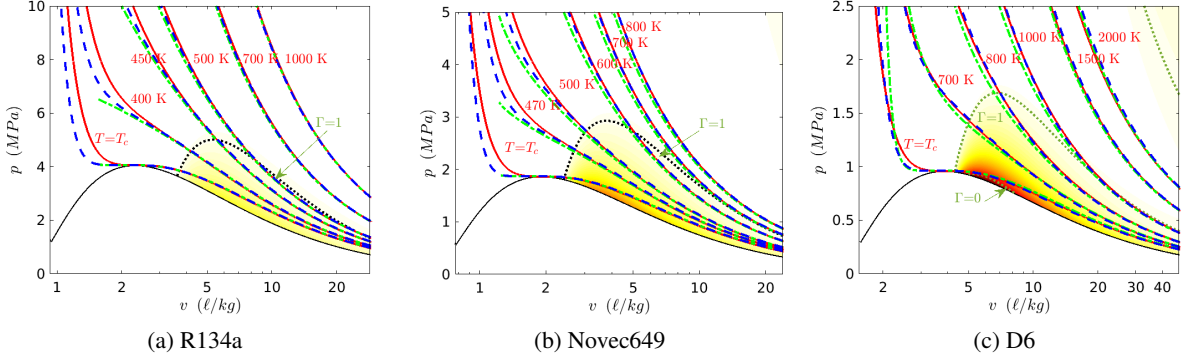


Figure 4: Comparison of isothermal curves obtained with the reference EoS of REFPROP (— · —), PRSV EoS (— · —) and Martin-Hou EoS (— · —) in Clapeyron’s diagram for the dense gases R134a (a), Novec649 (b) and D6 (c). The black line represents the saturation curve and the thick dotted line marks the boundary of the dense-gas region ( $\Gamma=1$ ). The colormap represents decreasing values of the fundamental derivative of gas dynamics  $\Gamma$  (1 to 0, from white to red). A small inversion zone is predicted by PRSV for the heavy siloxane D6.

typically characterized by complex non-linear mathematical expressions. Although these complex expressions are appropriate for the construction of state diagrams, their implementation within a numerical solver for compressible flows is more challenging due to the selection of the independent thermodynamic variables. Typically, the numerical methods are based on formulations of the conservation equations of mass, momentum and total energy as functions of the conservative variables, and the temperature must then be computed numerically from the caloric EoS, which has an impact on computational cost and numerical robustness. Other computational tasks may also require approximate inversion of nonlinear relations, such as the boundary conditions, or the postprocessing of some fluid properties (e.g. the stagnation properties).

### 3.3. Transport-property models

The fluid viscosity and thermal conductivity must be described by models suitable for the dense gas region. Accurate fluid-specific models exist, and several of them are available through the NIST REFPROP library [82]. Such laws can be quite accurate, provided that abundant experimental data are available. This is rarely the case for industrial fluids such as those of interest here, and the few data available are generally limited to the liquid state. In the vapor state, few or no data exist for most dense working fluids. In this case, general equations of state based on first principles are a better choice, since they provide analytical expressions of the transport properties as functions of temperature and density, given a small set of thermophysical parameters. Models widely employed in dense gas flow studies are the generalized laws of Chung *et al.* [79], which accounts for the strong density dependence of the transport properties in the dense gas region. The model includes a density-dependent correction of the Chapman-Enskog formula for pure substances and can be written as:

$$\mu(\rho, T) = \mu_0(T)[1/G_2 + A_6 Y] + \mu_p(\rho, T) \quad (23)$$

where the dilute-gas component  $\mu_0$  is given by

$$\mu_0 = 4.0785 \times 10^{-6} \frac{\sqrt{MT}}{V_c^{2/3} \Omega^*} F_c \quad \text{with} \quad F_c = 1 - 0.2756\bar{\omega} + 0.059035\bar{\xi}_r^4 \quad (24)$$

$\bar{\xi}_r = 131.3\bar{\xi}/(V_c T_c)^{1/3}$  being the reduced dipole moment, and  $V_c$  denotes the molar critical volume in  $\text{cm}^3/\text{mol}$ . The dimensionless Lennard-Jones collision integral  $\Omega^*$  is approximated using the empirical equation of [101]:

$$\begin{aligned} \Omega^*(T^*) = & 1.16145(T^*)^{-0.14874} + 0.52487e^{-0.7732T^*} + 2.16178e^{-2.43787T^*} \\ & - 6.435 \times 10^{-4}(T^*)^{0.14874} \sin[18.0323(T^*)^{-0.7683} - 7.27371] \end{aligned} \quad (25)$$

with  $T^* = 1.2593T/T_c$ . A density dependence is introduced by the nonlinear function  $G_2$ :

$$G_2 = \frac{A_1[1 - \exp(-A_4 Y)]/Y + A_2 G_1 \exp(A_5 Y) + A_3 G_1}{A_1 A_4 + A_2 + A_3}$$

with

$$Y = \frac{\rho}{6\rho_c}, \quad G_1 = \frac{1 - 0.5Y}{(1 - Y)^3} \quad (26)$$

The third term in Eq.(23) is a correction that takes into account dense-gas effects:

$$\mu_p = 36.344 \times 10^{-7} \frac{\sqrt{MT_c}}{V_c^{2/3}} A_7 Y^2 G_2 \exp [A_8 + A_9(T^*)^{-1} + A_{10}(T^*)^{-2}]$$

The constants  $A_1$ - $A_{10}$  are functions of the acentric factor  $\bar{\omega}$  and reduced dipole moment  $\bar{\xi}_r$ :

$$A_i = a_0(i) + a_1(i)\bar{\omega} + a_2(i)\bar{\xi}_r^4, \quad i \in \{1, \dots, 10\}.$$

whose coefficients  $a_0$ ,  $a_1$  and  $a_2$  are given in [79] and in appendix A of [81].

For the thermal conductivity  $\lambda$ , the Chung-Lee-Starling model [79] is used, which is written similarly to the viscosity model (23):

$$\lambda(\rho, T) = \lambda_0(T)[1/H_2 + B_6 Y] + \lambda_p(\rho, T) \quad (27)$$

The dilute-gas contribution  $\lambda_0$  is modeled as

$$\lambda_0 = 418.4 \times 7.452 \frac{\mu_0}{M} \psi$$

where  $\mu_0$  is given by Eq.(24) and  $\psi$  is a modified Eucken-type correlation based on kinetic theory extended to polyatomic gases, where the contribution of internal degrees of freedom (rotational and vibrational) is added to translational degrees of freedom:

$$\psi = 1 + \alpha \frac{0.215 + 0.28288\alpha - 1.061\beta + 0.26665Z_{\text{coll}}}{0.6366 + \beta Z_{\text{coll}} + 1.061\alpha\beta}$$

with a rotational coefficient  $\alpha = c_{v,\infty}/R - 3/2$ , a diffusion term  $\beta$ , empirically linked to the acentric factor as  $\beta = 0.7862 - 0.7109\bar{\omega} + 1.3168\bar{\omega}^2$  and  $Z_{\text{coll}} = 2 + 10.5T_r^2$  modeling the number of collisions required to interchange a quantum of rotational energy with translational energy. In the same way as the viscosity model, the dilute-gas contribution is weighted by a density-dependent nonlinear term  $H_2$ , given by:

$$H_2 = \frac{B_1[1 - \exp(-B_4 Y)]/Y + B_2 G_1 \exp(B_5 Y) + B_3 G_1}{B_1 B_4 + B_2 + B_3}$$

with  $Y$  and  $G_1$  defined by Eq.(26). The third term in Eq.(23) is a dense-gas correction:

$$\lambda_p = 418.4 \times 3.039 \times 10^{-4} \frac{\sqrt{T_c/M}}{V_c^{2/3}} B_7 Y^2 H_2 T_r^{1/2}$$

The constants  $B_1$ - $B_7$  are functions of the acentric factor  $\bar{\omega}$  and reduced dipole moment  $\bar{\xi}_r$ :

$$B_i = b_0(i) + b_1(i)\bar{\omega} + b_2(i)\bar{\xi}_r^4, \quad i \in \{1, \dots, 7\}.$$

with coefficients  $b_0$ ,  $b_1$  and  $b_2$  given in [79].

The transport properties calculated with Chung-Lee-Starling may differ up to 30% with respect to reference models, when these are available. Such differences are mostly due to the density dependence, even in very dilute conditions.

### 3.4. Lookup tables

As an alternative to analytical EoS and transport property models, Look-up tables (LuT) can be adopted to represent the thermo-physical behavior of the fluid: in the thermodynamic region of interest, a grid of nodal points (storing all thermodynamic and transport properties) is preliminary built and the properties at any other point are computed using fast interpolation methods, with a dramatic reduction in computational time. The look-up table method was

proven successful in many applications, such as tabulated chemistry for simulations of hypersonic boundary layers in chemical equilibrium [102], spray combustion [103], or for the design of energy conversion devices [104]. However, standard LuT approaches do not automatically satisfy thermodynamic consistency, as it is guaranteed by the use of analytical EoS, i.e. the direct and inverse computation of a given thermodynamic property from the tables does not necessarily deliver the same result (see [104]). Additionally, LuT may imply considerable memory overloads because of holding in memory the tabular data to be used for interpolation during runtime. Efforts have been made to improve the accuracy and the efficiency of LuT approaches in the context of inviscid and RANS real gas flow simulations. Boncinelli *et al.* [105] generated offline LuT from pre-specified real-gas EoS and proposed an efficient bicubic interpolation method for evaluating thermodynamic properties. The approach can be used in conjunction with any commercial or in-house developed databases, such as refrigerant or steam thermodynamic packages. Pini *et al.* [104] proposed a methodology improving the consistency of LuT. The equations of state are first used to construct a grid of nodes storing a subset of thermodynamic and transport properties required by the method for a given region of interest. Then, an interpolation method is used for determining the remaining properties in any other point. The approach guarantees thermodynamic stability, improving accuracy. Rinaldi *et al.* [106] proposed a LuT method to efficiently compute flux Jacobians and other properties required by numerical solvers without need for evaluating flux derivatives. Finally, Rubino *et al.* [107] proposed a look-up table algorithm based on unstructured grids. The algorithm grants the possibility of a fully automated generation of the tabulated thermodynamic region for any boundary and to use mesh refinement.

### 3.5. Machine learning surrogates

Improving the accuracy of dense gas flow simulations requires using costly advanced thermo-physical models. Direct coupling with thermodynamic libraries implies a significant increase of computational cost (approximately by a factor of ten) with respect to the perfect gas model. Hard-coding of the equations may reduce the cost to a factor 3-5, but the computational burden remains high and any change in the model requires modification of the numerical solver, which is a time-consuming and error-prone process. As mentioned above, using LuT approach may speed-up the calculations considerably, but the CPU cost and memory load becomes considerable for massive high-fidelity computations involving large 3D computational meshes [108, 109]. In this respect, machine learning techniques, naturally suited for representing highly dimensional and strongly nonlinear sets of data, appear as an attractive alternative to LuT for replacing costly thermodynamic libraries.

Early attempts can be found in [110], where an artificial neural network (ANN) surrogate was used to regress the temperature as a function of energy and density. The explicit model  $T = \text{ANN}(\rho, e)$  was then implemented in a dense gas solver in place of the costly iterative calculation of  $T$  from the caloric equation of state at each time step and grid point. The efficiency and accuracy of the procedure was demonstrated in conjunction with the Span-Wagner [86] fundamental equation of state for various non-polar or weakly polar fluids. Replacement of the temperature iterations with the ANN surrogate considerably sped up convergence of the numerical solver reduced computational cost, at the expense of some loss of accuracy when the calculation involved thermodynamic conditions not included in the training set. Recently, Pini *et al.* [109] have proposed an ANN surrogate to a fundamental equation of state based on the entropy, for the light siloxane MM, showing improvement over LuT in terms of convergence rate and memory consumption despite an increased computational cost per point and per iteration, for similar accuracy. Finally, an efficient machine learning surrogate for thermochemical libraries, including dimensionality reduction and online training has been recently proposed by [108] with application to hypersonic flows out of chemical equilibrium. Such an approach can be extended to non-reacting flows of real gases.

## 4. Numerical methods

### 4.1. Discretization schemes

As usual in compressible flow simulations, NICFD solvers can be categorized according to the numerical approach used to discretize the governing equations in space. Finite-volumes (FV) [105, 23, 111, 106, 24], mixed finite volumes/finite elements [22, 112], stabilized finite elements (FE) [113], finite differences (FD) [114, 115, 116, 117, 118], and discontinuous Galerkin finite elements (DG-FE) [119]. NICFD solvers have been developed, both for structured and unstructured meshes. For industrial applications, finite-volume solvers on unstructured or multiblock

structured meshes are the most common choice, in conjunction with upwind discretization of the convective fluxes. This implies the use of approximate Riemann solvers and the calculation of flux Jacobians, which is not straightforward for real gases. For instance, the well-known Roe scheme [120], probably the most used in CFD codes, has no unique extension to flows governed by real-gas EoS, due to the loss of first-order-degree homogeneity of the flux function with respect to the conservative variables for non-ideal gases. A number of extensions of Roe's scheme and other upwind schemes to real gases have been proposed in the literature for chemically reacting flows [121, 122, 123] or for NICFD [21, 124, 106, 125]. The approaches are in most cases direct extensions of methodologies initially tailored to deal with hypersonic reacting flows, for which the use of robust upwind numerical solvers was mandatory. Unfortunately, upwind schemes generally require characteristic decompositions and the computation of flux Jacobians, which complexifies their realization for multidimensional systems and complex thermodynamic models. On the other hand, for non reacting flows of gases close to saturation conditions, governed by complex equations of state, and characterized by "exotic" but quite weak waves, the use of sophisticated characteristic decompositions is not essential. In addition, recent studies have demonstrated the feasibility of central schemes also for highly compressible flows with shocks, provided a suitable shock-capturing technique is employed. For these flows, the use of central schemes appears a convenient choice, due to their conceptional simplicity and low computational cost. Examples of NICFD solvers using central schemes supplemented with artificial viscosity or explicit filtering can be found in [105, 23, 114, 116, 126, 117, 118].

Most NICFD codes where developed to solve the compressible Euler and RANS equations, e.g. for the design of turbomachinery components. To this effect, they rely on at most second-order-accurate spatial discretization schemes and are optimized for steady state computations through the use of implicit time stepping (see e.g. [106]). In some cases, Runge–Kutta (RK) stepping schemes are employed, such as in [105, 23], along with multigrid algorithms and implicit residual smoothing (IRS) to speed up convergence to the steady state.

In recent decades, the quest for high-fidelity simulations of increasingly complex flow configurations has driven the development of high-order numerical solvers. So-called high-order methods (loosely defined as methods whose nominal order of accuracy exceeds second order) have been shown to outperform low-order methods in terms of resolution power, i.e., the number of grid points required to accurately resolve a flow structure of a given size. High-fidelity FD solvers have been developed for the calculation of supercritical flows in simple geometries (e.g. [11, 13, 136]), that could also serve for other NICFD simulations. In the following, we discuss into more detail the high-fidelity solvers that have been employed to simulate dense gas flows. In this context, early use of high-order methods can be found in [23], were a third-order-accurate FV centered scheme was proposed for dense-gas simulations on structured grids. The formulation includes corrections for mesh deformations, and second-order accurate RK time stepping with IRS. Non-linear artificial viscosity (AV) [128] is used to ensure numerical stability and shock capturing. A third-order residual distribution (RD) scheme for steady-state dense gas flow simulations on unstructured grids was proposed in [112]. The steady-state solution is achieved by using a matrix-free implicit formulation and Newton-Krylov iterations. High-order central finite difference schemes were used by Sciacovelli *et al.* [115, 81, 145, 146] for the DNS and well-resolved LES of dense gas turbulence in simple geometries. The inviscid fluxes are discretized by means of tenth-order standard centered or dispersion-relation-preserving (DRP) optimized finite differences using an 11-point stencil. The centered schemes are supplemented with high order non-linear artificial viscosity or non-linear selective filters, resulting in, respectively, ninth- or fourth-order accuracy far from discontinuities. The viscous fluxes are discretized with standard fourth-order centered derivatives, and a four-stage RK algorithm is used for time integration. Giauque *et al.* [113, 147, 148, 149, 150] performed DNS of canonical flows as well as LES of flows through turbine cascade by using the Taylor-Galerkin finite-element solver AVBP [132] with RK time stepping. Touber and Alferez [116, 151] simulated 2D dense gas flows on Cartesian grids by using DRP finite difference schemes optimized on 13 points, supplemented with a selective filter and the localized artificial diffusivity (LAD) method of [136] for shock capturing. Hoarau *et al.* [126] performed LES of dense gas flows through turbine cascades with a high-order finite-volume solver based on the central third-order scheme of [23] and a fourth-order IRS operator (IRS4) initially proposed by [152] in a FD formulation, to enlarge the stability domain of RK schemes for high-Reynolds flows. The IRS approach enabled Courant–Friederichs–Lewy (CFL) numbers as high as 7, resulting in a substantial reduction of the turn-around time of LES calculations. Wang and coworkers [138] carried out DNS of forced dense gas homogeneous and isotropic turbulence using an explicit FD hybrid numerical scheme [153], resulting from the combination of a seventh-order weighted essentially non-oscillatory (WENO) in shocked regions and an eighth-order compact centered scheme is

Ref.	Solver	Equations	Discretization	Str./Unstr.	Multiblock	Spatial scheme	Spatial order	Time scheme	Time order
[22]	ZFLOW	Euler	FV/FE	Unstr.	No	Roe-Vinokur-Montagné [122]	2	Implicit	1
[105]	TRAF [127]	RANS	FV	Str.	Yes	Jameson [128]	2	IRS	1
[23]	DeGas	RANS	FV	Str.	Yes	Centred + AV	3	IRS	2
[111]		RANS	FV	Unstr.	No	HLL [129]	2	Implicit	1
[112]		RANS	FV/FE	Unstr.	No	RD [130]	2 or 3	Implicit	1
[106]		RANS	FV	Str.	No	Various schemes	2	Implicit	1
[114]	MUSICAA	DNS/LES/RANS	FD	Str.	No	Compact [131]+LAD	6	Explicit	3
[81, 117]	AVBP [132]	DNS/LES/RANS	FE	Unstr.	Yes	Centred + AV or filters	9 or 10	IRS4	4
[113]	SU2 [134]	RANS	FV	Unst.	Yes	Taylor-Galerkin [133]	3	Explicit	3 or 4
[24]	CompReal	DNS/LES	FD	Str.	No	Roe-type [122]	2	Implicit	1
[116]	DynHOLab [137]	DNS/LES/RANS	FV	Str.	No	DRP13 [135]+LAD [136]	4 opt.	Explicit	3
[126]		DNS	FD	Str.	Yes	Centred + AV	3	IRS4	3
[138]		DNS	FD	Str.	No	Compact+WENO	8	Explicit	2
[139]	[140]	DNS	FD	Str.	No	Compact upwind [141]	7	Explicit	3
[118]	3DNS [142]	DNS/LES/RANS	FD	Str.	Yes	Compact [143]	4 opt.	Explicit	4
[119]	MIGALE [144]	RANS	DG-FE	Unstr.	No	DG-FE-Vinokur-Montagné [122]	3	Implicit	1

Table 2: Literature review of numerical methods used for dense gas flow simulations.

smooth ones. A hyperviscosity term is added for ensuring numerical stability at small scales. Second-order RK is employed for time integration. Martinez Botas *et al.* [139, 154] used the DNS solver of [140], based on high-order compact upwind schemes [141] for the DNS of channel flows of dense gases. Gloerfelt and coworkers [117] developed a massively-parallel multiblock FD solver for the simulation of turbulent compressible flows, including NICFD [155, 156, 157, 158, 36]. The solver enables DNS, LES and RANS simulations. The inviscid fluxes are discretized by means of tenth-order standard centered differences, along with tenth-order coordinate transforms. The scheme is supplemented with a ninth-order nonlinear artificial viscosity or with tenth-order filtering. Viscous fluxes are discretized with standard fourth-order centered derivatives, and a four-stage RK algorithm along with an improved parallel implementation of the IRS4 approach on curvilinear grids is used for time advancement. Recently, Tosto *et al.* [118] performed DNS of transitional boundary layers of non-ideal gases in dilute or dense conditions using a finite-difference multiblock structured solver based on compact optimized FD schemes and fourth-order RK [143]. Finally, Mantecca *et al.* [119] presented an extension of the MIGALE DG solver of [144] to dense gas flows, with applications to turbomachinery.

The preceding review shows that, while a variety of high-order schemes can be found in dense gas applications, FD methods remain the preferred choice for LES and DNS, with the exception of Giauque *et al.* and Hoarau *et al.*. However, only a few high-order FD solvers have been extended to complex geometries, for which multiblock capabilities or unstructured formulations are mandatory. Table 2 summarizes the level of fidelity and the numerical methods used in some NICFD solvers used in the literature for dense gas flow simulations. Several commercial packages (low-order finite volumes), such as Ansys Fluent and Ansys CFX, also offer NICFD capabilities, but the are beyond the scope of this review.

#### 4.2. Approximations of the boundary conditions

The governing equations must be supplemented with suitable boundary conditions. For permeable (inflow/outflow) boundaries, it is common practice to use characteristic relations or Riemann invariants, which are traditionally expressed using perfect-gas relations and must be extended to gases governed by general EoS. The extension of the Riemann invariants to real gas models is quite involved. To work around this problem, Colonna and Rebay [22] proposed a linearized 1D formulation of the characteristic boundary conditions avoiding complex integrations. Congedo *et al.* [111], developed conditions ensuring an oscillation-free behavior of thermodynamic quantities such as enthalpy and entropy at inlet/outlet boundaries for turbomachinery computations.

On the other hand, accurate unsteady characteristic conditions [159] are generally used for high-fidelity DNS and LES simulations. An extension to general gases has been proposed by [160]. A similar procedure has been used recently by Gloerfelt *et al.* [36] to extend the non-reflecting conditions of Tam & Dong [161] (see Appendix A of [36]).

#### 4.3. Turbulence modelling

Most NICFD solvers mentioned in section 4.1 have been developed for the simulation of dense gas flow in configurations of industrial interest, and more particularly turbomachinery. In most cases, the steady compressible RANS equations are supplemented with linear eddy viscosity models. RANS analysis is supposed to remain appropriate for the preliminary design of non-ideal-gas turbomachinery, under the following conditions :

1. thin, attached and fully turbulent boundary layers;
2. simple geometries, with low aspect ratio, shrouded blades and relatively 2D flow;
3. steady flow.

The most employed turbulence model in NICFD is Menters' two-equation  $k - \omega$  SST [162], widely used in the turbomachinery community. As an alternative, the one-equation Spalart–Allmaras [163] or the algebraic Baldwin–Lomax [164] models have been also used. A few studies [165, 166, 167] have employed unsteady RANS (URANS) simulations, based on the Spalart–Allmaras or  $k - \omega$  SST models.

Only few LES of dense gas flows have been published until now. Use of the classical Smagorinsky [168] or WALE [169] subgrid-scale (SGS) models has been reported in [31, 113] and [150], respectively. For wall-bounded flow simulations, wall-functions are applied at the solid walls to relax mesh resolution requirements. Some studies

have investigated the potential for data-driven development of machine-learned SGS models specifically tailored for dense gas turbulence [170, 150].

On the other hand, the research group to which the authors belong has performed so-called implicit LES, where the highly selective AV or filtering terms have the dual role of ensuring numerical stability and regularizing the unresolved flow scales. This approach has been shown to be effective, provided that a high-order scheme with suitable spectral properties and a sharp cutoff at high wave numbers is used [171, 172].

Finally, due to the very high Reynolds numbers reached in dense gas flows of industrial interest, recent studies have considered the use of hybrid RANS/LES models, and specifically the shear-layer-adapted Delayed Detached Eddy Simulations (DDES-SLA) [173].

## 5. Dense gas stability and transition

### 5.1. Linear stability of dense-gas boundary layers

The linear stability theory (LST) for parallel flows, extended to gases with arbitrary equations of state and transport models, has been used to investigate how dense-gas boundary layers react to modal excitations and to select unstable modes susceptible to trigger transition to turbulence [174, 175, 36]. Other works about non-ideal fluid effects in linear stability analyses include the stability of supercritical fluid flows. Ren *et al.* [176] have investigated the linear stability of insulated flat-plate boundary layers in presence of supercritical carbon dioxide (CO<sub>2</sub>), and showed that the stability is profoundly modified in the transcritical regime (across the pseudo-critical line, also called the Widom line), with the appearance of a new inviscid mode with a growth rate one order of magnitude larger than the Tollmien–Schlichting (TS) mode for high Eckert numbers. Furthermore, Ren *et al.* [177, 176] also showed that the generalized Rayleigh criterion is applicable to non-ideal gases. Some authors have also studied the effects of variations in transport properties. For instance, Govindarajan and Sahu [178] or Saika *et al.* [179] showed that the stability is strongly affected by the stratification of the transport properties, which can be quantified by a single non-dimensional parameter, the Prandtl number.

The base flow for LST is given by the similarity solution of a zero-pressure-gradient compressible laminar boundary layer generalized to fluids governed by an arbitrary equation of state and transport-property models. The first studies dealing with the laminar boundary layer using similarity solutions are [73, 180, 75, 181]. Cramer *et al.* [73] compared similarity solutions for nitrogen N<sub>2</sub>, modeled as a perfect gas, sulfur hexafluoride SF<sub>6</sub>, used in heavy gas wind tunnels, and toluene, widespread in ORC turbomachinery. Kluwick [75] considered laminar boundary layers of nitrogen and two BZT fluids, PP11 and FC-71, whereas Cinnella and Congedo [54] performed numerical simulations for a lighter fluorocarbon (PP10). At supersonic speeds, dissipative effects cause a substantial temperature variation in N<sub>2</sub> or air, and the velocity profile deviates significantly from the incompressible Blasius solution. On the other hand, for all studied dense gases, the temperature remains almost constant due to high heat capacity of the fluid, and the density experiences only weak variations. Consequently, the velocity profiles for dense-gas boundary layers nearly collapse on the incompressible profiles. As an illustration, Fig. 5 compares streamwise velocity and temperature profiles of a zero-pressure-gradient laminar boundary layer for air (flow conditions given in [175]), the heavy fluorocarbon PP11 in BZT conditions [175] and Novec649 in dilute conditions [36]. Similarly to the preceding studies, the high heat capacity of the dense gas leads to weaker variations of wall thermodynamic quantities, with a maximum wall overheat of 2.5% for PP11 and 31% for Novec649 at  $M=6$ , whereas a factor greater than 7 is obtained for air.

In [175], boundary layer stability was first investigated for PP11 at thermodynamic conditions corresponding to a point inside the inversion zone and free-stream Mach numbers  $M$  in the range [0.5, 6]. The results depend on a local Reynolds number  $Re_{L^*} = (\rho_\infty U_\infty L^*)/\mu_\infty$  based on the freestream velocity  $U_\infty$  and the Blasius length  $L^* = (\mu_\infty x/\rho_\infty U_\infty)^{1/2}$ , and on the non-dimensional angular frequency  $\omega L^*/U_\infty$  (or  $F = \omega\mu_\infty/(\rho_\infty U_\infty^2)$ ). Some results are reported in Fig. 6, compared to results for air [175] and for a lighter organic vapor (Novec649) in dilute conditions [36]. Two sets of results are well separated. In the low frequency range, typically  $\omega L^*/U_\infty \lesssim 0.05$ , the first mode occurs, which is the continuation of the viscous Tollmien–Schlichting instability. In the high frequency range, a strong instability arises for  $M \gtrsim 2.5$ . Up to low supersonic Mach numbers, in line with results for perfect-gas boundary layers, the TS mode is damped by compressibility. Due to the high heat capacity of dense gases, the friction heating at the wall is very weak, the boundary-layer thickening (observed for perfect gases) is inhibited and the generalized inflection point, defined by  $\partial(\rho\partial u/\partial y)/\partial y = 0$ , is not present or located very close to the wall. As a consequence,

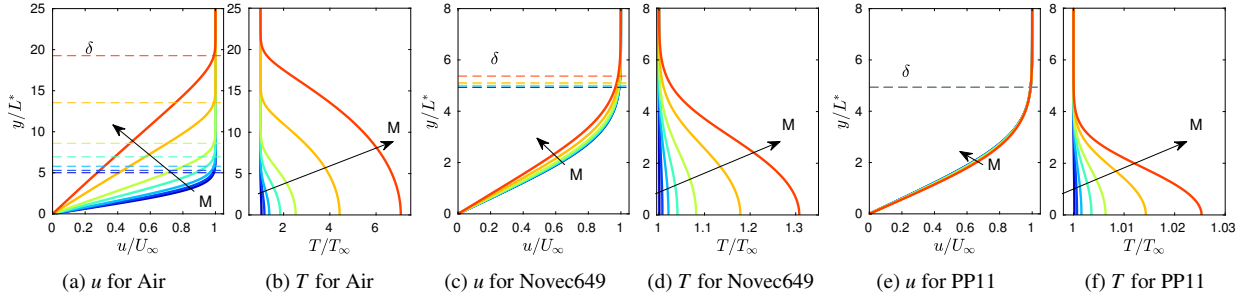


Figure 5: Influence of Mach number on similarity solutions of laminar boundary layers of air (a,b), Novec649 (c,d) and PP11 (e,f). Flow conditions are given in [175] for air and PP11 and in [36] for Novec649. For air and PP11,  $M=0.5$  (—), 1 (—), 1.5 (—), 2.25 (—), 3 (—), 4.5 (—), 6 (—). For Novec649,  $M=0.3$  (—), 0.9 (—), 1.5 (—), 2.2 (—), 3 (—), 4.5 (—), 6 (—). Horizontal thin dashed lines denote the location of the 99% boundary layer thickness  $\delta$ .

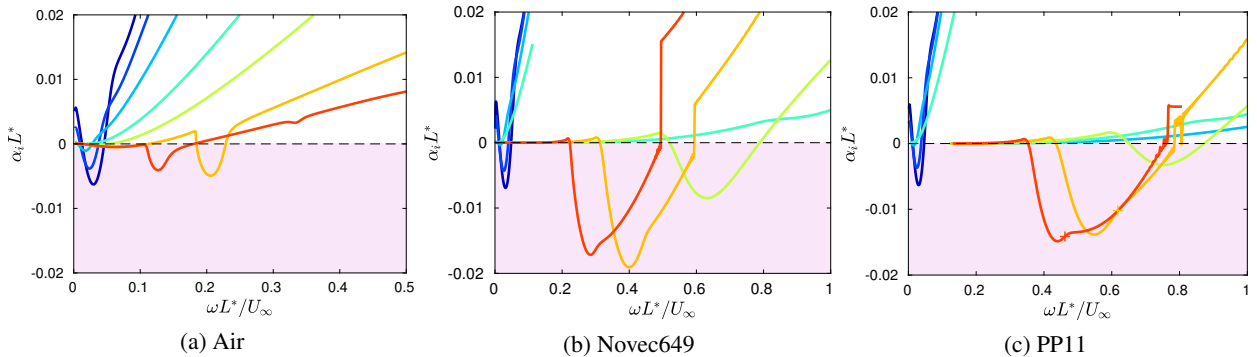


Figure 6: Influence of Mach number on the growth rate of LST modes in a boundary layer at  $Re L^* = 2000$ : (a) air [175]; (b) Novec649 [36]; (c) PP11 [175]. Line legend as in Fig.5. In panel (c), a + sign for  $M=4.5$  and 6 indicates the location where the phase speed becomes supersonic.

the 2D TS mode turns totally stable for dense gases at  $2 < M < 3$ . In contrast, for a perfect gas, the stabilizing effect of compressibility is counterbalanced by the appearance of the generalized inflection point and the oblique TS mode, called the first mode, becomes more and more inviscid. For higher speeds ( $M > 4$ ), a region of the mean flow becomes supersonic relative to the instability phase speed, and multiple modes can exist including Mack's mode, commonly referred to as the second mode [182]. It is sometimes qualified as an "acoustic" mode, due to the presence of acoustic waves trapped between the wall and the relative sonic line. For a dense gas, the acoustic mode appears in a high frequency range and bears similarities with the mode recently observed in high-enthalpy highly-cooled hypersonic air boundary layers [183, 184], which is called a supersonic mode (since its phase speed can reach relative supersonic values). These conclusions seem relatively robust since different dense gases (refrigerants R134a, R245f and siloxanes MDM, D<sub>6</sub> in [175] and Novec649 in [36]), different working conditions and different equations of state lead qualitatively to the same results. Note that in an unpublished work, Chakravarthy [174] studied dense gas effects on LST of laminar boundary layers for toluene vapor at six Eckert numbers (which can be related to the Mach number). The linear stability theory (LST) shows that the boundary layer becomes more stable as the Eckert number increases, developing eventually no modal instabilities for  $Ec > 0.15$ .

To get insights into the peculiar high-frequency supersonic mode that appear in dense gases, the growth rates and phase speeds for Novec649 at  $M=6$  are reported in Fig.7. The fact that the friction heating is dramatically reduced entails a thinner boundary and a thinner height of the acoustic wave guide. As a consequence, the acoustic wavelength is reduced and the acoustic mode is moved towards high frequencies (a similar mechanism exists for cold walls). In this frequency range, the eigenvalue, giving rise to the first mode, called mode S because it comes from the slow acoustic branch [185], is strongly stable. The terminology is more explicit by looking at the phase speed in Fig.7(b). At  $\omega=0$  (leading edge), mode S has a phase speed  $U-c$  (slow acoustic waves). Other modes correspond to eigenvalues with phase speed  $U+c$  at the leading edge (fast modes) and are thus referred to as modes F<sub>1</sub>, F<sub>2</sub>, ... In Fig.7(a), the unstable acoustic mode arises first from mode F<sub>1</sub>. After the maximum amplification, near  $\omega L^* / U_\infty \approx 0.3$ , a kink

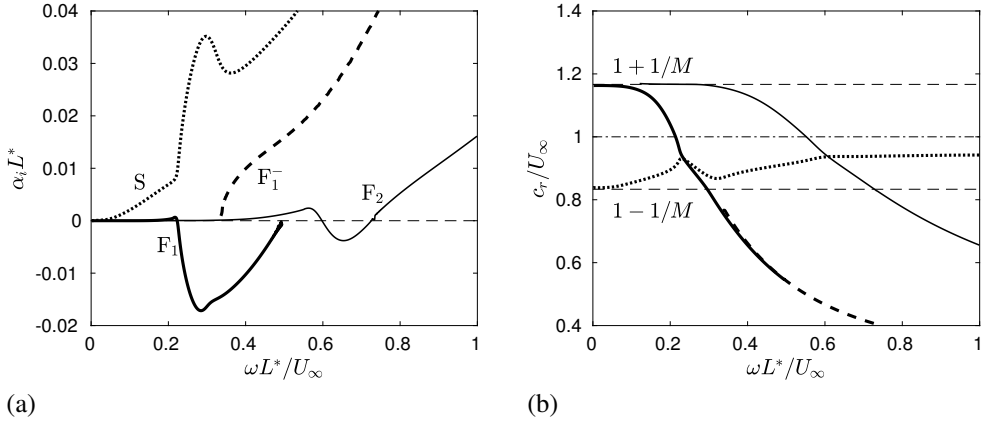


Figure 7: LST for a Novec649 boundary layer at  $M=6$  and  $Re_{L^*}=2000$ : (a) growth rate and (b) phase speed.

is visible that corresponds to the frequency where  $F_1$  phase speed has decreased below  $1 - 1/M$  and thus becomes supersonic (marked by + sign for  $M=4.5$  and 6 in Fig.6c). Such a mode is called a supersonic mode. As it stabilizes, the eigenvalue crosses the slow acoustic branch (located on the real axis) leading to the discontinuities observed in Fig. 6. In fact, after the branch cut, a new eigenvalue (noted  $F_1^-$ ) occurs. This phenomenon is similar to the synchronisation with the entropy/vorticity branch, well described in [185] or [186]. Even if the main mechanism are similar among various dense gases, the peculiar behaviour of each compound, such as the onset  $M$  of the supersonic mode, can be related to their sound speed that modifies the resonance frequency of acoustic waves.

For the high-subsonic to low-supersonic speeds of interest for dense-gas applications, three-dimensional instabilities develop preferentially with an obliqueness angle that reduces their relative phase speed. They have been studied in [175, 36] by varying the wave angle (or equivalently the spanwise wavelength). Another important aspect is the study of transient growth in compressible boundary layers of dense gases. Transient growth due to the non-normality of the eigenmodes is indeed a candidate mechanism for many examples of bypass transition. It has not been investigated for dense gases but results of Ren *et al.* [177, 176] for supercritical CO<sub>2</sub> indicate that transient growth is weakly affected by non-ideal effects.

### 5.2. Natural transition in dense-gas boundary layers

The prediction of the laminar-turbulent transition in non-ideal fluids is of utmost importance to improve the efficiency of many industrial processes. In [36], a natural transition using oblique modes (type 'O') has been simulated by means of DNS and LES for a zero-pressure-gradient flat-plate boundary layer of the organic vapour Novec649. Realistic operating conditions, representative of CLOWT facility, have been selected ( $M=0.9$ ,  $T_\infty=100^\circ\text{C}$  and  $p_\infty=4$  bars). For the transonic to supersonic speeds of interest for turbine applications, the unstable mode in the boundary layer is the TS mode, which has a greater amplification for 3D skewed waves. Consequently, a pair of oblique modes with an angle of 30° is determined with LST and entered at the inlet of the computational domain to trigger laminar-to-turbulent transition. The inlet Reynolds number based on Blasius length  $L^*$  is  $Re_{L^*}=1000$ , the excitation frequency is  $\omega_0 L^*/U_\infty=0.02$  and the spanwise wavenumber  $\beta_0 = 0.04L^*$ . The DNS path is shown in Fig.8(a), where the neutral curve for air is superimposed to show that the TS mode is very similar but slightly more stable in Novec649. Three-dimensional and top views of the transitional region are reported in Fig.8(b,c). A checkerboard pattern is visible in panel (c) just after the inlet due to the interaction of the two initial oblique waves with opposite angles. The  $\lambda_2$ -criterion rapidly shows saturated Λ-shaped vortices due to nonlinear energy transfer between modes. An analysis in terms of frequency-spanwise wavenumber modes ( $\omega/\omega_0$ ,  $\beta/\beta_0$ ) indicate the rapid growth of laminar streaks (modes (0,2)) that takes over the initial mode (1,±1), as sketched in panel (b). Nonlinearities then rapidly develop with the eruption of streak harmonics, as highlighted by the successive doublings of the spanwise period in the top view. The scenario follows what is known in air (generation of streaks by lift-up, streak instabilities and breakdown). The amplitude and frequency of oblique modes inducing the natural transition have been varied in order to determine how long it takes to reach an equilibrium turbulent state. Due to the high density and low viscosity of the organic

vapor, the Reynolds number increases rapidly and, even if the LST analysis is non-dimensionalized, the onset of TS waves corresponds to a higher Reynolds (see panel a). As a consequence, the initial instability growth is postponed, and the transition is delayed accordingly, meaning that equilibrium is obtained for higher values of the Reynolds number. From a practical point of view, the transition occurs few millimeters after the leading edge and the boundary layer thickness is estimated to be less than 0.1 mm, which represents a considerable challenge for experiments.

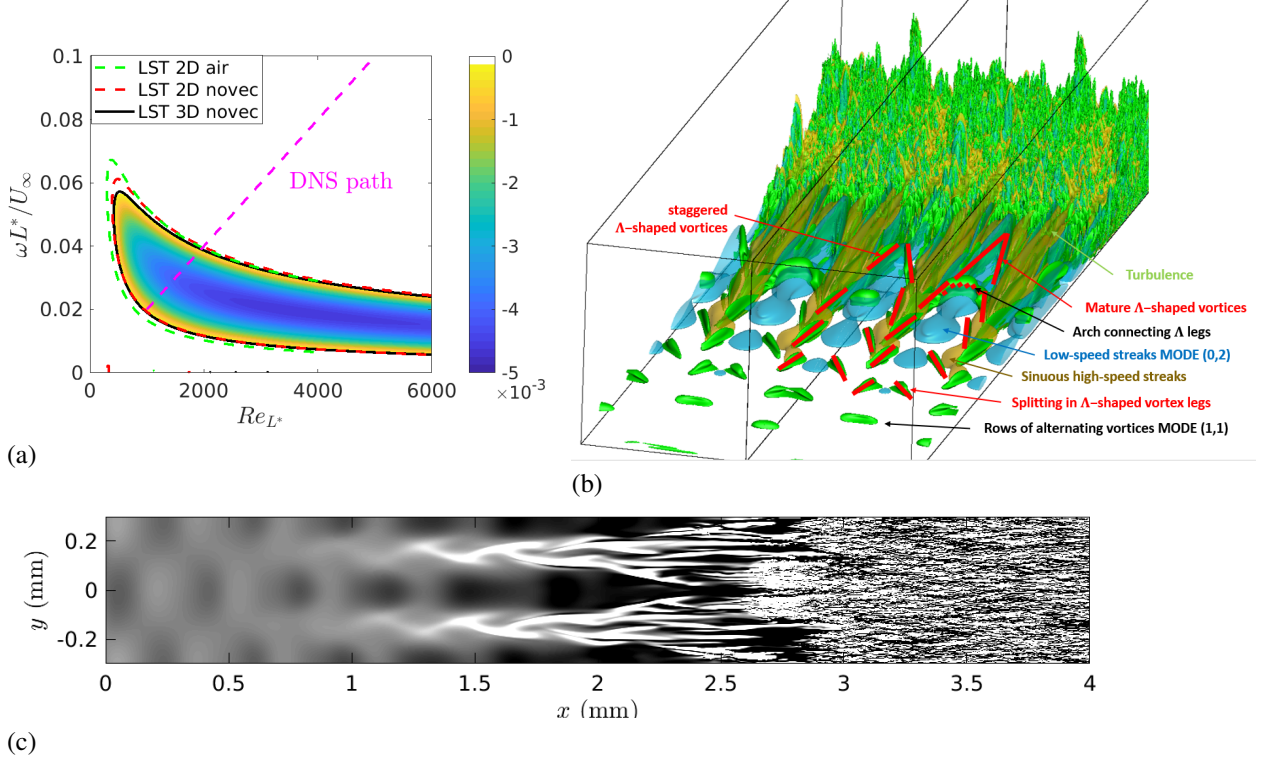


Figure 8: Oblique transition of Novec649 flat-plate boundary layer at  $M=0.9$ . (a) Maps of the amplification rate  $\alpha_i$  from LST and DNS path (magenta dashed line). The black solid line is the neutral curve for 3D oblique waves (with an angle of  $30^\circ$ ); red and green dashed lines are neutral curves for 2D modes with Novec649 and air, respectively. (b) Instantaneous view of the transitional region (duplicated in spanwise direction): low and high-speed streaks are shown by negative (light blue) and positive (light brown) contours of the streamwise velocity fluctuations; an isocontour of the  $\lambda_2$ -criterion (green) is superimposed. (c) Instantaneous top view ( $y^+ \approx 15$ ) of the streamwise velocity fluctuation.

The second (more exotic) example of natural transition used a heavy fluorocarbon PP11 with operating conditions in the inversion zone ( $\Gamma < 0$ ) and a high Mach number,  $M=6$  [187]. Such conditions would be difficult to reproduce in a wind-tunnel (even if PP11 vapour can exist in these conditions), but are chosen to exacerbate dense-gas effects. From the previous LST analysis [175], we know that the laminar-turbulent transition is very particular at this Mach number. The first-mode is indeed totally damped and the only remaining instability is the Mack second mode. But for a dense gas, the acoustic waveguide sustaining this mode is thin and the mode frequency is very high. To figure that point, neutral curves and amplification rates are reported in Fig.9(a) for PP11 and for air (in the conditions of [188]). For air at  $M=6$ , the first mode and the second mode are unstable, their frequency range and growth rate being far smaller than for PP11. In PP11, the second mode takes the form a supersonic mode, which is highly unstable. The supersonic mode has been recently studied in air at very particular conditions, but no full transition to turbulence has been reported. Its very high frequency makes the transition very complex. In the same way as the second-mode transition, the instability is strong but the transition (fundamental or harmonic) generally require additional low frequencies and a complex interaction is responsible for the breakdown. It is exemplified in the 3D and top views of Fig.9(b,c). Initially, high-frequency spanwise rolls correspond to the development of the 2D supersonic mode. In the DNS, the supersonic mode with a frequency  $\omega \delta_{ex}^*/U_\infty = 0.6$  and an amplitude  $\varepsilon = 0.02 U_\infty$  is forced by a suction and blowing wall condition at  $Re_{\delta_{ex}^*} = 1200$ . High-order 3-D waves ( $\beta \delta_{ex}^* = \pm 0.3$ ) are added with a small intensity (5% of

the fundamental) to favor the transition. Due to these small-amplitude high-order modes, low- and high-speed laminar streaks emerge. They appear strongly modulated by the 2D mode (panel b). Streak interactions between  $x/\delta^*=700$  and 800 promote the streak instabilities and breakdown. The generation of streaks results from intermodal exchange with the mean flow, inducing a mean-flow distortion. The supersonic mode is not supported any more, and the transition originates from the meandering laminar streaks, inducing spots that rapidly merge into turbulence, a common feature of most transition scenarios. Finally, even if extreme conditions were used in [187], it is worth noting that an unstable supersonic mode is also present for lighter dense gases and dilute conditions as soon as the Mach number is greater than 3 to 4.

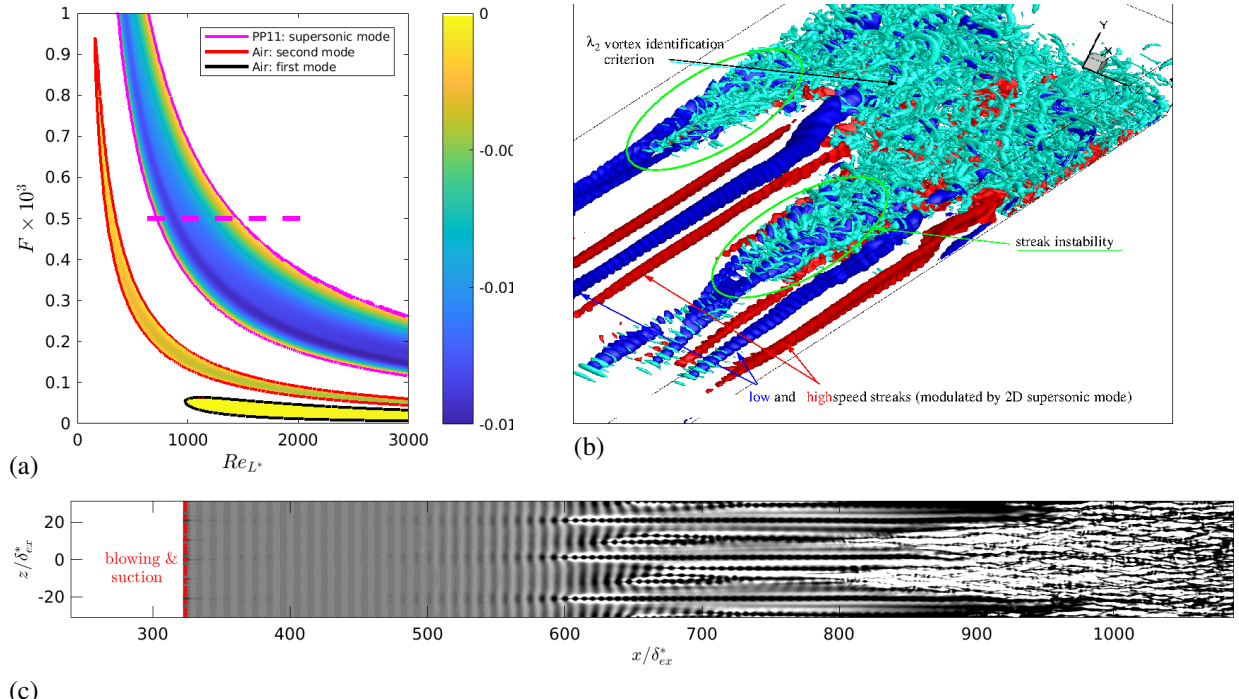


Figure 9: Supersonic-mode transition of PP11 flat-plate boundary layer at  $M=6$ . (a) Maps of the amplification rate  $\alpha_i$  in the  $F$ - $Re$  plane and DNS path (magenta dashed line). The magenta solid line is the neutral curve for PP11 supersonic mode, whereas the black and red lines are respectively the neutral curves for the first and second modes in air. (b) Close-up view of the transitional region: low and high-speed streaks are shown by negative (blue) and positive (red) contours of the streamwise velocity fluctuations; an isocontour of the  $\lambda_2$ -criterion (cyan) is superimposed. (c) Instantaneous top view ( $y^+ \approx 15$ ) of the streamwise velocity fluctuation.

### 5.3. Bypass transition in dense-gas boundary layers

In the previous 'controlled' scenarios, a limited number of waves are excited, whereas in applications, a large number of modes can exist, with possibly non-normal growth or complex receptivity issues. Hence, controlled transitions provide a limited insight but give precious informations on the ability of a particular mode, or set of modes, to yield a complete breakdown to turbulence. In turbomachinery applications, the environment is highly perturbed with high levels of incoming turbulence or the interactions with turbulent wakes from a previous turbine stage. The most likely scenario is termed bypass transition, where the role of primary instability waves is bypassed. In the narrow sense, we mean the superposition on a laminar boundary layer of a freestream turbulence (FST) at an initial turbulence intensity  $T_u$  of  $1\sim 10\%$ . In the general sense, bypass transition refers to transition caused by finite amplitude perturbations.

First insights into FST-induced transition for dense-gas boundary layers were given in [155]. Large-eddy simulations of FST transitions were performed for the organic vapor Novec649. Recent experiments for grid-generated isotropic turbulence in Novec649 [189] indicated that the integral length scale,  $L_f$ , can be very large relative to the boundary layer thickness (due to high Reynolds numbers). The main objective of the study [155] was to investigate the effects of large-scale incoming FST on transition. Integral length scales ten times that generally used (e.g.

in T3A benchmark case) are considered for high and low turbulence intensity. Three cases are described: "low  $L_f$ " ( $Re_{L_f}=1850$  &  $T_u=4\%$ ), "high  $L_f$ -low  $T_u$ " ( $Re_{L_f}=13600$  &  $T_u=2.5\%$ ) and "high  $L_f$ -high  $T_u$ " ( $Re_{L_f}=13250$  &  $T_u=4\%$ ). The flow conditions were selected as representative of CLOWT wind tunnel, namely a freestream Mach number  $M=0.9$ , a temperature  $T=100$  °C and a pressure of 4 bars. A snapshot of the laminar-turbulent transition is reported in Fig.10. The sideview shows the incoming turbulence and the spatial evolution of the boundary layer. Laminar streaks (also called Klebanoff streaks) can be identified on the top view before the transition ( $Re_x \sim 300\,000$ ) and play a crucial role in the transition (see reviews [190, 191]). They have been shown to be optimal structures due to transient growth mechanisms. Secondary instability of laminar streaks are then excited by high-frequency FST and eventually break down, producing a turbulent patch near the wall, called turbulent spots (e.g. at  $Re_x \sim 154\,000$  in Fig.10). A first important outcome of [155] is that a high  $L_f$  tends to delay transition and increases the spanwise scales of the Klebanoff streaks. Overall, the transition process is weakly affected by dense gas effects. The friction coefficient for the various cases are reported in Fig.11(b). Another interesting finding is that for large  $L_f$  and sufficiently high turbulence levels  $T_u$ , the early appearance of  $\Lambda$ -vortices can dominate spot inceptions.

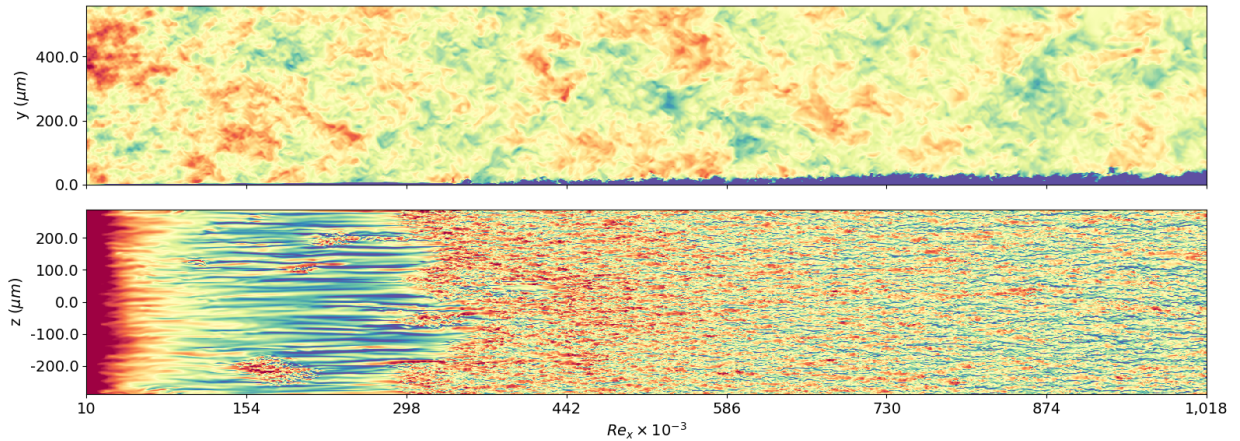


Figure 10: FST-induced transition in flat-plate boundary layers of Novec649. Snapshot of the streamwise velocity for case "high  $L_f$ -high  $T_u$ " (sideview on top and top view on bottom).

The next step in [156] was to include the leading-edge (LE) receptivity effects and the influence of a favorable pressure gradient (FPG). For that purpose, simulations around the nose of an idealized blade, representative of stator blades in turbines, have been carried out with Novec649 at conditions similar to the previously described flat-plate simulations. The flow accelerates from  $M=0.5$  up to 1 on the LES domain (shown in Fig.11a). A relatively high-intensity and large-scale FST, representative of turbomachinery environment, is injected at inlet, with  $T_u=4.3\%$  and  $Re_{L_f}=10450$ . Turbulence is rapidly distorted by the presence of the large LE. Compared to previous studies about LE receptivity on FST transition, the Reynolds number based on the blade half-thickness is one order of magnitude greater due to the high density of Novec649. That means that the elongated structures wrapped around the LE due to stretching and tilting of incoming turbulent structures are very large compared to the boundary-layer thickness (inset of Fig.11a). These streamwise structures appear as clusters of small-scale streamwise vortices, which lead downstream to the formation of Klebanoff-type streaks. However, their distribution is irregular and follows the clusters, as illustrated in the top view of Fig.11(c). As the FPG becomes weaker, transition starts and turbulent spots appear. An important point is that the high-Reynolds-number conditions produces a scale separation, where large-scale wrapped spanwise arrangements modulate the laminar streaks and the spanwise spreading of turbulent spots. The combined effect of FPG and modulation by large scales delays and lengthens the transition compared to flat-plate results [155] (see Fig.11b).

Another interesting observation in [156] is that the turbulent spots bear strong similarities with the ones observed in supersonic flows on cold walls. Spanwise-oriented vortices appear very close to the wall in the turbulent spots (see Fig.12) and persist in the turbulent boundary layer. Their presence is associated with the high thermal capacity of the dense gas, which suppress friction heating and thus temperature rise at the wall, as in the case of an isothermal wall in air. Moreover, the lateral spreading angle  $\alpha$  of the turbulent spots are smaller than in air at high-subsonic speeds ( $M \sim 0.9$ ) and comparable with air flows at Mach  $\sim 3$ . The dense-gas effect thus paradoxically enhances compressibility

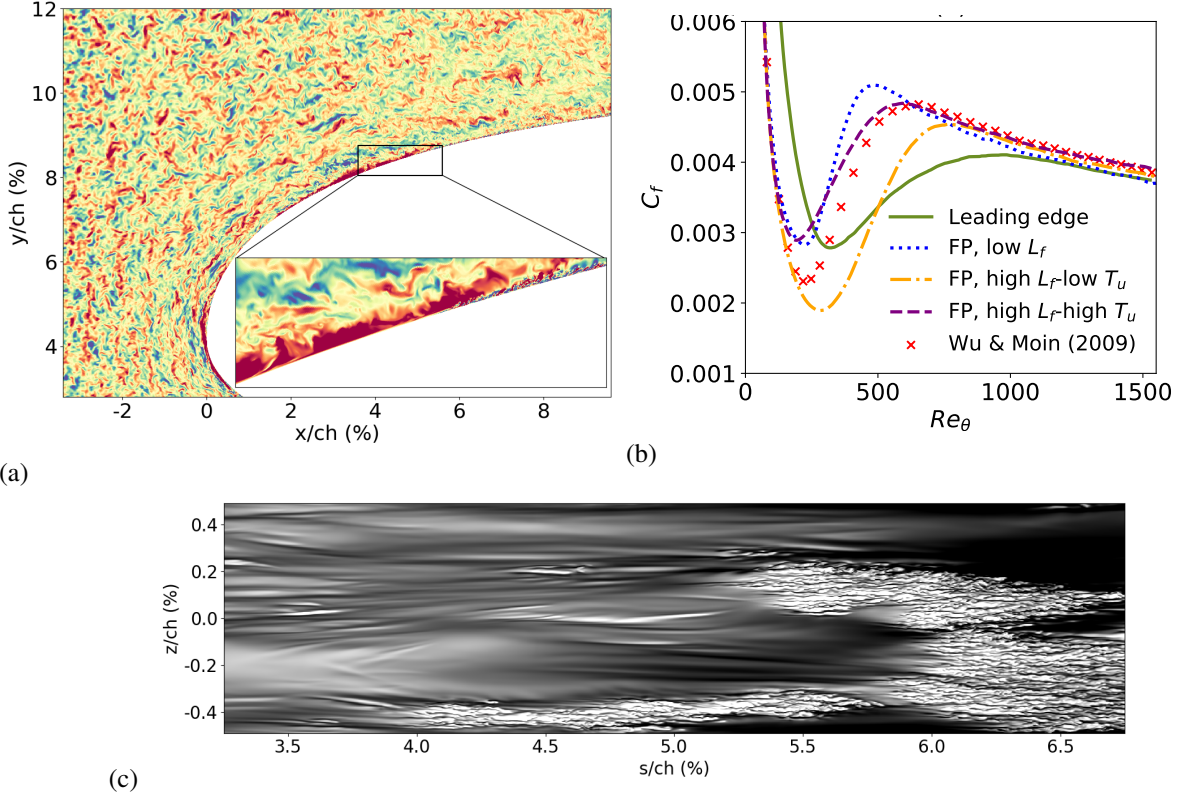


Figure 11: FST-induced transition in the LE-region of an idealized blade with Novec649. (a) Mid-span plane of the spanwise fluctuations  $w'$  with a focus on the BL (levels  $\pm 0.05 \times c_m$ ). (b) Friction coefficient  $C_f$  evolution. The  $C_f$  evolution of the FP LES [155] are also depicted in the panel. (c) Observation of a large structure modulating the laminar streaks and turbulent spot spreading. Tangential velocity fluctuations  $u'_s$  at  $n^+ \sim 15$  (levels  $\pm 0.2c_m$ , from black to white).

and the reduction of  $\alpha$ , which has been observed for cold-wall supersonic air flows [192], may also be a consequence of the Novec649 high thermal capacity.

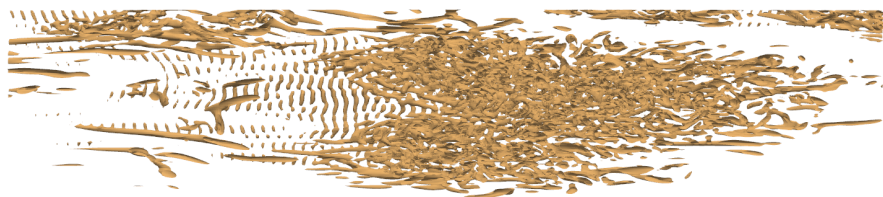


Figure 12: FST-induced transition in the LE-region of an idealized blade with Novec649. Turbulent spots characteristics and observation of near-wall spanwise vortices. ( $Q$ -criterion in light brown).

Yang *et al.* [154] investigated the non-ideal effects on the bypass transition in boundary layers for two dense gases: the refrigerant R1233zd(E) and the siloxane MDM. A blowing and suction at a normalized frequency of  $2.5\pi$  is applied at the wall to simulate a roughness that induces transition. Three operating conditions are tested: (1) in the dilute-gas region, (2) near the saturation line and (3) close to the critical region. They are referred to as cases R1-R3 for R1233zd(E), and cases M1-M3 for MDM. The results are compared with the same setup for air (case AIR). Two additional simulations with air (S1 and S2) are used to investigate changes in the boundary thickness at the blowing and suction location (which virtually correspond to change the plate leading edge location). The position of the bypass transition can be inferred from the  $C_f$  curves in Fig.13(a). It is observed that the onset of transition is earlier

for the dense gases, regardless of the flow conditions. The instantaneous snapshot in Fig.13(b,c) show a single sinuous streamwise streak for air, whereas, two streaks along the span are visible for MDM, which is also characterized by smaller scale structures, meaning that the local Reynolds number is higher. The authors underline that acoustics due to pressure fluctuations can affect turbulent energy transportation.

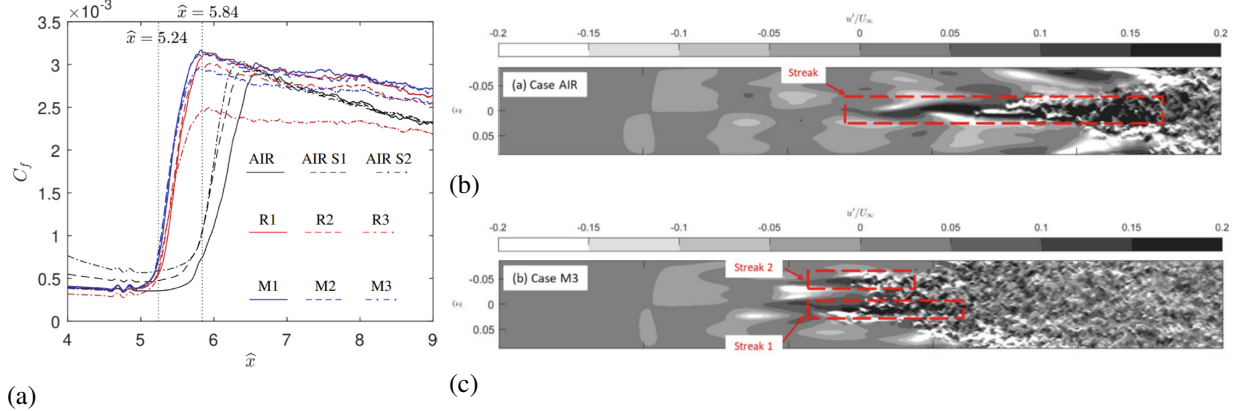


Figure 13: Bypass transition on flat plate (reproduced from [154]): (a) Friction coefficients for the various simulated cases (the blowing and suction device is at the non-dimensional location  $\hat{x}=4.8$ ). On the right, top views of the fluctuating streamwise velocity for (b) case AIR and (c) case M3 (MDM near critical conditions).

## 6. Turbulent dense gas flows

Dense gas flows have been simulated with varying degrees of fidelity for a wide variety of configurations. A number of DNS or well-resolved LES have allowed, for the first time, to shed light on the influence of dense gas effects on compressible turbulence for canonical turbulent flows ranging from free flows, such as homogeneous isotropic turbulence and mixing layers, to wall-bounded flows, i.e. compressible plane channel flows and spatially evolving boundary layers. Dramatic changes with respect to the known behavior for air flows have been pointed out, due not only to dense gas effects, but also to the large heat capacity and complex variations of transport properties. The data have also allowed a priori and a posteriori tests of turbulence models for dense gas flows, compensating for the lack of experimental data for turbulent flow properties. Finally, more recently, LES has been applied to configurations of engineering interest, ranging from simplified turbine vanes to fully 3D turbine configurations, revealing the large errors of RANS models in estimating important performance parameters, such as loss coefficients, and demonstrating the importance of using high-fidelity simulations for radically improved design of engineering systems using NICFD. In the following of this section, we review the main findings for flow configurations of increasing complexity.

### 6.1. Homogeneous and isotropic turbulence

Dense gas effects were first investigated by Sciacovelli *et al.* [115, 145] and by Giauque *et al.* [113] for freely decaying compressible homogeneous isotropic turbulence (CHIT), with focus on the influence of the non-ideal and non-classical thermodynamic behavior on small scales structures, viscous dissipation and enstrophy generation. Compressible turbulence decay is governed by the initial turbulent Mach number  $M_{t_0} = u_{\text{rms}_0}/\bar{c}_0$  and the Reynolds number  $Re_{\lambda_0} = u_{\text{rms}_0}\lambda_0\bar{\rho}_0/\bar{\mu}_0$ , based on the initial Taylor microscale  $\lambda_0$ , where the overlines denote volume averages.

In all the above-mentioned studies initial kinetic energy spectrum of the Passot-Pouquet type [193] is prescribed, i.e.,  $E(k) = Ak^4 \exp[-2(k/k_0)^2]$ , where  $k_0$  is the peak wavenumber and  $A$  is a constant that depends on the initial amount of kinetic energy. Small values of  $k_0$  are selected, so that most of the energy is initially injected at large scales. Initial velocity field is assumed to be purely solenoidal and the r.m.s. of the thermodynamic variables are set to zero. After a short transient during which the thermodynamic fields are established, a phase mostly dominated by vortex stretching is observed, followed by another governed by dissipation effects [194].

DNS of decaying dense-gas CHIT have been performed at various initial turbulence Mach numbers (for instance,  $M_{t_0} = 0.2, 0.5, 0.8$  and  $1$  in [115, 145]), Reynolds numbers ( $Re_{\lambda_0} = 75$  [113],  $200$  [145] and  $\infty$  [115]; in the

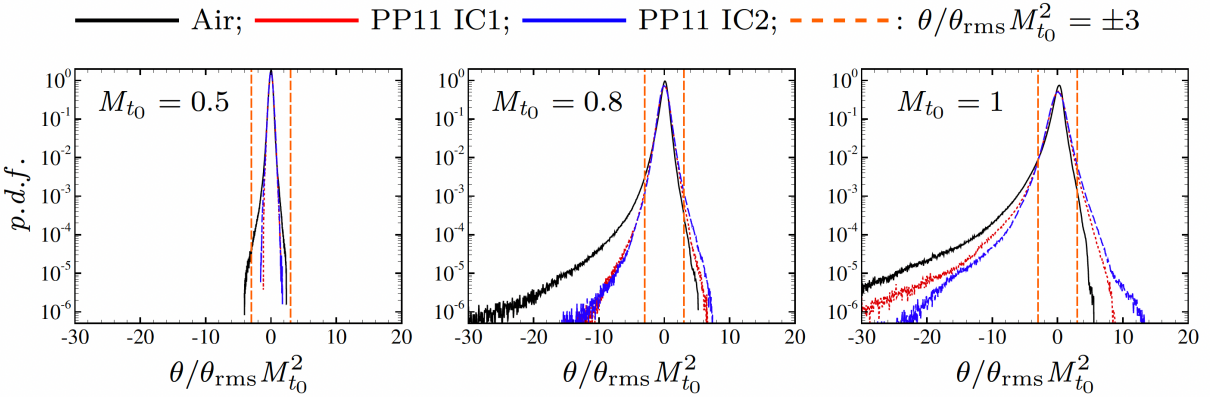


Figure 14: Probability distribution functions (PDF) of the normalized dilatation  $\theta/\theta_{rms}$  at various initial turbulent Mach numbers and at  $Re_{\lambda_0} = 200$ . Black: Air; red: PP11 at dense gas conditions IC1; blue: PP11 at BZT conditions IC2. The orange broken lines indicate the regions corresponding to strong compressions ( $\theta/\theta_{rms} \lesssim -3$ ) and to strong expansions ( $\theta/\theta_{rms} \gtrsim 3$ ). As gas non-ideality increases, the PDF skewness toward negative values is reduced.

latter case, the simulations correspond to implicit LES), and gases (a BZT Van der Waals gas in [115], the heavy fluorocarbons PP11 in [145] and FC-70 in [113] modeled through the MAH EoS). Various initial thermodynamic states were also considered: Ref. [145] considered thermodynamic conditions lying immediately outside the inversion zone ( $\rho_0/\rho_c=1.618$ ,  $p_0/p_c=1.02$ ,  $T_0/T_c=1.01$ ,  $\Gamma_0=0.1252$ , named case IC1) and inside the inversion zone ( $\rho_0/\rho_c=1.618$ ,  $p_0/p_c=0.98$ ,  $T_0/T_c=1.001$ ,  $\Gamma_0=-0.093$ , named case IC2), potentially leading to BZT effects such as the occurrence of non-classical shocklets. Thermodynamic conditions in the BZT region have been also considered in [113]. DNS results for forced CHIT have been also reported by Giauque *et al.* [147] (for FC-70 at  $Re_{\lambda_0}=100$  and  $M_{t0}=0.8$  and BZT thermodynamic conditions) and by Duan *et al.* [138] (for PP11 at  $Re_{\lambda_0} \approx 153$  and  $M_{t0} \approx 1$  and various thermodynamic conditions: dilute, strongly non-ideal, BZT).

Both the gas molecular complexity and non-ideal or non-classical effects were found to play a role in the time evolution of mean thermodynamic properties, most notably for initial turbulent Mach numbers greater than 0.5. In contrast, most kinematic properties (velocity spectra, total kinetic energy and total enstrophy) were weakly sensitive to the gas nature [115, 145], except at very small scales [147].

More specifically, the main findings are summarized hereafter. Compared to air flow at the same initial turbulent Mach and Reynolds numbers, the fluctuations of thermodynamic properties such as temperature and pressure (estimated through their root mean square (*rms*)) are considerably attenuated, including for high turbulent Mach numbers. Such attenuation is due in the first place to the increased molecular complexity and not to thermodynamic non-ideality, and it is observed for molecular complex gases also at dilute conditions. Ref. [115] investigate perfect gases with different molecular complexities (resulting in a variety of specific heat ratios  $\gamma$ ). They showed that  $p_{rms}/\bar{p}$  and  $T_{rms}/\bar{T}$  scale as  $\gamma M_{t0}^2$  and  $(\gamma - 1)M_{t0}^2$ , respectively. As a consequence, temperature fluctuations tend to vanish as  $\gamma \rightarrow 1$ , while pressure fluctuations are greatly reduced even for high values of the initial turbulent Mach number. On the other hand, density fluctuations are little sensitive to the gas complexity, since they simply scale as  $M_{t0}^2$ . When comparing a highly non-ideal and a perfect gas with similar molecular complexity (i.e. dense vs. dilute conditions), it is shown that non-ideal thermodynamic effects tend however to enhance the fluctuations of thermodynamic quantities [115], due to increased compressibility. In addition, for strongly non-ideal thermodynamic conditions such that the fundamental derivative  $\Gamma$  is close to zero or negative, the flow dilatational behavior exhibits dramatic qualitative deviations with respect to perfect gases, due to the non-classical variation of the speed of sound. While in perfect gases strong compression regions occur with much higher probability than strong expansions, due to eddy shocklets, the volume fractions occupied by strong expansion and compression regions are much more balanced in dense gases. Moreover, strong expansion regions are associated with sheet-like structures instead of tubular eddy structures, thus suggesting the possible occurrence of expansion eddy shocklets at BZT conditions. Figure 14 shows the probability distribution functions (PDF) of the dilatation  $\theta$  (divergence of the velocity field) at various Mach numbers for air and PP11. While the PDF for air becomes strongly skewed toward negative values, the PDF for PP11 at BZT conditions IC2 remains

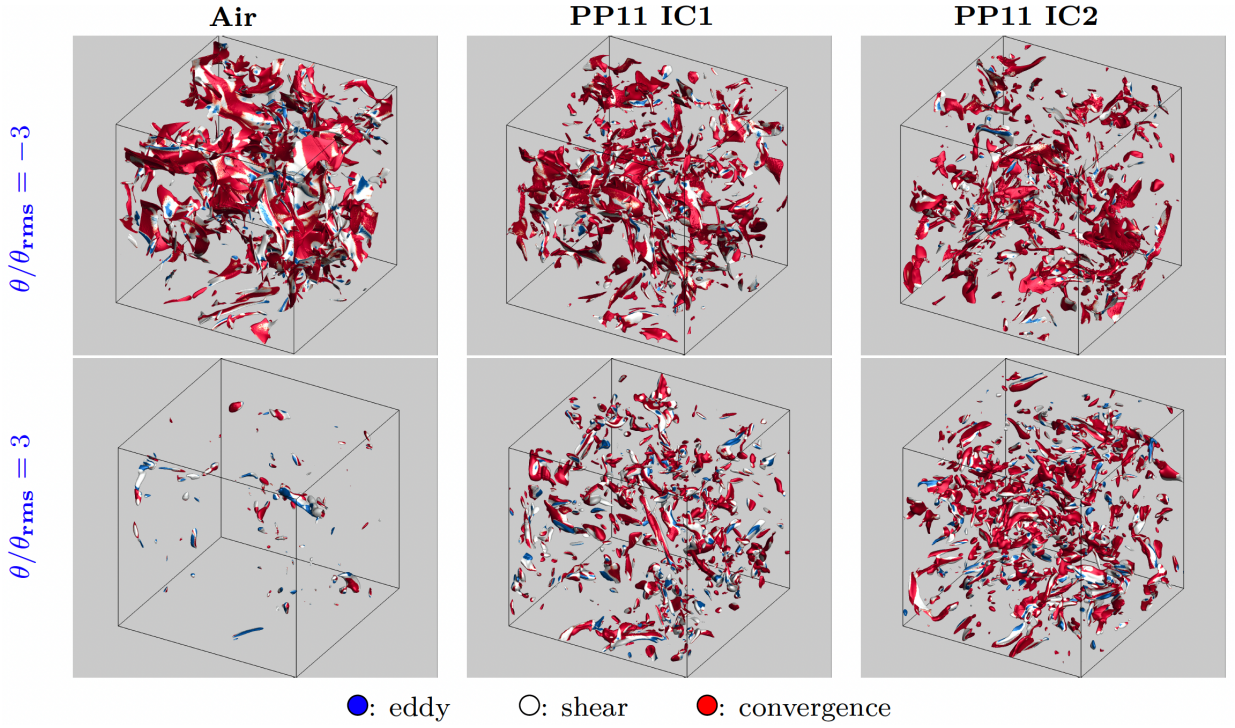


Figure 15: Strong expansions (identified through the isosurface  $\theta/\theta_{rms}M_{t_0}^2 = 3$ ) for air and PP11 at conditions IC1 and IC2 of [145] at  $M_{t_0} = 1$ , colored with the local type of structure. Blue: eddy structures; white: shear structures; red: convergence structures.

rather symmetric up to very high values of  $M_{t_0}$ . An analysis of the statistical properties of turbulent structures in the plane of the second and third invariant of the deviatoric strain-rate tensor [145, 138] shows a weakening of compression regions and an enhancement of expanding ones for dense gas turbulence, independently on the occurrence of BZT effects, provided that the fundamental derivative is close enough to 0. Such regions are classified according to the local level of normalized velocity divergence  $\theta/\theta_{rms}M_{t_0}^2$  [115] and regions with  $|\theta/\theta_{rms}M_{t_0}^2| \gtrsim 3$  are categorized as strong expansions/compressions. Additionally, strong expansion regions are mostly populated by non-focal convergence structures typical of strong compression regions, in contrast with the perfect gas that is dominated by eddy-like structures. Figure 15 shows the iso-surfaces  $\theta/\theta_{rms} = -3$  and  $\theta/\theta_{rms} = 3$  for air and for PP11 at  $M_{t_0} = 1$ . The colormap corresponds to the local type of structure determined from the discriminant of the solenoidal deformation tensor (see [145] and references cited therein for details). The analysis allows to distinguish so-called eddy-dominated zones (vortices), shear zones (e.g. between vortices) and convergence zones (shocklets). While in perfect gases the latter are dominantly associated with strong compression regions, in dense gases they are more balanced among compressions and expansions, due to the attenuation of compression shocklets for  $\Gamma \approx 0$  and eventually to the appearance of expansion shocklets (sheet-like structures). As the gas behavior becomes more non-ideal, the amount of strong compression structures tends to decrease and strong expansions tends to increase. Furthermore, the latter are associated with sheet-like isosurfaces of  $\theta/\theta_{rms}$ , identified as "convergence" structures. The forced CHIT DNS of Duan *et al.* [138] confirmed the findings of [145] concerning the appearance of sheet-like expansion structures. They also analyzed the production of enstrophy at small scales and found that dense gas effects weaken enstrophy production in compression regions and enhance expansion regions. The dynamics of eddy shocklets was investigated into more details by [138] in the case of forced CHIT, which allowed to collect shocklet statistics by means of a shocklet detection algorithm based on the Rankine-Hugoniot conditions. Their results numerically confirmed the possible occurrence of expansion eddy shocklets in HIT at high initial turbulent Mach number and BZT initial thermodynamic conditions. Finally, Duan *et al.* [138] exploited the forced HIT DNS database to perform a priori tests of the validity of SGS modeling assumptions and highlighted a strong sensitivity of the pressure dilatation term in the large-scale kinetic energy transport equation to the gas thermodynamic properties, possibly requiring specific modeling.

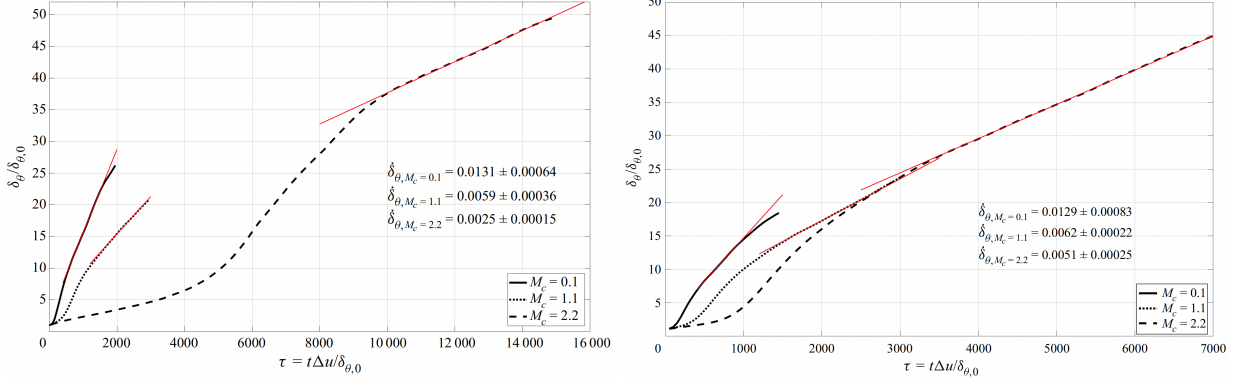


Figure 16: Temporal evolution of the mixing layer momentum thickness for air (left) and FC-70 (right) at  $M_c=0.1, 1.1$  and  $2$ . Reproduced from [149].

The preceding studies have focused on CHIT under very high turbulent Mach numbers and strongly non-ideal conditions. While of theoretical interest, such extreme conditions are hardly realizable in practice. Dense gas flow in practical applications may occur at high Mach numbers, and compressibility effects in turbulence start to appear for turbulent Mach numbers of about 0.5. Hake *et al.* [189] have investigated for the first time decaying HIT of a dense organic vapor both experimentally and numerically. The experiments were conducted in the CLOWT wind tunnel [34]. The working fluid is Novec649, and various runs were performed with Mach numbers ranging from incompressible flow regime up to the inflow choking Mach number of the grids used for generating turbulence. The experimental setup considered mildly non-ideal thermodynamic conditions, with  $\Gamma < 1$  and with a compressibility factor  $Z=0.9$ . Constant-temperature hot wire measurements were conducted using probes with a wire diameter of 5 or  $10\ \mu\text{m}$  and a wire length of 1 and 4 mm. The wire size being much larger than the dissipative scales in the flow, empirical correction schemes based on the assumption of isotropy and spectrum shape should be used. As the Mach number was increased, the experimental turbulence tended to loose isotropy because of disturbances due to grid choking. Comparisons with a companion LES simulation of temporal CHIT based on the MUSICAA dense gas solver were performed at the lowest Mach number, showing a rather good agreement with the experimental measurement of the turbulent intensity decay under Taylor's frozen turbulence hypothesis. Further research efforts and improved miniaturized sensors are needed to provide a more complete experimental exploration of dense gas CHIT, but the reported results represented a very encouraging first step.

## 6.2. Compressible mixing layers

Vadrot *et al.* [148, 149] investigated temporally evolving compressible mixing layers of a dense gas (FC-70) at BZT conditions at various convective Mach numbers  $M_c$ . The Reynolds number based on the initial momentum is taken fixed,  $\text{Re}_{\delta_{0,0}} = 160$ . Figure 16, extracted from [149], shows the spatial evolutions of mixing layer thickness for air and FC-70 at various Mach numbers. One-to-one comparisons between air and FC-70 at  $M_c=1.1$  showed that instability modes evolved differently in the two gases, leading to a sharper thickening in the dense gas. Furthermore, the well-known decrease of the growth rate with the convective Mach number is considerably reduced in the dense gas, and the slopes of the self-similar range of the mixing layer are weakly dependent on  $M_c$ . This effect, also observed for FC-70 at less non-ideal or nearly-dilute thermodynamic conditions, is partly due to reduced Eckert number of dense gases. As a result the growth rate of the FC-70 mixing layers at  $M_c=2.2$  is twice as large as that of air. Yet, the turbulent Mach number in the dense gas is higher than in air and density fluctuations are more intense and more concentrated around the axis. Also, the different small-scale dynamics in the two fluids leads to a reduced dissipation in the dense-gas mixing layer. It is argued that this behavior might require specific treatment in view of the design of improved LES models.

## 6.3. Compressible turbulent channel flows

Dense gas effects in sheared, confined turbulent flows were first investigated in [81], where DNS of compressible turbulent channel flows (TCF) were carried out at three bulk Reynolds numbers  $Re_B = \bar{\rho}_B \bar{u}_B h / \bar{\mu}_w$  (3000, 7000 and

12000) and three bulk Mach numbers  $M_B = \bar{u}_B/\bar{c}_w$  (1.5, 2.25 and 3) [81], where the subscripts  $(\cdot)_B$  and  $(\cdot)_w$  denote time and space averaged values over the channel cross-section and at the wall, respectively. Reynolds averaging is indicated as  $(\cdot)$ , with  $(\cdot)'$  the Reynolds fluctuations; similarly,  $(\tilde{\cdot})$  and  $(\cdot)''$  denote Favre averages and fluctuations. The simulations were performed for air and for PP11, modeled by means of the MAH EoS and the Chung-Lee-Starting transport property laws. The average thermodynamic conditions in the channel were close to the non-classical gas region.

For PP11, due to the very low Eckert number, the average temperature is almost constant across the channel for any choice of the Mach and Reynolds numbers, variations being less than 1%. Decoupling of dynamic and thermal effects in the dense gas also leads to smaller mean density variations across the channel than for an air flow: the wall density is up to 60% higher than the centerline one for air at  $M_B=3$ , whereas variations below 20% observed for PP11. The peculiar variations of transport properties in the dense gas regions are shown to modify deeply the flow dynamics. While viscosity follows the temperature variation for air and increases when moving from the walls to the center of the channel, it varies instead like the density for PP11, tending to decrease toward the channel center. This corresponds to the "gas-like" and "liquid-like" behaviors discussed in [195] for incompressible flows with non-constant properties. Overall, thanks to reduced friction heating in the dense gas, deviations of the velocity profiles with the incompressible law of the wall are found to be much smaller than in air flows at the same conditions. As shown in Fig.17, a good collapse with the incompressible velocity profile could be obtained for all Mach numbers by applying compressibility scalings, such as the van Driest [196] or the Trettel-Larsson [197] scalings. Interestingly, the van Driest scaling, developed for adiabatic walls, does not collapse well velocity profiles for air at various Mach numbers but performs much better for the dense gas, for which the flow is simultaneously isothermal and nearly adiabatic. Due to the reduced centerline viscosity, the local friction Reynolds number  $Re_\tau^* = Re_\tau \sqrt{\rho(y)/\bar{\rho}_w} (\bar{\mu}_w/\bar{\mu}(y))$  (with  $Re_\tau = \bar{\rho}_w u_\tau h / \bar{\mu}_w$ ) increases when moving from the wall toward the channel centerline in PP11. At the wall,  $Re_\tau^*$  is lower than in air at the same conditions, but it is much higher at the centerline, where the values are closer to incompressible channel flow at the same  $Re_B$ . The thermal boundary layer is also affected: the average Prandtl number  $\bar{Pr}$ , is approximately 2 near the centerline, and reaches values as high as 5 at the wall in high Mach number cases, following variations of the heat capacity across the channel. The thermal boundary layer is then about twice thinner than the dynamic one. Variations of the average semi-local Reynolds number in air and PP11 and of the average Prandtl number in PP11 at various Mach numbers are illustrated in Fig.18 as functions of the semi-local wall coordinate,  $y^* = \bar{\rho}(y) u_\tau^* y / \bar{\mu}(y)$ , with  $u_\tau^* = \sqrt{\bar{\tau}_w / \bar{\rho}(y)}$  the semi-local friction velocity.

Despite the liquid-like behavior, the turbulent Mach number reached for given bulk conditions is comparable to air flows (actually, slightly higher). In all cases, the maximum turbulent Mach number is well below the limit where strong compressibility effects, like eddy shocklets, can be expected. Other interesting effects are observed on second-order moments of fluctuating flow quantities. Figure 19 displays selected profiles of the second-order statistics, namely, the  $rms$  of the density and temperature fluctuations and the streamwise Reynolds stress in wall units,  $\overline{\rho u_i'' u_j''}^+ = \overline{\rho u_i'' u_j''} / \tau_w$ . The relative density (and pressure) fluctuations are of the same order as those observed for air flows, whereas temperature fluctuations are nearly two orders of magnitude lower. Remarkably,  $\rho_{rms}$  decreases monotonically from wall to centerline, contrary to light gases that exhibit a peak at a normalized wall distance corresponding to the buffer region of the turbulent boundary layer. In [81], it was shown analytically and numerically that this effect is a consequence of the real gas effects, the density fluctuations being linked to pressure and temperature fluctuations through a real-gas EoS. More precisely, density fluctuations are strongly correlated with pressure ones. This has a consequence on near wall structures: density fluctuations are correlated with pressure ones, unlike the perfect gas, where the near-wall streaks correspond directly to high- and low-density fluid. In all cases, density fluctuations remain small compared to the mean value, and Morkovin's hypothesis is satisfied even at the highest Mach number. Despite the striking differences in the thermodynamic behavior, Reynolds stress profiles are qualitatively similar to those observed for low-Mach channel flows with temperature-dependent transport properties. The liquid-like behavior of viscosity leads to increased spanwise, wall-normal and Reynolds shear stresses with respect to the corresponding incompressible evolution, whereas the streamwise stresses decrease. Finally, energy budgets (not reported) match well the typical distribution for incompressible flow using semi-local scaling. The production peak is located as usual at  $y^* \approx 12$ . For the higher Reynolds number, a second production peak is observed in the outer region, like in high- $Re$  incompressible flow, due to the reduced dissipation close to centerline. The increase centerline Reynolds number also leads to relatively finer flow structures in PP11 than in air: comparison of flow structures for air and PP11  $M_B=3$ ,  $Re_B=12000$

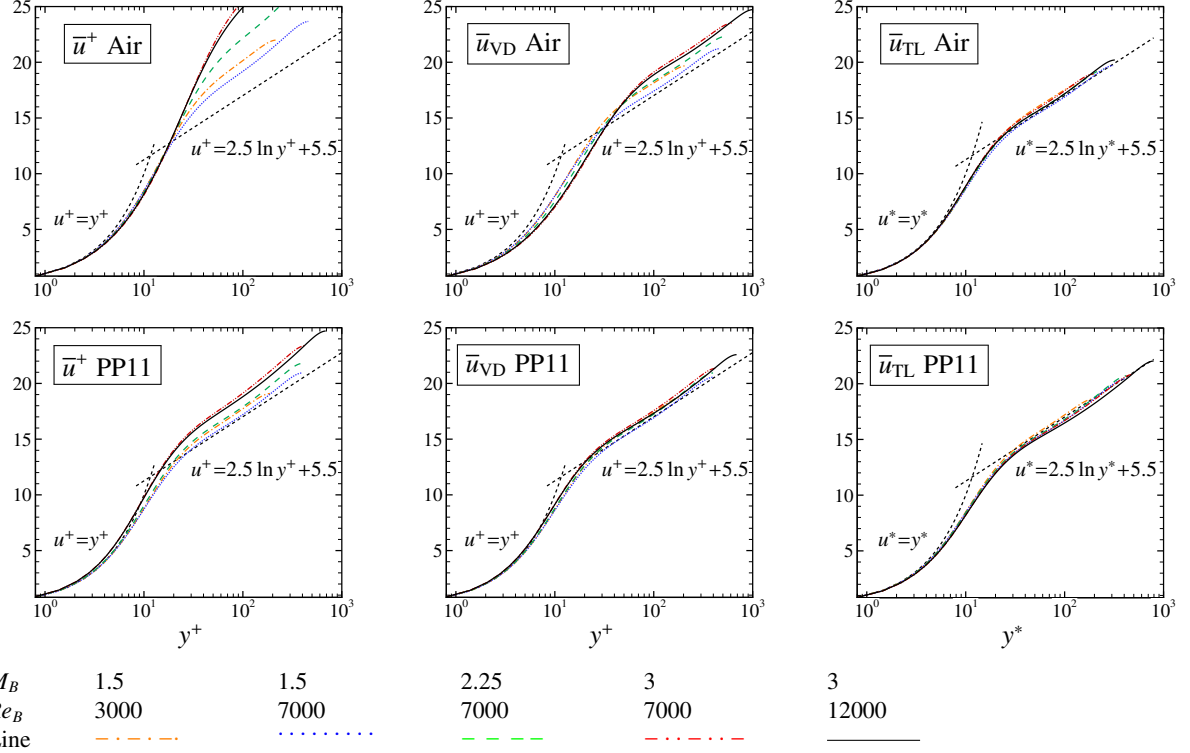


Figure 17: Scaled velocity profiles for channel flows of air and PP11 at various  $M_B$  and  $Re_B$ : standard wall scaling (left), van Driest scaling (center), Trettel–Larsson scaling (right).

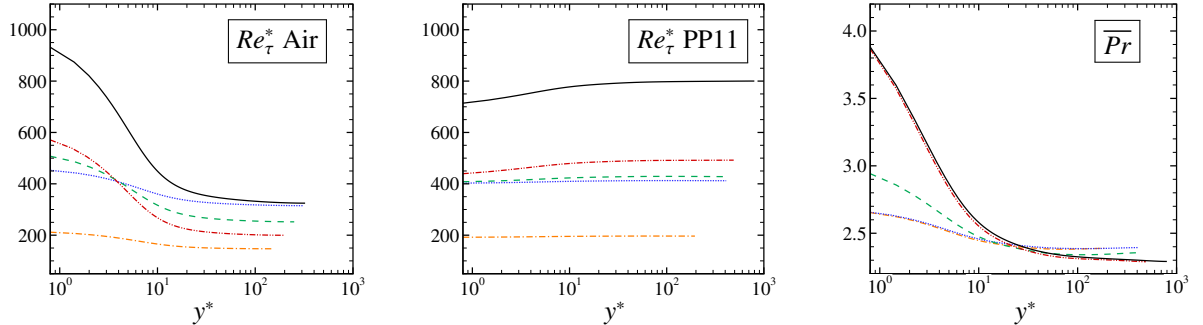


Figure 18: Local friction Reynolds number ( $Re_\tau^*$ ) for air (left) and PP11 (center), and average Prandtl number ( $\overline{Pr}$ ) for PP11 versus  $y^*$  at various  $M_B$  and  $Re_B$ . Line styles as in Fig.17.

is provided in Fig.20. However, when scaled with the semi-local turbulent scale, the non-dimensional characteristic sizes of boundary layer structures are similar for all cases and match the values observed in incompressible flow.

More recently Martinez Botas and coworkers [139] performed DNS of compressible TCF using gases employed as working fluids in organic Rankine cycles, namely, the ozone-friendly refrigerant R1233zd(E) and the light siloxane MDM, modeled by using reference EoS available in NIST REFPROP for these fluids. The considered bulk Reynolds and Mach numbers are in the ranges 2683–4881 and 1.26–2.52. Most of the effects described for thermodynamic quantities in PP11 were also observed for these lighter fluids at operating conditions representative of ORC turbines, and in particular the attenuation of thermodynamic property variations across the channel. The two fluids exhibited liquid-like variations of the viscosity for supercritical working conditions, while almost constant or weakly increasing viscosity values were observed for the other conditions. In all dense-gas cases, the viscosity is at most 15% higher than the wall value at the center of the channel, because of the suppression or significant weakening of friction heating.

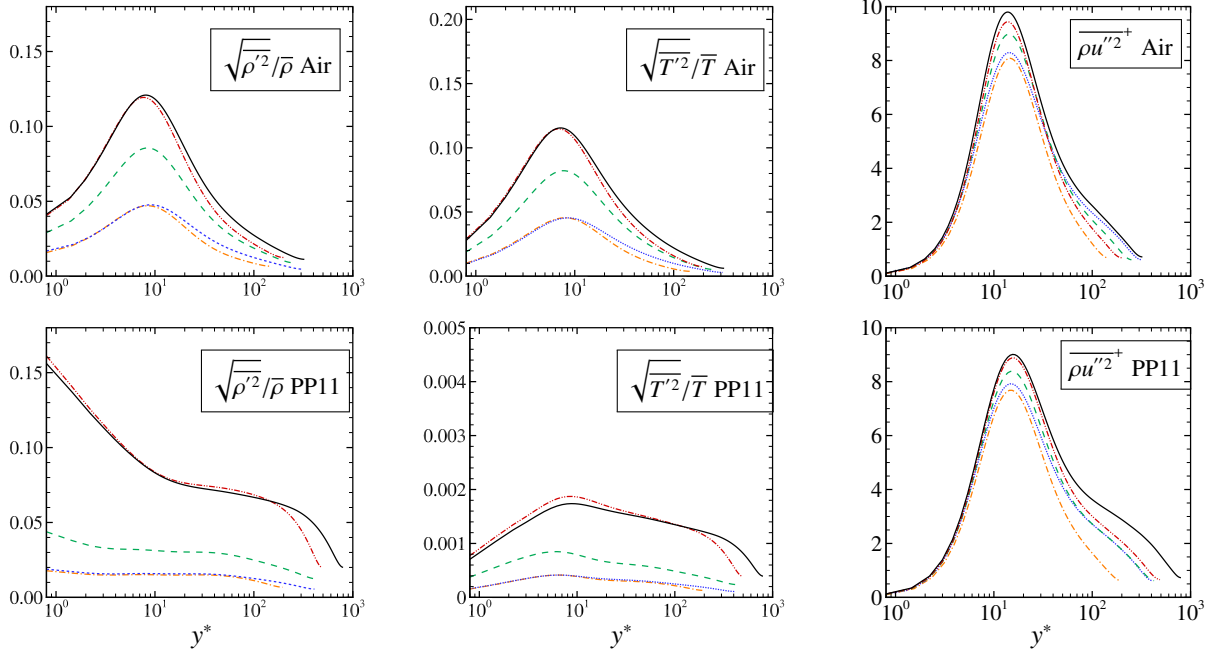


Figure 19: Left to right: Normalized density, temperature and streamwise velocity fluctuations for channel flows of air (top line) and PP11 (bottom) at various  $M_B$  and  $Re_B$ . Line styles as in Fig.17.

The peak values of streamwise and wall-normal Reynolds intensities were respectively lower and higher than in air, indicating that this behavior results from gas non-ideality as well as from liquid-like variations of the fluid transport properties. Similarly, the appearance of an external peak of the production-to-dissipation ratio, absent in air, is also confirmed.

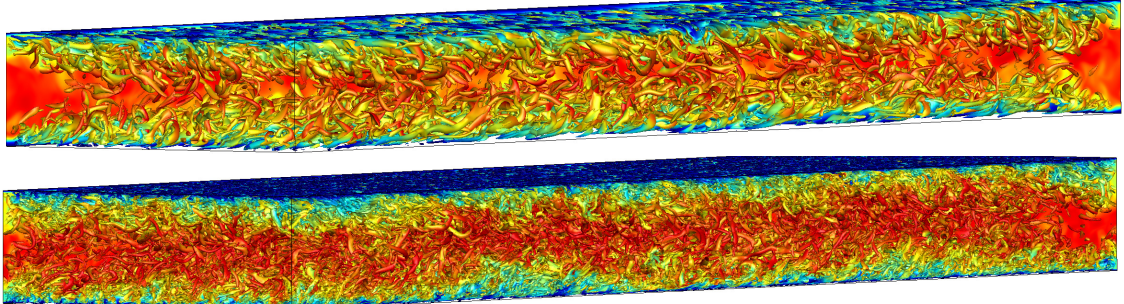


Figure 20: Iso-surface of  $Q(h/u_B)^2 = 1$  colored with streamwise velocity ( $M_B=3, Re_B=7000$ ). Top: air; bottom: PP11.

The DNS data for turbulent channel flows were used to conduct a priori tests of the validity of some common modeling assumptions for the eddy viscosity and turbulent Prandtl number. The study [198] assessed several low-Reynolds formulations of the classical  $k-\epsilon$  model, showing that turbulence models for eddy viscosity follow the exact trend from DNS more closely for dense gas conditions (at least for high Mach number cases), due to the higher local Reynolds number of the dense gas flow. However, the eddy viscosity values are overestimated. It was argued that an adjustment of the model constant could improve the results. A peculiar behavior is observed for the turbulent Prandtl number close to the wall, which peaks more or less abruptly in the viscous sublayer. The reader is referred to [198] for more details. Chen *et al.* [139] also performed a priori tests, and found that the eddy viscosity hypothesis  $\nu_t = k^2/\epsilon$  (with  $\nu_t$  the eddy viscosity,  $k$  the turbulent kinetic energy and  $\epsilon$  the turbulence dissipation) is reasonably well respected in the inertial region of the boundary layers with values of the eddy viscosity constant  $C_\mu \approx 0.009 \pm 10\%$ , as shown

in Fig. 21.

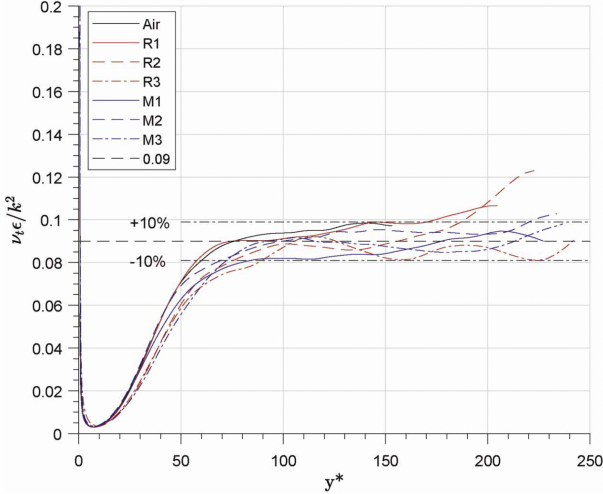


Figure 21: Verification of the eddy viscosity hypothesis  $\nu_t = k^2/\epsilon$  for the cases of [139].

#### 6.4. Turbulent boundary layers

Although the body of literature about turbulent boundary layers (TBL) is vast, few studies have investigated boundary layers of dense gases or organic vapors. The first high-fidelity simulations for a spatially developing boundary layer of a dense gas, namely PP11 at  $M=2.25$  and 6, were carried out in [146]. The evolution of  $C_f$  in Fig.22(a) over the computational domain shows an overshoot during turbulent breakdown for simulations in air, whereas no overshoot is observed for PP11. This is a first indication that thermal exchanges are dramatically reduced, even for very high speeds. In contrast, the  $C_f$  overshoot in air corresponds to an important heat transfer overshoot [188]. The simulations were used to investigate dense-gas effects in the fully-developed turbulent portion of the boundary layer. As expected, the high heat capacity leads to nearly negligible temperature variations across the boundary layer even at hypersonic conditions, and the thickening rate of the boundary layer in the dense gas is close to that of an incompressible flow. Wall-normal profiles of mean thermodynamic and transport properties change with the Mach number, but their variations across the boundary layer are much smaller than in air flow. Accordingly, variations of the fluid viscosity across the boundary layer are greatly reduced, and they follow an opposite trend than in a perfect gas (liquid-like behaviour). The above-mentioned effects lead to higher local Reynolds numbers, and to the appearance of an outer peak in the velocity spectra, similar to high-Reynolds incompressible boundary layers. The velocity profiles and turbulent intensities are almost insensitive to the Mach number (Fig.22b). The most significant deviations from standard behavior are observed for the density (and viscosity) fluctuations, which reach a maximum near the wall in PP11 instead of vanishing as in air. Such behavior, already observed for turbulent channel flows, is shown in Fig.22(c) for density. The reduced thickening of dense-gas TBL leads to a more extended supersonic region than in perfect gases and to higher turbulent and fluctuating Mach numbers. As previously observed for homogeneous isotropic turbulence, expansion and compression events are rather balanced. Snapshots of numerical Schlieren contours for PP11 and air are reported in Fig.23. Density variations are considerably attenuated in the outer region of the dense-gas boundary layer, while a strong dilatational activity is located in the near-wall region.

DNS and LES of Novec649 boundary layers, undergoing modal transition (section 5.2) and FST-induced transition (section 5.3), have been performed up to the fully turbulent state. In particular, the turbulent state at  $M=0.9$  up to  $Re_\theta \approx 5000$  has been scrutinized in [36]. Almost no overshoot of the friction coefficient is observed in Fig.24(a) during turbulent breakdown, as in the FST-induced bypass transition of [199], even if the Reynolds number of transition is larger since the inlet Reynolds number is relatively high. As inferred by the comparison with the DNS of [200] for air at  $M=0.85$ , the  $C_f$  value in the turbulent state is lower in a perfect gas due to friction heating effects. For Novec649, the mean wall temperature differs by less than 1%, so that compressibility effects on the mean flow are almost absent. The mean and fluctuating velocity profiles are thus very close to the incompressible DNS of [201] (Fig.24b). The

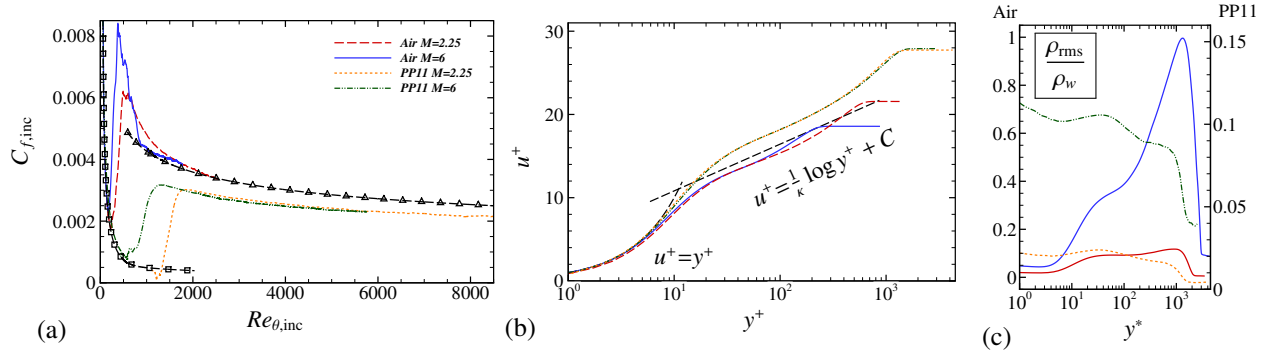


Figure 22: Turbulent boundary layer of PP11 at  $M=2.25$  and 6 [146]: (a) Skin friction coefficient  $C_f$ ; (b) mean streamwise velocity profile in the classical wall scaling and (c) profiles of the scaled density fluctuations versus the semi-local wall coordinate. In panel (a), Blasius laminar solution ( $\square$ ) and turbulent correlation  $C_{f,inc}=0.024Re_{\theta,inc}^{-1/4}$  ( $\triangle$ ).

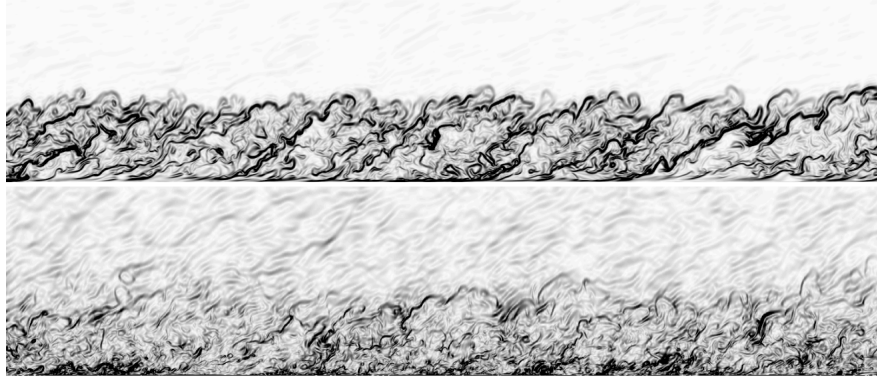


Figure 23: Snapshots of normalized numerical Schlieren for Air (top) and PP11 (bottom) at  $M=6$ .

dynamical properties, such as the scales of turbulent structures, are also very similar to simulations or measurements in air at low speeds. The analysis of thermo-physical quantities however shows genuine compressibility effects. The temperature fluctuations (Fig.24a) are very small and the pressure fluctuations (Fig.24b) follow the incompressible behaviour but the density (Fig.24c) has a peculiar distribution, being highly correlated to pressure, unlike air flows. This affects the profiles of dynamic viscosity, which depends on both temperature and density. Another outcome is that the mean temperature profile can be related to the velocity profile using Crocco-Busemann's approximation but, contrary to air, the recovery factor is lower in the turbulent region than in the laminar one (due to the higher Prandtl number). The turbulent Mach number can reach higher values than in air and intense acoustic waves are radiated, showing that the thermal mode is drastically damped but not the acoustic mode. By comparing TBL obtained with various forcing amplitude and frequency [36] or TBL resulting from FST transition [155], small discrepancies have been noted for the turbulent  $C_f$  values or shape factors. They are interpreted as memory effects. The history of transition can persist in integral quantities due to the relatively high Reynolds number where TS waves start to become unstable. This high-Reynolds-number effect follows directly from the high density of Novec649, and an approximate equilibrium state is obtained for  $Re_\theta \gtrsim 3000$  (compared to a value of approximately 2000 for perfect gas).

Recent years have seen renewed interest for estimating turbine losses, in particular the dissipation due to turbulent boundary layers of dense gases. Similarity solutions for the laminar state and RANS models for the turbulent state were used in [202] to estimate the dissipation phenomena in the boundary layer. Various RANS models to simulate steady turbulent boundary layers are discussed in [203] for a siloxane fluid (MM) at  $M$  between 0.2 and 2.8. Pini and De Servi [204] investigated the entropy generation in laminar boundary layers of dense gases and proposed a reduced-order model (ROM) based on the boundary layer equations. Tosto *et al.* [118] used high-fidelity simulations with the 3DNS code to assess the ROM model. They carried out DNS of spatially developing boundary layers at

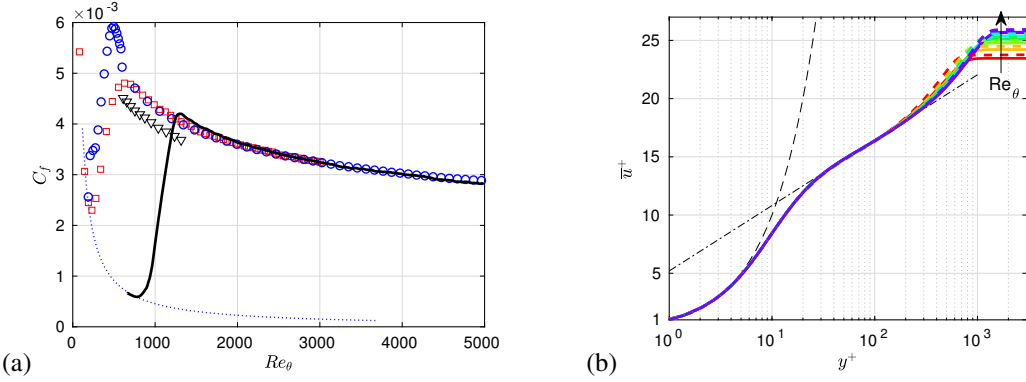


Figure 24: Turbulent boundary layer of Novec649 at  $M=0.9$ . (a) Skin friction coefficient: DNS of [36] (—); incompressible DNS of [201] (○); DNS of bypass transition of [199] (□); compressible DNS of [200] at  $M=0.85$  (▽); laminar Blasius correlation  $0.664/\sqrt{Re_x}$  (····). (b) Mean streamwise velocity at  $Re_\theta=2000, 2540, 3030, 3270, 3630, 3970, 4060$  (solid lines from red to blue) compared to DNS results of [201] (dashed lines) at the same  $Re_\theta$ .

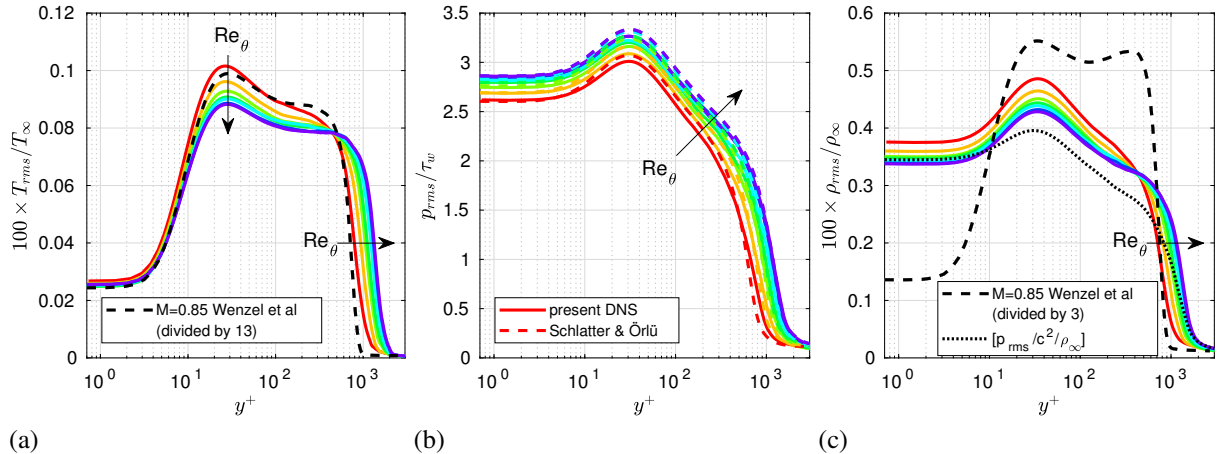


Figure 25: Turbulent boundary layer of Novec649 at  $M=0.9$  [36]. Profiles of fluctuating thermodynamic quantities: (a) temperature, (b) pressure and (c) density at  $Re_\theta=2000, 2540, 3030, 3270, 3630, 3970, 4060$  (solid lines from red to blue). Pressure fluctuations are compared to incompressible DNS of [201] at the same Reynolds numbers (dashed lines); rescaled temperature and density profiles at  $Re_\tau=671$  from DNS of [200] in air at  $M=0.85$  (— · · ·).

$M=0.9$  for air and MM, in dilute- (case *iMM*) and dense-vapor conditions (case *niMM*), where the turbulent state is triggered using a numerical trip. The shape factor  $H$  is 1.45 for *iMM* and 1.49 for *niMM*, close to the nominal value for an incompressible TBL, whereas  $H=1.84$  for air due to the alteration of boundary layer thicknesses by friction heating. The friction coefficient  $C_f$ , reported in Fig.26(a), is higher for siloxane than for air, in line with results for Novec649 in Fig.24(a). The dissipation coefficient in Fig.26(b), defined as

$$C_d = \frac{1}{\rho_\infty U_\infty} \left[ - \underbrace{\int_0^\delta \overline{\rho u_i u_j} \frac{\partial \bar{u}_i}{\partial x_j} dy}_{\text{turbulence production}} + \underbrace{\int_0^\delta \mu \left( \frac{\partial \bar{u}_i}{\partial x_j} \right)^2 dy}_{\text{time-mean strain}} \right],$$

follows qualitatively the same trend as  $C_f$  due to the decoupling between thermal and kinematic fields. The ROM [204], coupled with an algebraic turbulence model, give a fair estimation of the dissipation rate. Another conclusion is that dense gases are almost isothermal so that the loss contribution due to irreversible heat transfer is negligible.

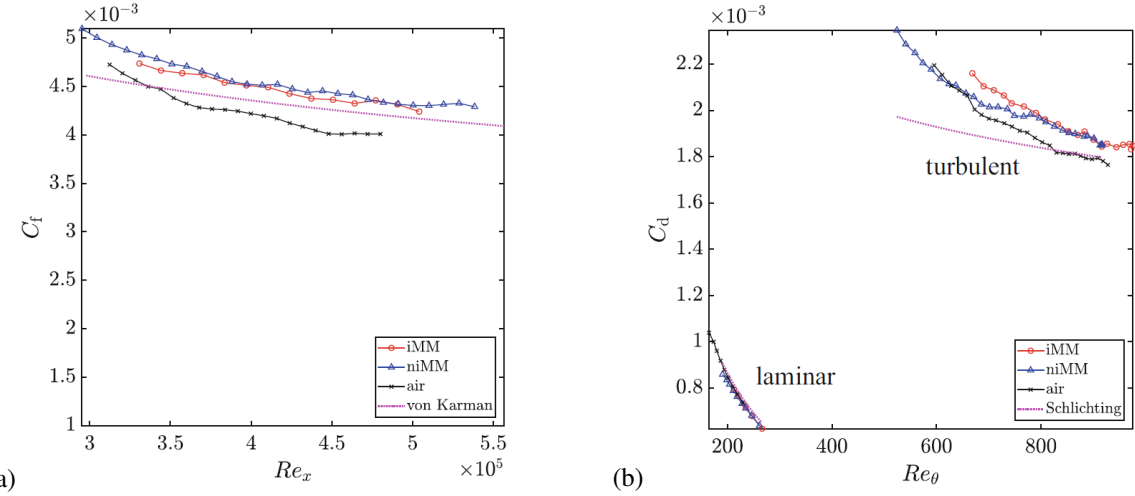


Figure 26: Turbulent boundary layer of MM at  $M=0.9$  (reproduced from [118]): (a) Skin friction coefficient  $C_f$  and (b) dissipation coefficient  $C_d$ .

### 6.5. Compressible flows past cylinders

Circular cylinders at various flow regimes are of interest for many other engineering applications [205, 206]. The incompressible high Reynolds number flow around a smooth circular cylinder has become a classical fluid mechanics problem and has served to develop experimental and numerical methods. On the other hand, the compressible regime has received dimmer attention, even less in the non-ideal gas regime.

Large-eddy simulation of low-Reynolds number flows of cylinders in the high subsonic regime have been recently presented in [158], with the purpose of assisting the calibration of hot-wire anemometry in non-ideal gases. Hot-wire anemometry is a key tool for turbulence research in incompressible flows, and extensions to compressible perfect gas flow exist in the literature, although some controversies persist. An essential step in hot-wire calibration is represented by the determination of the so-called sensitivity coefficients, i.e. the variations of the measured voltage with flow conditions, and particularly their dependency on the flow Reynolds and Mach numbers. Due to the high density and low speed of sound, the application of hot-wire anemometry is particularly challenging for organic vapor flows. The high density of a heavy organic vapor at elevated pressure leads to relatively high wire Reynolds numbers, in combination with significant Mach numbers. In such conditions, little is known about the behavior of sensitivity coefficients or heat transfer properties. For this reasons, high-fidelity numerical simulations were conducted to achieve a better understanding of the heat transfer behavior, and support the experimental work. The thermodynamic and flow inlet quantities were chosen to replicate on average those investigated experimentally with the organic vapor Novec649. The flow conditions corresponded to mildly non-ideal regime: the compressibility factor  $Z$  was slightly below 1, but the fundamental derivative remaining less than 1 throughout most of the flow, leading to non monotonic speed of sound change through compressions and expansions. The cylinder wall was under isothermal conditions to ensure a constant overheat ratio  $T_w/T_\infty = 1.63$ , where  $T_w$  is the wall temperature. With the aim of investigating the effect of Mach number on heat transfer around the cylinder, several flows were simulated with  $M=0.5$ ,  $0.6$  and  $0.7$  at two thermodynamic entry conditions:  $\rho_\infty=27.45 \text{ kg/m}^3$  and  $p_\infty=2.463 \text{ bar}$  (denoted "J"), or  $\rho_\infty=15.71 \text{ kg/m}^3$  and  $p_\infty=1.457 \text{ bar}$  (denoted "A"), corresponding to Reynolds numbers based on the diameter  $D$  of  $Re_D=1240$  and  $717$ , respectively. A strong effect of  $Re$  at quasi-constant  $M$  was observed, the recirculation bubble observed at the higher Reynolds number being approximately 0.6 diameters longer than in the low-Reynolds case. Since both inlet thermodynamic states lie in the weakly non-ideal gas region, the observed changes in the recirculation length were attributed to the different Reynolds. Even at the highest considered inlet Mach number, the fields did not exhibit shockwave formation, due to the increasing speed of sound of the dense gas when undergoing expansion at the aft section of the cylinder (non-ideal gas behavior). The strong overheat ratio contributed to further increase the speed of sound. In Fig.27, we show two instantaneous isosurfaces of the  $Q$ -criterion colored by the vorticity magnitude. For the low-Reynolds case, the flow is three-dimensional but still very coherent in the near wake, with transition starting at a distance of  $2 \div 3$  diameters downstream of the cylinder. For the higher Reynolds, the flow transitions in the

shear layer shortly downstream of the cylinder, which strongly enhances mixing and heat transfer. Overall, the study showed that the wall quantities, and particularly the Nusselt number, were little affected by the Mach number (at least in the considered range) while they were strongly dependent on Reynolds. Finally, the wall-averaged values of the Nusselt number were in close agreement with the measured one, showing that the LES represented a good model for hot-wire studies.

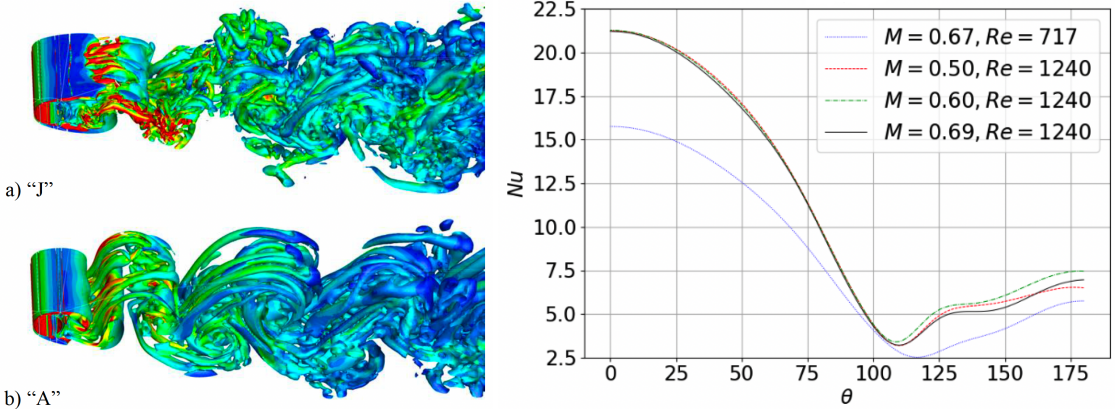


Figure 27: Instantaneous isosurfaces of the  $Q$ -criterion for high-subsonic ( $M = 0.7$ ) and mildly non-ideal Novec649 flows past circular cylinders at  $Re = 1240$  (case "J") and 717 (case "A"), considered for the hot-wire calibration study of [158] (left) and wall-distributions of the Nusselt number for cylinders at various Mach and Reynolds numbers and  $T_w/T_\infty = 1.63$  ( $\theta$  denoted the azimuthal position along the cylinder in degress,  $\theta = 0$  at the front stagnation point). Figures extracted from [158].

With the same spirit, [167] and [157] performed URANS and large eddy simulations of flows past transonic cylinders at  $M=0.7, 0.8, 0.9$  and at high Reynolds numbers of  $Re_D=200000$ . The motivation was twofold. First, flows past circular cylinders can be used as a simplified model for the flow behind the trailing edge of a turbine blade [207], and specifically the coupled dynamics of the wake dynamics and shock system and their influence on turbine losses. These phenomena are of great importance for the design of turbomachinery blades, because they determine the value of the *back pressure*, i.e. the minimal pressure at the rear of the body, which in turn often represents the main contribution to the overall system losses [40]. Second, the simulations were compared with pressure measurements and Backward-Oriented Schlieren (BOS) visualizations obtained in the CLOWT wind tunnel. Such comparisons represent the first-in-the-literature cross-validation of numerical models of flows dominated by viscous effects (flow separation, shock/boundary layer and shock/wake interactions, and unsteady wake dynamics) against experiments in the non-ideal flow regime. As stated above, the physical mechanisms governing transonic flows past circular cylinders are not yet fully understood already for perfect-gas air flow. Indeed, the extreme sensitivity of the flow to the boundary conditions and to the status of the boundary layers and wakes around the so-called "transonic drag divergence" conditions, i.e. conditions such that the drag increases steeply and reaches a maximum under a small increase of the Mach number [208, 209], makes both experimental and numerical investigations rather difficult. In particular, the determination of the "critical" Mach number,  $M_{cr}$  at which drag divergence occurs, is subject to significant uncertainties. In fact, in transonic flow regimes (for Mach numbers  $M \geq 0.6$ ), locally supersonic zones exist in the vicinity of the cylinder, allowing highly unsteady shock waves to form near the walls [210], as well as shocklets in the recirculating flow [211]. Supersonic expansion fans occurring on either sides of the cylinder delay boundary layer separation. This favorable pressure gradient further decreases the pressure on the cylinder surface so that when the flow finally detaches, the back pressure is low, leading to high pressure drag  $C_{d,p}$ . According to the experimental studies in air, the peak drag was measured in the range  $M_{cr} = 0.95 \div 1.0$ . The results were found to be sensitive to the spanwise extent of the cylinder and to blockage effects. The flow topology was also strongly affected by the Mach number but similar topologies did not always correspond to the same Mach number in different experiments, because of flow sensitivity to experimental uncertainties, such as surface roughness and levels of freestream turbulence. The few numerical investigations available in the literature [212, 213] also show a large scatter. Also note that performing numerical simulations at the high characteristic Reynolds numbers encountered in the experimental settings is computationally very demanding, so that the available studies are based on RANS or

coarse RANS/LES or LES. When it comes to consider organic vapor flows, the characteristic Reynolds numbers are even higher because of the gas density, and performing wall-resolved LES is challenging.

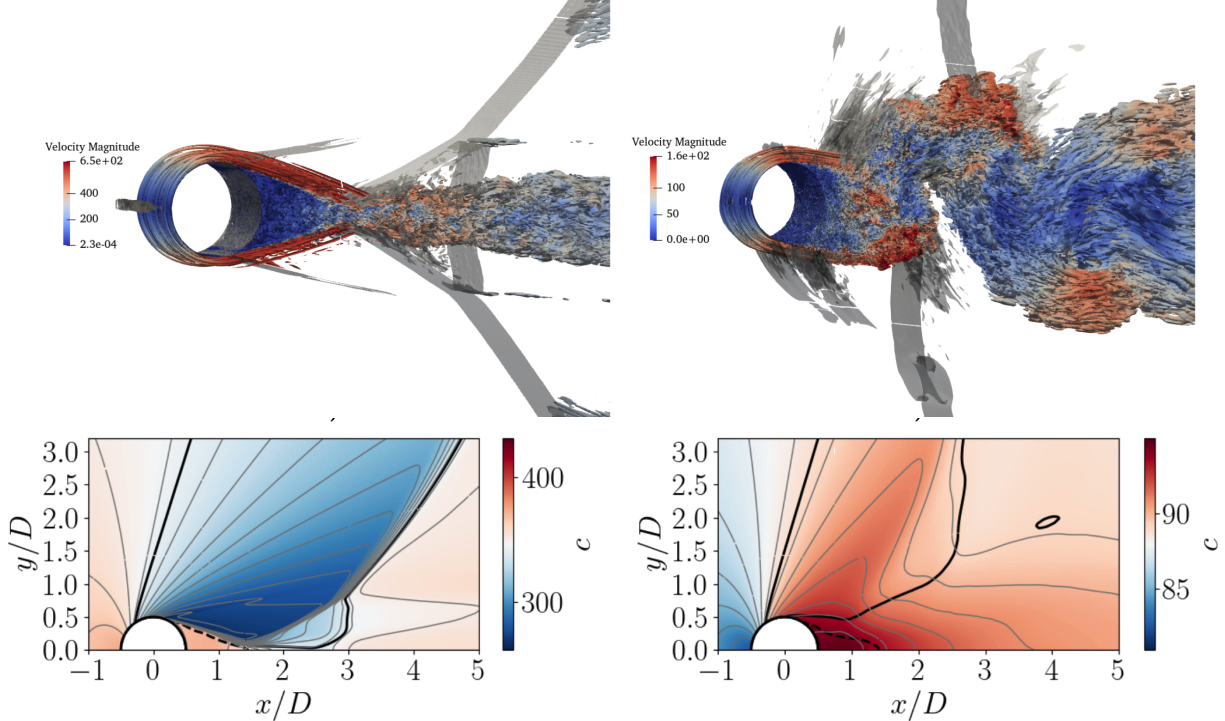


Figure 28: Top line:  $Q$ -criterion iso-contour colored by local velocity magnitude for cylinders at  $M=0.9$  and  $Re_D=200\,000$ ; shock waves are highlighted in grey shadow; left: air, right: Novec649. Bottom line: speed of sound  $c$  mean field and grey contours. The thick black line is the sonic line  $M = 1$ , and the thick black dashed line is the null streamwise velocity component iso-contour  $u = 0$ .

The URANS simulations of [167] showed that organic vapors exhibit significantly higher values of  $C_{d,p}$  over the whole Mach number range, even at nearly-ideal thermodynamic conditions. The reason was found to be the lower back pressure, due to the lower isentropic exponent of the gas. On the other hand, the  $M_{cr}$  was identical to the one in air. Therefore, the thermodynamic behavior of the gas plays a crucial role in the aerodynamic performance of the cylinder in addition to the Mach and Reynolds numbers. Comparisons with experimental data for the wall pressure distribution from CLOWT wind-tunnel experiments using Novec649 as the working fluid showed that the URANS simulations predicted considerably shorter recirculation bubbles than steady RANS simulations at the same conditions, which improved the predicted value of the back pressure coefficients  $C_{p,b}$ . Nevertheless, discrepancies with the experimental data persisted. Note that the experiments were also affected by uncertainties in the cylinder exact cross-sectional shape and roughness. In order to shed light on drag generation mechanisms for transonic flows around cylinders and highlighting the role of the gas properties, a numerical study was presented in [157] using high-fidelity, wall-resolved LES. The simulations were conducted for Novec649 under mildly non-ideal conditions, and compared to air flows at standard conditions. It was shown that the gas properties affect the flow in several ways. Because the fundamental derivative is less than one, the speed of sound increases during the initial expansion of the fluid. As a consequence, the pressure reached on the aft section of the cylinder is lower in the dense gas flow, which results in higher values of the pressure drag, thus higher losses at  $M=0.7$  and  $0.8$  compared to air flows. On the other hand, the local rise in Mach number is limited in the dense gas, so that drag divergence is delayed. Figure 28 shows instantaneous iso-contours of the  $Q$ -criterion for air and Novec649 at  $M=0.9$  (upper panels), as well as time- and span-averaged distributions of the speed of sound, with the sonic line highlighted by black solid lines, and the recirculation region highlighted by black dashed lines (bottom panels). Even at the highest considered Mach number ( $M=0.9$ ), no fish-tail shock system was observed for Novec649, yielding an open wake with strong standing shocks alternatively emanating from the wake as a consequence of vortex shedding, and moving back and forth along the cylinder. In contrast, the air flow exhibits a closed wake with oblique shocks originating at the reattachment point, indicating that the divergence drag regime has

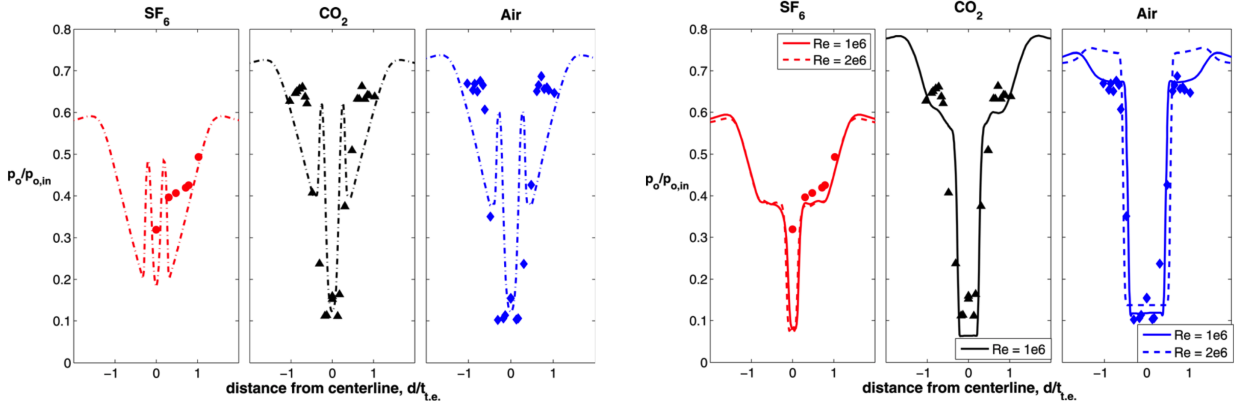


Figure 29: Comparisons of total pressure profiles across the wake behind a supersonic thick trailing edge. Symbols denote experiments. Left: RANS; right: wall-modeled LES. Extracted from [31]

established. This results in higher losses for air. Because of the similarities between a circular cylinder and a turbine blade trailing edge, the losses were calculated using the Denton loss decomposition [40], specifically into entropy generation inside the boundary layer, and profile and momentum losses. In the case of the organic vapor, the thermal boundary layer has little effect on the dynamic one and self-heating is largely weakened, due to the high heat capacity, in agreement with previous works. It was found that transonic vortex shedding, responsible for wake thickening, is the main contributor to momentum loss and should essentially be suppressed to increase the cylinder performance.

### 6.6. ORC turbine configurations

Turbomachinery flows are generally characterized by complex phenomena, such as transition, separation, and non-equilibrium flow conditions involving strong pressure gradients, rotation and streamline curvature (see e.g. [214]). However, due to the dominant use of RANS calculations in non-ideal turbomachinery studies, the influence of these phenomena on turbine performance has remained largely unexplored. Computations of ORC turbine cascades based on higher-fidelity models have been reported in the literature for the first time by Durá Galiana and Wheeler [31], with the aim of investigating trailing-edge loss mechanisms in ORC turbines. The trailing-edge flow is strongly dependent on Mach number and can account for a third of the total stage losses [40], making the trailing-edge region critical for turbine efficiency. For turbine vanes with supersonic exit flow, expansion fans are generated on either side of the trailing edge as the flow accelerates and turns around the trailing edge. This generally produces a separation bubble behind the trailing edge followed by a confluence region, where shock waves are produced as the flows from either side of the blade/vane meet and turn in a shared direction. According to the expansion intensity, recirculation bubble size, and shock topology and intensity, an open or a closed wake is generated (similar to what is observed for cylinder flows), and vortex shedding is produced. In an inviscid flow of a gas with  $\Gamma > 1$ , such as air, supersonic expansions are limited by a maximum turning angle, set by the asymptotic behavior of the Prandtl–Meyer function as the Mach number approaches infinity. On the other hand, in an inviscid flow of a gas with  $\Gamma < 1$  the Prandtl–Meyer function changes because of the low equivalent isentropic exponent of dense gases [28], resulting in no limit to the Prandtl–Meyer function as Mach number increases. The separation point around the trailing-edge is then determined by viscous effects, and therefore dependent on the Reynolds number. Overall, a higher turning angle and higher acceleration is expected in dense gases compared to light ones. To better understand the effects of trailing edge shape on the shock system and wake dynamics, Durá Galiana and Wheeler [31] performed a combined experimental and numerical study. In a first series of experiments, they considered a thick flat plate with a truncated trailing edge, placed in the divergent of a supersonic nozzle. Experiments were run with various fluids, including fluorocarbon SF<sub>6</sub>, and compared with RANS and wall-modelled LES (Smagorinsky model). The calculations used the commercial code FLUENT14.5 and a grid of approximately  $4 \times 10^6$  points, with near-wall resolution corresponding to  $\Delta y^+ \geq 30$ . The flow Reynolds number based on exit conditions was up to  $2 \times 10^6$ . Despite the rather coarse grid, LES captured total pressure profiles across the wake much more accurately than RANS, providing a reasonably good estimate of the

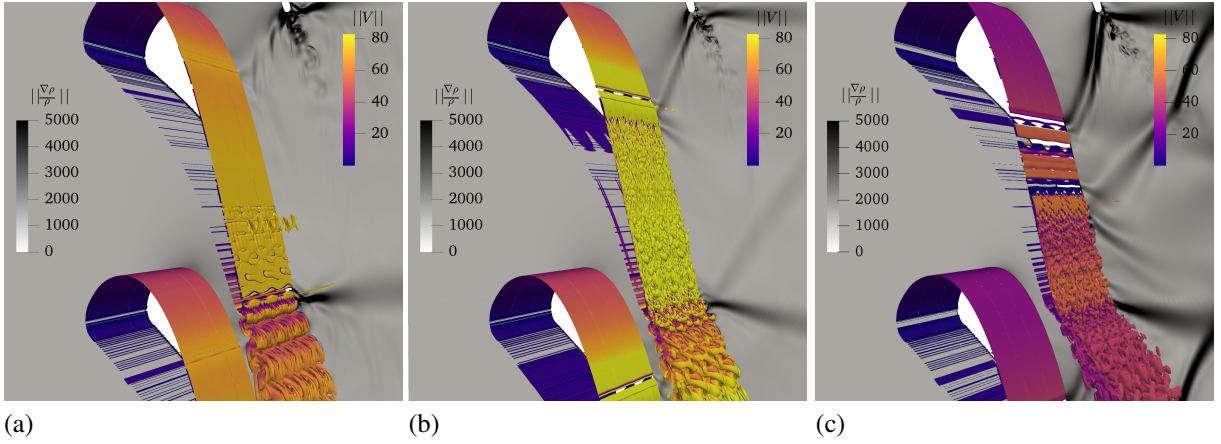


Figure 30: Instantaneous iso-surface of the Q-criterion ( $Q = 1000 \text{ s}^{-1}$ ) colored by the velocity magnitude (m/s), replicated three times in the spanwise direction, and snapshot of the relative density gradient in the background for cases IC1-LPR (a), IC1-HPR (b), and IC2-LPR (c). Extracted from [215]

wake thickness and maximum total pressure loss (see Fig.29). For fluids with low  $\Gamma$ , the recirculation bubble behind the trailing edge was smaller, confirming that the flow turning angle is higher in dense gases. The maximum Mach number reached in the flow was also lower than in lighter gases, as expected for  $\Gamma < 1$ . Afterwards, the authors studied a supersonic centripetal turbine stator using experiments, RANS and wall-modeled LES. Their results show that, despite the rather coarse grid, the LES solution deviates from the RANS one significantly, shedding doubts about the reliability of RANS models employed in ORC design. In particular, entropy generation patterns and loss coefficients considerably differed in RANS and LES. The authors concluded that higher-fidelity models are needed to better design the blade geometry near the trailing edge.

The first wall-resolved LES were presented in [215] for PP11 flow through a transonic turbine nozzle vane, for two inlet thermodynamic conditions, corresponding to subcritical and supercritical pressure (called respectively IC1 and IC2), and two pressure ratios (LPR, HPR). The geometry corresponds to the VKI LS-89 configuration, widely investigated in the literature for air flows. Due limitations in the maximum grid resolution, the flow Reynolds number (based on exit conditions) was limited to the range  $1.13 \times 10^6 \div 2.26 \times 10^6$ . For the subcritical conditions IC1, only mild non-ideal gas dynamic effects were observed. On the contrary, dramatic deviations from the ideal-gas behavior were present for the supercritical operating conditions and the lower pressure ratio, including non-classical expansion and compression waves interacting with the surrounding boundary layers and wakes. The study also showed that the flow remained laminar over most of the blade surface (at least at the moderate Reynolds number considered in the study), and laminar-to-turbulent transition was induced by shock/boundary layer interactions. Overall 3D views of the three LES are shown in Fig. 30. For some operating conditions, transition led to abrupt changes in boundary layer thickness, resulting in the formation of additional shock waves. Such waves cannot be captured neither by inviscid flow simulations, nor by RANS simulations, for which the boundary layers are fully turbulent. Another important finding was that, in contrast with theoretical predictions based on inviscid flow, the supercritical inlet operating conditions (characterized by significant BZT effects) do not lead to an improvement of cascade losses, showing the importance of accounting for the contribution of viscous losses to the cascade performance.

In the frame of a Franco-German project aiming at understanding loss mechanisms in ORC turbines (ANR-DFG project REGAL-ORC, "REal-GAs effects on loss mechanisms of ORC turbine flows"), a joint experimental/numerical investigation of turbine blade geometries has been undertaken. In preparation of detailed experiments to be undertaken in the closed-loop organic-vapor wind tunnel CLOWT at FH Muenster, an idealized turbine blade geometry has been studied numerically in [216]. The configuration had been studied previously by Passmann *et al.* [217] using air as the working fluid. The study considered Novec649 at an inlet Mach number of 0.52, and mildly non-ideal thermodynamic conditions ( $\rho_{in}/\rho_c=0.07$ ,  $p_{in}/p_c=0.17$ ,  $\Gamma_{in}=0.8$ ). The vane accelerated the flow to supersonic exit conditions ( $M_2 \approx 1.6$ ), reaching an exit Reynolds number (based on blade chord) equal to  $8.5 \times 10^6$ . The extremely high Reynolds number makes wall-resolved LES computationally unreachable (approximately 100 billions grid points are

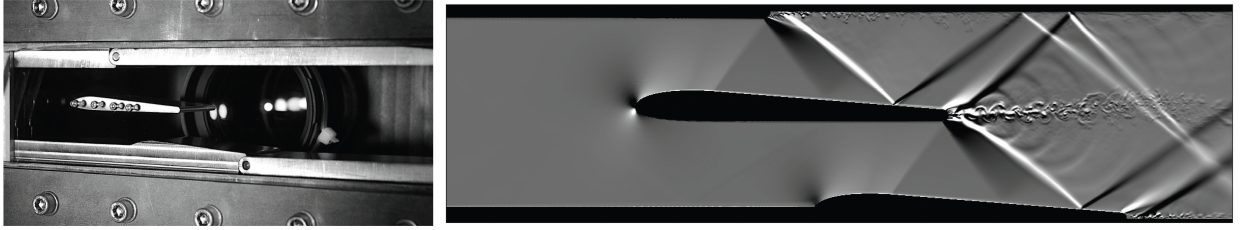


Figure 31: View of the idealized turbine vane experiment (left) and numerical pseudo-Schlieren picture from DDES-SLA [216]

estimated to be necessary to resolve the full domain), so hybrid RANS/LES simulations were performed instead, using the DDES-SLA model. Figure 31 shows a close-up view of the test section in the experimental setup and a numerical pseudo-Schlieren picture of the flow field at midspan. The upper and bottom walls of the test section have been profiled to obtain a nearly-periodic flow. The gas accelerates through the vane, reaching supersonic conditions shortly after turning around the trailing edge. The flow further expands around the rounded trailing edge, and oblique shock waves originate at the point where the trailing edge recirculation bubble closes. The simulation captures the large structures in the wake and in the upper and lower boundary layers, downstream of the rounded backward facing steps. The dense gas flow is characterized by a significant emission of acoustic waves originating from vortex shedding, a phenomenon that remains much more limited in air flow. As expected in DDES, the attached boundary layers are simulated in the RANS mode, so that no structures are visible. Large vortices are shed behind the blade, with a Strouhal number of about 0.55. While the flow through the vane is little affected by the turbulence model in use, the study showed that the trailing losses are strongly dependent on the coupled trailing edge shocks/wake dynamics, and that the loss coefficient predicted by URANS simulations is 20% lower than in DDES. Comparisons with air also confirm that the flow turning angle around the trailing edge and the size of the recirculation bubble are smaller in Novec649, as previously discussed in [31]. Experimental data will be hopefully available within the next year, allowing a detailed comparison of the wake turbulent properties and loss coefficients with measurements.

Moving toward more realistic ORC turbine vanes, recent research efforts have attempted to reproduce a recent experiment conducted at University of Cambridge [218], corresponding to an annular supersonic turbine vane. Various fluids were used in the experiments, including refrigerant R134a. At the experimental conditions, the high pressure ratio of about 4.4 induces exit Mach and Reynolds numbers of approximately 1.45 and  $1.7 \times 10^6$ , respectively. Based on standard estimates of wall-resolved LES requirements, more than one billion grid points would be necessary to simulate the full configuration (including the upper and bottom walls). For this reason, in [219] a simplified configuration, corresponding to a 2D section extracted at the turbine shroud and extruded in the spanwise direction. The simulation used a tenth-order scheme and a mesh of  $780 \times 10^6$  points. At the suction side, the simulation highlighted the presence of leading-edge separation, transition to turbulence, and relaminarization due to the strong favorable pressure gradient downstream of the vane throat. The flow then transitions again to turbulence as it interacts with impinging shocks generated at the trailing edge of the adjacent blade. The trailing-edge flow exhibits the classical fishtail shock system, and the wake is fully turbulent. Overall, the simulations show that the flow is highly transitional, and that RANS models widespread in industrial practice for ORC turbine design might be providing over-optimistic estimates of the loss coefficients. Due to the highly twisted geometry of the turbine vane, the 2D simulations exhibited discrepancies with the available experimental measurements of total pressure losses. In [150], two LES (wall-modeled and wall-resolved) were conducted using a lower exit Reynolds number of 500 000. The grids contained 400 and 450 millions cells, respectively. Figure 32 provides a view of the turbulent structures developing along the suction side, represented through an isosurface of the  $Q$ -criterion. Contrary to the 2D simulations, transition to turbulence occurs at an earlier position in the vane divergent, because of the interaction with secondary flows emanating from the connection of the blades with the shroud. Although the simulations capture the overall trend of the pressure loss profile downstream of the blade, full quantitative agreement could not be obtained, and further investigations are in progress. Additional high-fidelity simulations have been undertaken for a linear supersonic cascade by Wheeler et al. [220] and compared with RANS solutions obtained using various CFD solvers. Better converged results and analyses are expected in the near future.

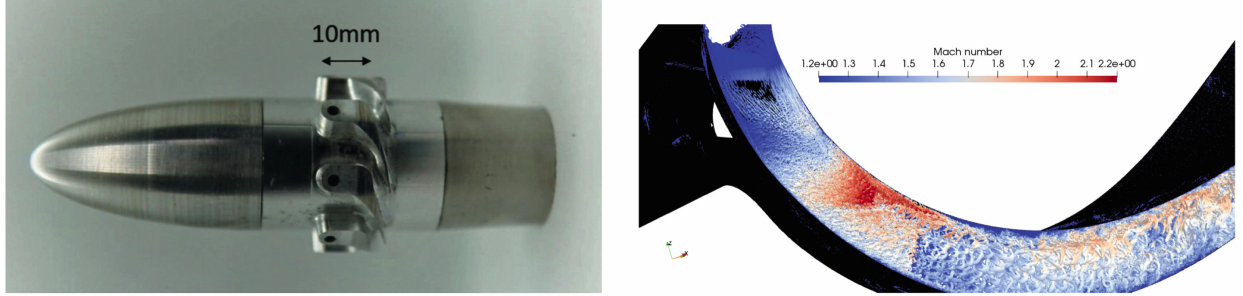


Figure 32: Picture of the annular cascade [218] (left) and visualisation of the turbulent structures at the suction side using the  $Q$ -criterion colored with the Mach number [150].

## 7. Conclusions

The recent use of high-fidelity numerical simulations of non-ideal gas flows has contributed to elucidate the influence of the thermodynamic and thermophysical gas properties on laminar-to-turbulent transition, compressible turbulence, and the development of turbulent boundary layers, mixing layers, and wakes.

For gases with sufficiently high molecular complexity, the heat capacity is high, leading to a decoupling of dynamical and thermal effects. This profoundly alters the hydrodynamic stability properties, introducing effects reminiscent of those observed in strongly wall-cooled airflows: the mean flow properties remain closer to those of the corresponding incompressible flows, while the stability region is enlarged because of energy drained by activation of the vibrational modes of the molecules. Due to the low characteristic sound speed of molecularly complex organic compounds, acoustic modes are also enhanced, with the appearance of supersonic unstable modes and radiating Mach waves. For transitional boundary layer flows, the enhanced flow stability (at fixed Reynolds number) disadvantages ordered modal transition and favors instead transition scenarios dominated by transient growth and energy exchange among modes. This finally leads to the formation of unstable sinuous streaks through the lift-up mechanisms, and eventually breakdown to turbulence. In free-stream turbulence induced scenarios, the rapid growth of the local Reynolds number in heavy gases causes the formation of clusters of small structures than are transported and sheared by larger structures, a situation that is not observed in air flows at the same inlet conditions.

Strongly non-ideal or non-classical gas dynamic effects have also been shown to strongly affect turbulent flow statistics in idealized configurations, such as homogeneous isotropic turbulence and turbulent mixing layers. In the first case, probability density functions are modified, with expansion events being enhanced, and compression events weakened compared to airflows. In the second case, the growth rate is reduced and remains closer to incompressible flow conditions, and turbulent fluctuations along the axis are strongly enhanced. For wall-bounded flows, thermodynamic non-idealities are less influential than high-Reynolds-number effects induced by the elevated fluid density and/or density-dependent transport properties. Liquid-like viscosity behavior in dense gases was documented for turbulent channel flow and turbulent boundary layers. In all these cases, the first- and second-order velocity statistics remain similar to those observed in incompressible flows, even at very high characteristic Mach numbers. Despite that, genuine compressibility effects are present, including high levels of the density fluctuations close to the wall, and the emission of acoustic waves in the external flow.

More recently, the focus of research has moved toward more realistic geometries and thermodynamic conditions, often encountered in engineering applications, and specifically in turbomachinery components for energy conversion systems. High-fidelity simulations have shed light into the important role played by laminar-to-turbulent transition, even at the high Reynolds numbers encountered in non-ideal gas turbomachinery. This phenomenon, largely neglected by designers (who rely mostly on RANS models), affects the nature of shock/boundary layer interactions and the wake dynamics and, ultimately, the turbine losses. Of note, RANS models might underestimate the actual losses, thus providing an over-optimistic estimate of the actual performance.

The simulations provide useful databases for the assessment and improvement of turbulence models (an essential ingredient for flow design). The development of improved wall-modeled LES or hybrid RANS/LES approaches and of suitable transition models is also critical to a better description of unsteady flow phenomena.

Therefore, it seems to be of primary importance to promote the upgrading of design tools for non-ideal gas turbomachinery towards higher fidelity models (a process that has already started for classical turbomachinery such as gas and steam turbines). The significant extra cost of high-fidelity simulations can be reduced by implementing the models on modern GPU architectures and by adopting multi-fidelity design strategies. This will certainly be the focus of intensive research efforts in the near future.

## Acknowledgments

This research has been funded by the Agence Nationale de la Recherche through the ANR-20-CE92-0019-02 project Regal-ORC. This work was granted access to the HPC resources of IDRIS and TGCC under the allocations A0112A01736 and A0132A01736 made by GENCI (Grand Equipement National de Calcul Intensif).

## References

- [1] J. Hoffren, T. Talonpoika, J. Larjola, T. Siikonen, Numerical simulation of real-gas flow in a supersonic turbine nozzle ring, *ASME J. Eng. Gas Turbines Power* 124 (2) (2002) 395–403.
- [2] B. Brown, B. Argrow, Application of Bethe-Zel'dovich-Thompson fluids in organic Rankine cycle engines, *J. Prop. Power* 16 (6) (2000) 1118–1124.
- [3] J. Monaco, M. Cramer, L. Watson, Supersonic flows of dense gases in cascade configurations, *J. Fluid Mech.* 330 (1997) 31–59.
- [4] G. Angelino, C. Invernizzi, Supercritical heat pump cycles., *Int. J. Refrig.* 17 (8) (1994) 543–554.
- [5] C. Zamfirescu, I. Dincer, Performance investigation of high-temperature heat pumps with various BZT working fluids, *Thermochimica Acta* 488 (1-2) (2009) 66–77.
- [6] N. Kirillov, Analysis of modern natural gas liquefaction technologies, *Chem. Petrol. Eng.* 40 (7-8) (2004) 401–406.
- [7] Proceedings of the 1st International Seminar on Non-Ideal Compressible-Fluid Dynamics for Propulsion & Power, Vol. 821 of *J. Phys.: Conf. Ser.*, IOP Sciences, 2017.
- [8] F. di Mare, A. Spinelli, M. Pini (Eds.), Selected Contributions from the 2nd International Seminar on Non-Ideal Compressible Fluid Dynamics for Propulsion and Power, NICFD 2018, October 4-5, 2018, Bochum, Germany, Lecture Notes in Mechanical Engineering, Springer Cham, 2020.
- [9] M. Pini, C. De Servi, A. Spinelli, F. di Mare, A. Guardone (Eds.), Proceedings of the 3rd International Seminar on Non-Ideal Compressible Fluid Dynamics for Propulsion and Power, NICFD 2020, ERCOFTAC Series, Springer Cham, 2021.
- [10] M. White, T. El Samad, I. Karathanassis, A. Sayma, M. Pini, A. Guardone (Eds.), Proceedings of the 4th International Seminar on Non-Ideal Compressible Fluid Dynamics for Propulsion and Power, NICFD 2022, Vol. 29 of ERCOFTAC Series, Springer Cham, 2023.
- [11] R. Miller, K. Harstad, J. Bellan, Direct numerical simulations of supercritical fluid mixing layers applied to heptane-nitrogen, *J. Fluid Mech.* 436 (2001) 1–39.
- [12] N. Okong'o, J. Bellan, Direct numerical simulation of a transitional supercritical binary mixing layer: heptane and nitrogen, *J. Fluid Mech.* 464 (2002) 1–34.
- [13] J. Bae, J. Yoo, H. Choi, Direct numerical simulation of turbulent supercritical flows with heat transfer, *Phys. Fluids* 17 (10) (2005) 105104.
- [14] H. Nemat, A. Patel, B. Boersma, R. Pecnik, Mean statistics of a heated turbulent pipe flow at supercritical pressure, *International Journal of Heat and Mass Transfer* 83 (2015) 741–752.
- [15] S. Kawai, Heated transcritical and unheated non-transcritical turbulent boundary layers at supercritical pressures, *J. Fluid Mech.* 865 (2019) 563–601.
- [16] G. H. Schnerr, S. Adam, K. Lanzenberger, R. Schulz, Computational Fluid Dynamics Review, John Wiley & Sons, Chichester, England, 1995, Ch. Multiphase flows: Condensation and cavitation, pp. 614–640.
- [17] A. White, A comparison of modelling methods for polydispersed wet-steam flow, *Int. J. Numer. Meth. Eng.* 57 (2003) 819–834.
- [18] N. A. Okong'o, J. Bellan, Consistent large-eddy simulation of a temporal mixing layer laden with evaporating drops. part 1. direct numerical simulation, formulation and a priori analysis, *J. Fluid Mech.* 499 (2004) 1–47.
- [19] W. Wróblewski, S. Dykas, A. Gepert, Steam condensing flow modeling in turbine channels, *International Journal of Multiphase Flow* 35 (6) (2009) 498–506.
- [20] P. Post, M. Sembritzky, F. di Mare, Towards scale resolving computations of condensing wet steam flows, in: ASME Turbo Expo 2019, Vol. GT2019-91269, 2019, p. V008T29A023.
- [21] A. Gaurdone, L. Vigevano, Roe linearization for the van der Waals gas, *J. Comput. Phys.* 175 (1) (2002) 50–78.
- [22] P. Colonna, S. Rebay, Numerical simulation of dense gas flows on unstructured grids with an implicit high resolution upwind Euler solver, *Int. J. Numer. Meth. Fl.* 2004 (46) 735–765.
- [23] P. Cinnella, P. Congedo, Numerical solver for dense gas flows, *AIAA J.* 43 (2005) 2458–61.
- [24] M. Pini, S. Vitale, P. Colonna, G. Gori, A. Guardone, T. Economou, J. Alonso, F. Palacios, SU2: the open-source software for non-ideal compressible flows, *J. Phys.: Conf. Ser.* 821 (1) (2017) 012013.
- [25] E. Mantecca, A. Colombo, A. Ghidoni, G. Noventa, D. Pasquale, S. Rebay, On the development of an implicit discontinuous Galerkin solver for turbulent real gas flows, *MDPI Fluids* 8 (4) (2023) 117.
- [26] J. Harinck, P. Colonna, A. Guardone, S. Rebay, Influence of thermodynamic models in two-dimensional flow simulations of turboexpanders, *ASME J. Turbomachinery* 132 (1) (2010) 011001.

- [27] L. Sciacovelli, P. Cinnella, Numerical study of multistage transcritical organic Rankine cycle axial turbines, *ASME J. Eng. Gas Turbines Power* 136 (8) (2014) 082604.
- [28] A. Wheeler, J. Ong, The role of dense gas dynamics on organic Rankine cycle turbine performance, *ASME J. Eng. Gas Turbines Power* 135 (10) (2013) 102603.
- [29] D. Wilcox, *Turbulence Modeling for CFD*, DCW Industries, 2006.
- [30] F. Alshammari, A. Pesyridis, A. Karvountzis-Kontakiotis, B. Franchetti, Y. Pesmazoglou, Experimental study of a small scale organic Rankine cycle waste heat recovery system for a heavy duty diesel engine with focus on the radial inflow turbine expander performance, *Applied Energy* 215 (2018) 543–555.
- [31] F. Durá Galiana, A. Wheeler, J. Ong, A study of trailing-edge losses in organic Rankine cycle turbines, *ASME J. Turbomachinery* 138 (12) (2016) 121003.
- [32] A. Spinelli, G. Cammi, S. Gallarini, M. Zocca, F. Cozzi, P. Gaetani, V. Dosseña, A. Guardone, Experimental evidence of non-ideal compressible effects in expanding flow of a high molecular complexity vapor, *Experiments in Fluids* 59 (2018) 126.
- [33] M. C. Robertson, P. J. Newton, T. Chen, R. F. Martinez-Botas, Development and commissioning of a blowdown facility for dense gas vapours, in: *Turbo Expo: Power for Land, Sea, and Air*, Vol. 58608, American Society of Mechanical Engineers, 2019, p. V003T28A002.
- [34] F. Reinker, E. Kenig, M. Passmann, S. aus der Wiesche, Closed loop organic wind tunnel (CLOWT): Design, components and control system, *Energy Procedia* 129 (2017) 200–207, IV International Seminar on ORC Power Systems, ORC2017 13–15 September 2017, Milano, Italy.
- [35] A. Head, Novel experiments for the investigation of non-ideal compressible fluid dynamics: the ORCHID and first results of optical measurements, Ph.D. thesis, TU Delft (2021).
- [36] X. Gloerfelt, A. Bianner, P. Cinnella, High-subsonic boundary-layer flows of an organic vapour, *J. Fluid Mech.* 971 (2023) A8.
- [37] S. aus der Wiesche, Experimental investigation techniques for non-ideal compressible fluid dynamic, *International Journal of Turbomachinery Propulsion and Power* 8 (2) (2023) 11.
- [38] M. Zocca, A. Guardone, G. Cammi, F. Cozzi, A. Spinelli, Experimental observation of oblique shock waves in steady non-ideal flows, *Experiments in Fluids* 60 (2019) 101.
- [39] G. Gori, M. Zocca, G. Cammi, A. Spinelli, P. M. Congedo, A. Guardone, Accuracy assessment of the non-ideal computational fluid dynamics model for siloxane mdm from the open-source su2 suite, *European Journal of Mechanics-B/Fluids* 79 (2020) 109–120.
- [40] J. Denton, Loss mechanisms in turbomachines, *ASME J. Turbomachinery* 115 (1993) 621.
- [41] B. Zappoli, D. Bailly, Y. Garrabos, B. Le Neindre, P. Guenoun, D. Beysens, Anomalous heat transport by the piston effect in supercritical fluids under zero gravity, *Physical Review A* 41 (4) (1990) 2264.
- [42] N. Okong'o, J. Bellan, Small-scale dissipation in binary-species, thermodynamically supercritical, transitional mixing layers, *Comp Fluids* 39 (2010) 1112–1124.
- [43] L. Selle, T. Schmitt, Large-eddy simulation of single-species flows under supercritical thermodynamic conditions, *Combustion Science and Technology* 182 (4-6) (2010) 392–404.
- [44] M. Tanahashi, Y. Tominaga, M. Shimura, K. Hashimoto, T. Miyauchi, DNS of supercritical carbon dioxide turbulent channel flow, in: *Progress in Wall Turbulence: Understanding and Modeling*, Springer, 2011, pp. 429–436.
- [45] U. Sengupta, H. Nemati, B. Boersma, R. Pecnik, Fully compressible low-mach number simulations of carbon-dioxide at supercritical pressures and trans-critical temperatures, *Flow Turbulence Combust.* 99 (2017) 909–931.
- [46] Y. Cao, R. Xu, J. Yan, S. He, P. Jiang, Direct numerical simulation of convective heat transfer of supercritical pressure CO<sub>2</sub> in a vertical tube with buoyancy and thermal acceleration effects, *J. Fluid Mech.* 927 (2021) A29.
- [47] W. Wang, S. He, C. Moulinec, D. R. Emerson, Direct numerical simulation of thermal stratification of supercritical water in a horizontal channel, *Comp Fluids* 261 (2023) 105911.
- [48] J. Y. Yoo, The turbulent flows of supercritical fluids with heat transfer, *Ann. Rev. Fluid Mech.* 45 (2012) 495–525.
- [49] S. Elghobashi, Direct numerical simulation of turbulent flows laden with droplets or bubbles, *Ann. Rev. Fluid Mech.* 51 (2019) 217–244.
- [50] T. Trummler, S. J. Schmidt, N. A. Adams, Investigation of condensation shocks and re-entrant jet dynamics in a cavitating nozzle flow by large-eddy simulation, *International Journal of Multiphase Flow* 125 (2020) 103215.
- [51] P. Post, B. Winhart, F. di Mare, Large eddy simulation of a condensing wet steam turbine cascade, *ASME J. Eng. Gas Turbines Power* 143 (2) (2021) 021016.
- [52] M. Cramer, Nonclassical dynamics of classical gases, *Nonlinear waves in real fluids* (1991) 91–145.
- [53] R. Menikoff, B. Plohr, The Riemann problem for fluid flow of real materials, *Reviews of Modern Physics* 61 (1989) 75–130.
- [54] P. Cinnella, P. Congedo, Inviscid and viscous aerodynamics of dense gases, *J. Fluid Mech.* 580 (2007) 179–217.
- [55] J. Harinck, A. Guardone, P. Colonna, The influence of molecular complexity on expanding flows of ideal and dense gases, *Phys. Fluids* 21 (8) (2009) 086101.
- [56] P. Thompson, A fundamental derivative in gas dynamics, *Phys. Fluids* 14 (1971) 1843–1849.
- [57] M. Cramer, L. Best, Steady, isentropic flows of dense gases, *Phys. Fluids A* 3 (4) (1991) 219–226.
- [58] H. A. Bethe, The Theory of Shock Waves for an Arbitrary Equation of State, Tech. Rep. 545, Office of Scientific Research and Development (1942).
- [59] Y. B. Zel'Dovich, Y. P. Raizer, *Physics of Shock Waves and High-Temperature Hydrodynamic Phenomena*, Academic, New York, 1966.
- [60] M. Cramer, A. Kluwick, On the propagation of waves exhibiting both positive and negative nonlinearity, *J. Fluid Mech.* 142 (1) (1984) 9–37.
- [61] M. Cramer, Shock splitting in single-phase gases, *J. Fluid Mech.* 199 (1989) 281–296.
- [62] Z. Rusak, C.-W. Wang, Transonic flow of dense gases around an airfoil with a parabolic nose, *J. Fluid Mech.* 346 (1997) 1–21.
- [63] N. Chandrasekaran, T. Michelis, B. Mercier, P. Colonna, Preliminary experiments in high temperature vapours of organic fluids in the asymmetric shock tube for experiments on rarefaction waves (ASTER), in: M. White, T. El Samad, I. Karathanassis, A. Sayma, M. Pini, A. Guardone (Eds.), *Proceedings of the 4th International Seminar on Non-Ideal Compressible Fluid Dynamics for Propulsion and Power (NICFD 2022)*, Vol. 29 of *ERCOFTAC series*, Springer, 2023, pp. 181–190.
- [64] M. Cramer, Negative nonlinearity in selected fluorocarbons, *Phys. Fluids A* 1 (11) (1989) 1894–1897.
- [65] J. Van der Waals, Over de continuïteit van den gas-en vloeistofoestand (on the continuity of the gas and liquid state), Ph.D. thesis, University

of Leiden (1873).

- [66] P. Thompson, K. Lambakis, Negative shock waves, *J. Fluid Mech.* 60 (1) (1973) 187–208.
- [67] M. Cramer, R. Sen, Exact solutions for sonic shocks in van der Waals gases, *Phys. Fluids* 30 (2) (1987) 377–385.
- [68] M. Cramer, G. Tarkenton, Transonic flows of Bethe-Zel'dovich-Thompson fluids, *J. Fluid Mech.* 240 (1992) 197–228.
- [69] M. Cramer, R. Fry, Nozzle flows of dense gases, *Phys. Fluids A* 5 (5) (1993) 1246–1259.
- [70] C.-W. Wang, Z. Rusak, Numerical studies of transonic BZT gas flows around thin airfoils, *J. Fluid Mech.* 396 (1999) 109–141.
- [71] Z. Rusak, C.-W. Wang, Low-drag airfoils for transonic flow of dense gases, *Zeitschrift für angewandte Mathematik und Physik ZAMP* 51 (3) (2000) 467–480.
- [72] M. Cramer, A. Crickenberger, The dissipative structure of shock waves in dense gases, *J. Fluid Mech.* 223 (1991) 325–355.
- [73] M. Cramer, S. Whitlock, G. Tarkenton, Transonic and boundary layer similarity laws in dense gases, *ASME J. Fluids Eng.* 118 (3) (1996) 481–485.
- [74] M. Cramer, S. Park, On the suppression of shock-induced separation in Bethe-Zel'dovich-Thompson fluids, *J. Fluid Mech.* 393 (1999) 1–21.
- [75] A. Kluwick, Internal flows of dense gases, *Acta Mechanica* 169 (2004) 123–143.
- [76] A. Kluwick, A. Wrabel, Shock boundary layer interactions in dense gases, *Proc. Appl. Math. Mech.* 4 (2004) 444–445.
- [77] A. Kluwick, G. Meyer, Shock regularization in dense gases by viscous-inviscid interactions, *J. Fluid Mech.* 644 (2010) 473–507.
- [78] A. Kluwick, G. Meyer, Viscous-inviscid interactions in transonic flows through slender nozzles, *J. Fluid Mech.* 672 (2011) 487–520.
- [79] T. Chung, M. Ajlan, L. Lee, K. Starling, Generalized multiparameter correlation for nonpolar and polar fluid transport properties, *Industrial & Engineering Chemistry Research* 27 (4) (1988) 671–679.
- [80] P. Colonna, A. Guardone, Molecular interpretation of nonclassical gas dynamics of dense vapors under the van der Waals model, *Phys. Fluids* 18 (2006) 056101.
- [81] L. Sciacovelli, P. Cinnella, X. Gloerfelt, Direct numerical simulations of supersonic turbulent channel flows of dense gases, *J. Fluid Mech.* 821 (2017) 153–199.
- [82] E. Lemmon, M. Huber, M. McLinden, NIST standard reference database 23: Reference fluid thermodynamic and transport properties – REFPROP, Version 9.1., <http://www.nist.gov/srd/nist23.cfm> (2013).
- [83] R. Span, W. Wagner, E. W. Lemmon, R. T. Jacobsen, Multiparameter equations of state – recent trends and future challenges, *Fluid Phase Equilibr.* 183–184 (2001) 1 – 20.
- [84] E. Lemmon, R. Jacobsen, A new functional form and new fitting techniques for equations of state with application to pentafluoroethane (HFC-125), *J. Phys. Chem. Ref. Data* 34 (1) (2005) 69–108.
- [85] R. Span, W. Wagner, Equations of state for technical applications. I. Simultaneously optimized functional forms for nonpolar and polar fluids, *Int. J. Thermophys.* 24 (2003) 1–39.
- [86] R. Span, W. Wagner, Equations of state for technical applications. II. Results for nonpolar fluids, *Int. J. Thermophys.* 24 (2003) 41–109.
- [87] R. Span, W. Wagner, Equations of state for technical applications. III. Results for polar fluids, *Int. J. Thermophys.* 24 (2003) 111–162.
- [88] E. Lemmon, R. Span, Short fundamental equations of state for 20 industrial fluids, *J. Chem. Eng. Data* 51 (3) (2006) 785–850.
- [89] P. Colonna, N. Nannan, A. Guardone, E. Lemmon, Multiparameter equations of state for selected siloxanes, *Fluid Phase Equilibr.* 244 (2) (2006) 193 – 211.
- [90] P. Colonna, A. Guardone, N. Nannan, Siloxanes: A new class of candidate Bethe-Zel'dovich-Thompson fluids, *Phys. Fluids* 19 (086102) (2007).
- [91] P. Colonna, N. Nannan, A. Guardone, Multiparameter equations of state for siloxanes:  $[(\text{CH}_3)_3\text{-Si-O}_{1/2}]_2\text{-}[\text{O-Si-(CH}_3)_2]_{i=1,\dots,3}$ , and  $[\text{O-Si-(CH}_3)_2]_6$ , *Fluid Phase Equilibr.* 263 (2) (2008) 115 – 130.
- [92] F. A. Aly, L. L. Lee, Self-consistent equations for calculating the ideal gas heat capacity, enthalpy, and entropy, *Fluid Phase Equilibria* 6 (3-4) (1981) 169–179.
- [93] K. Marsh, R. Wilhoit, M. Frenkel, D. Yin, The thermodynamic properties of substances in the ideal gas state, *Thermodynamics Research Center* (1994).
- [94] O. Redlich, J. Kwong, On the thermodynamics of solutions. V. An equation of state. Fugacities of gaseous solutions, *Chem. Rev.* 44 (1) (1949) 233–244.
- [95] D.-Y. Peng, D. Robinson, A new two-constant equation of state, *Industrial and Engineering Chemistry Fundamentals* 15 (1) (1976) 59–64.
- [96] J. Martin, Y.-C. Hou, Development of an equation of state for gases, *AIChE Journal* 1 (2) (1955) 142–151.
- [97] M. Benedict, G. B. Webb, L. C. Rubin, An empirical equation for thermodynamic properties of light hydrocarbons and their mixtures I. Methane, ethane, propane and n-butane, *The Journal of Chemical Physics* 8 (4) (1940) 334–345.
- [98] B. Poling, J. Prausnitz, J. O'Connell, *The properties of gases and liquids*, 5th Edition, McGraw-Hill, New York, USA, 2001.
- [99] R. Stryjek, J. Vera, PRSV: An improved Peng-Robinson equation of state for pure compounds and mixtures, *The Canadian Journal of Chemical Engineering* 64 (2) (1986) 323–333.
- [100] A. Guardone, L. Vigevano, B. Argrow, Assessment of thermodynamic models for dense gas dynamics, *Phys. Fluids* 16 (11) (2004) 3878–3887.
- [101] P. Neufeld, A. Janzen, R. Aziz, Empirical equations to calculate 16 of the transport collision integrals  $\omega(l, s)^*$  for the Lennard-Jones (12-6) potential, *J. Chem. Phys.* 57 (1972) 1100–1102.
- [102] O. Marxen, T. Magin, G. Iaccarino, E. Shaqfeh, A high-order numerical method to study hypersonic boundary-layer instability including high-temperature gas effects, *Phys. Fluids* 23 (8) (2011) 084108.
- [103] B. Franzelli, B. Fiorina, N. Darabiha, A tabulated chemistry method for spray combustion, *Proceedings of the Combustion Institute* 34 (1) (2013) 1659–1666.
- [104] M. Pini, A. Spinelli, G. Persico, S. Rebay, Consistent look-up table interpolation method for real-gas flow simulations, *Comp. Fluids* 107 (2015) 178–188.
- [105] P. Boncinelli, F. Rubechini, A. Arnone, M. Cecconi, C. Cortese, Real gas effects in turbomachinery flows: A computational fluid dynamics model for fast computations, *ASME J. Turbomachinery* 126 (2004) 268–276.

- [106] E. Rinaldi, R. Pecnik, P. Colonna, Exact Jacobians for implicit Navier–Stokes simulations of equilibrium real gas flows, *J. Comput. Phys.* 270 (2014) 459–477.
- [107] A. Rubino, M. Pini, M. Kosec, S. Vitale, P. Colonna, A look-up table method based on unstructured grids and its application to non-ideal compressible fluid dynamic simulations, *Journal of Computational Science* 28 (2018) 70–77.
- [108] C. Scherding, G. Rigas, D. Sipp, P. J. Schmid, T. Sayadi, Data-driven framework for input/output lookup tables reduction: Application to hypersonic flows in chemical nonequilibrium, *Physical Review Fluids* 8 (2) (2023) 023201.
- [109] M. Pini, A. Giuffré, A. Cappiello, M. Majer, E. Bunshoten, Data-driven regression of thermodynamic models in entropic form, in: M. White, T. El Samad, I. Karathanassis, A. Sayma, M. Pini, A. Guardone (Eds.), *Proceedings of the 4th International Seminar on Non-Ideal Compressible Fluid Dynamics for Propulsion and Power (NICFD 2022)*, Vol. 29 of *ERCOFTAC series*, Springer, 2023, pp. 22–34.
- [110] S. Hercus, P. Cinnella, Robust shape optimization of uncertain dense gas flows through a plane turbine cascade, *ASME-JSME-KSME* (2011) Paper AJK2011-05007.
- [111] P. Congedo, C. Corre, P. Cinnella, Numerical investigation of dense-gas effects in turbomachinery, *Comp Fluids* 49 (2011) 290–301.
- [112] R. Abgrall, P. Congedo, D. De Santis, N. Razaaly, A non-linear residual distribution scheme for real-gas computations, *Comp Fluids* 102 (2014) 148–169.
- [113] A. Giauque, C. Corre, M. Menghetti, Direct numerical simulations of homogeneous isotropic turbulence in a dense gas, in: *J. Phys.: Conf. Ser.*, Vol. 821, 2017, p. 012017.
- [114] S. Kawai, H. Terashima, H. Negishi, A robust and accurate numerical method for transcritical turbulent flows at supercritical pressure with an arbitrary equation of state, *J. Comput. Phys.* 300 (2015) 116–135.
- [115] L. Sciacovelli, P. Cinnella, C. Content, F. Grasso, Dense gas effects in inviscid homogeneous isotropic turbulence, *J. Fluid Mech.* 800 (2016) 140–179.
- [116] E. Touber, N. Alferez, Shock-induced energy conversion of entropy in non-ideal fluids, *J. Fluid Mech.* 864 (2019) 807–847.
- [117] A. Biennier, X. Glaerfelt, P. Cinnella, Assessment of a high-order implicit residual smoothing time scheme for multiblock curvilinear meshes, *11th International Conference on Computational Fluid Dynamics (ICCFD11) 11-15 July, Maui, HI, USA* (2022).
- [118] F. Tosto, A. Wheeler, M. Pini, High fidelity simulations and modelling of dissipation in boundary layers of non-ideal fluid flows, in: M. White, T. El Samad, I. Karathanassis, A. Sayma, M. Pini, A. Guardone (Eds.), *Proceedings of the 4th International Seminar on Non-Ideal Compressible Fluid Dynamics for Propulsion and Power. NICFD 2022*, Vol. 29 of *ERCOFTAC series*, Springer, 2023, pp. 62–71.
- [119] E. Mantecca, A. Colombo, A. Ghidoni, G. Noventa, D. Pasquale, S. Rebay, On the development of an implicit discontinuous galerkin solver for turbulent real gas flows, *Fluids* 8 (4) (2023) 117.
- [120] P. Roe, Approximate Riemann solvers, parameter vectors, and difference schemes, *J. Comput. Phys.* 43 (2) (1981) 357–372.
- [121] P. Glaister, An approximate linearised Riemann solver for the Euler equations for real gases, *J. Comput. Phys.* 74 (2) (1988) 382–408.
- [122] M. Vinokur, J.-L. Montagné, Generalized flux-vector splitting and Roe average for an equilibrium real gas, *J. Comput. Phys.* 89 (2) (1990) 276–300.
- [123] L. Mottura, L. Vigevano, M. Zaccanti, An evaluation of Roe’s scheme generalizations for equilibrium real gas flows, *J. Comput. Phys.* 138 (2) (1997) 354–399.
- [124] P. Cinnella, Roe-type schemes for dense gas flow computations, *Comp Fluids* 35 (10) (2006) 1264–1281.
- [125] D. Vimercati, A. Guardone, On the numerical simulation of non-classical quasi-1D steady nozzle flows: capturing sonic shocks, *Applied Mathematics and Computation* 319 (2018) 617–632.
- [126] J.-C. Hoarau, P. Cinnella, X. Glaerfelt, Large eddy simulation of turbomachinery flows using a high-order implicit residual smoothing scheme, *Comp Fluids* 198 (2020) 104395.
- [127] A. Arnone, Viscous analysis of three-dimensional rotor flow using a multigrid method, *ASME J. Turbomachinery* 116 (3) (1994) 435–445.
- [128] A. Jameson, W. Schmidt, E. Turkel, Numerical solutions of the Euler equations by finite volume methods using Runge–Kutta time-stepping schemes, *AIAA Paper 81-1259* (1981).
- [129] A. Harten, P. D. Lax, B. v. Leer, On upstream differencing and godunov-type schemes for hyperbolic conservation laws, *SIAM Review* 25 (1) (1983) 35–61.
- [130] R. Abgrall, Residual distribution schemes: current status and future trends, *Comp Fluids* 35 (7) (2006) 641–669.
- [131] S. Lele, Compact finite difference schemes with spectral-like resolution, *J. Comput. Phys.* 103 (1992) 16–42.
- [132] T. Schonfeld, M. Rudgyard, Steady and unsteady flow simulations using the hybrid flow solver AVBP, *AIAA J.* 37 (11) (1999) 1378–1385.
- [133] O. Colin, M. Rudgyard, Development of high-order Taylor–Galerkin schemes for LES, *J. Comput. Phys.* 162 (2) (2000) 338–371.
- [134] F. Palacios, J. Alonso, K. Duraisamy, M. Colonno, J. Hicken, A. Aranake, A. Campos, S. Copeland, T. Economou, A. Lonkar, et al., Stanford university unstructured (su 2): an open-source integrated computational environment for multi-physics simulation and design, in: 51st AIAA aerospace sciences meeting including the new horizons forum and aerospace exposition, 2013, p. 287.
- [135] C. Tam, J. Webb, Dispersion-relation-preserving finite difference schemes for computational acoustics, *J. Comput. Phys.* 107 (1993) 262–281.
- [136] S. Kawai, S. Lele, Localized artificial diffusivity scheme for discontinuity capturing on curvilinear meshes, *J. Comput. Phys.* 227 (22) (2008) 9498–9526.
- [137] P.-Y. Outtier, C. Content, P. Cinnella, B. Michel, The high-order dynamic computational laboratory for CFD research and applications, 21st AIAA Computational Fluid Dynamics Conference, 24–27 June, Dallas, Texas, *AIAA Paper 2013-2439* (2013).
- [138] L. Duan, Q. Zheng, Z. Jiang, J. Wang, Dense gas effect on small-scale structures of compressible isotropic turbulence, *Phys. Fluids* 33 (2021) 115113.
- [139] T. Chen, B. Yang, M. C. Robertson, R. F. Martinez-Botas, Direct numerical simulation of real-gas effects within turbulent boundary layers for fully-developed channel flows, *Journal of the Global Power and Propulsion Society* 5 (2021) 216–232.
- [140] X. Li, Y. Ma, D. Fu, Dns and scaling law analysis of compressible turbulent channel flow, *Science in China Series A: Mathematics* 44 (2001) 645–654.
- [141] D. Fu, Y. Ma, A high order accurate difference scheme for complex flow fields, *Journal of Computational physics* 134 (1) (1997) 1–15.
- [142] A. P. Wheeler, R. D. Sandberg, N. D. Sandham, R. Pichler, V. Michelassi, G. Laskowski, Direct numerical simulations of a high-pressure

- turbine vane, ASME J. Turbomachinery 138 (7) (2016) 071003.
- [143] J. W. Kim, R. D. Sandberg, Efficient parallel computing with a compact finite difference scheme, Comp Fluids 58 (2012) 70–87.
- [144] F. Bassi, L. Botti, A. Colombo, A. Crivellini, N. Franchina, A. Ghidoni, Assessment of a high-order accurate discontinuous galerkin method for turbomachinery flows, International Journal of Computational Fluid Dynamics 30 (4) (2016) 307–328.
- [145] L. Sciacovelli, P. Cinnella, F. Grasso, Small-scale dynamics of dense gas compressible homogeneous isotropic turbulence, J. Fluid Mech. 825 (2017) 515–549.
- [146] L. Sciacovelli, X. Gloerfelt, D. Passiatore, P. Cinnella, F. Grasso, Numerical investigation of high-speed turbulent boundary layers of dense gases, Flow Turbulence Combust. 105 (2020) 555–579.
- [147] A. Giauque, C. Corre, A. Vadrot, Direct numerical simulations of forced homogeneous isotropic turbulence in a dense gas, J. Turbulence 21 (3) (2020) 186–208.
- [148] A. Vadrot, A. Giauque, C. Corre, Analysis of turbulence characteristics in a temporal dense gas compressible mixing layer using direct numerical simulation, J. Fluid Mech. 893 (2020) A10.
- [149] A. Vadrot, A. Giauque, C. Corre, Direct numerical simulations of temporal compressible mixing layers in a Bethe–Zel'dovich–Thompson dense gas: influence of the convective Mach number, J. Fluid Mech. 922 (2021) A5.
- [150] A. Giauque, A. Vadrot, C. Corre, Development, validation and application of an ANN-based large eddy simulation subgrid-scale turbulence model for dense gas flows, in: M. Pini, C. De Servi, A. Spinelli, F. di Mare, A. Guardone (Eds.), Proceedings of the 3rd International Seminar on Non-Ideal Compressible Fluid Dynamics for Propulsion and Power (NICFD 2020), ERCOFTAC series, Springer, 2021, pp. 43–52.
- [151] E. Touber, Small-scale two-dimensional turbulence shaped by bulk viscosity, J. Fluid Mech. 875 (2019) 974–1003.
- [152] P. Cinnella, C. Content, High-order implicit residual smoothing time scheme for direct and large eddy simulations of compressible flows, J. Comput. Phys. 277 (2016) 72–100.
- [153] J. Wang, L.-P. Wang, Z. Xiao, Y. Shi, S. Chen, A hybrid numerical simulation of isotropic compressible turbulence, J. Comput. Phys. 229 (13) (2010) 5257–5279.
- [154] B. Yang, T. Chen, R. Martinez-Botas, Bypass laminar-turbulent transition on a flat plate of organic fluids using DNS method, in: M. White, T. El Samad, I. Karathanassis, A. Sayma, M. Pini, A. Guardone (Eds.), Proceedings of the 4th International Seminar on Non-Ideal Compressible Fluid Dynamics for Propulsion and Power (NICFD 2022), Vol. 29 of ERCOFTAC series, Springer, 2023, pp. 53–61.
- [155] A. Biennner, X. Gloerfelt, P. Cinnella, L. Hake, S. aus der Wiesche, S. Strehle, Study of bypass transition in dense-gas boundary layers, in: 12th International Symposium on Turbulence and Shear Flow Phenomena (TSFP12), Osaka, Japan, 2022, pp. 1–6.
- [156] A. Biennner, X. Gloerfelt, P. Cinnella, Leading-edge effects in freestream turbulence induced transition in a dense gas flow, 13th Direct and Large-Eddy Simulations (DLES13) 26–28 October, Udine, Italy (2022).
- [157] C. Matar, P. Cinnella, X. Gloerfelt, S. Sundermeier, L. Hake, S. aus der Wiesche, Numerical investigation of the transonic non-ideal gas flow around a circular cylinder at high Reynolds number, 13th Direct and Large-Eddy Simulations (DLES13) 26–28 October, Udine, Italy (2022).
- [158] L. Hake, S. aus der Wiesche, S. Sundermeier, L. Cakievski, J. Bäumer, P. Cinnella, C. Matar, X. Gloerfelt, Hot-wire anemometry in high subsonic organic vapor flows, ASME J. Turbomachinery 145 (2023) 091010.
- [159] K. Thompson, Time dependent boundary conditions for hyperbolic systems, J. Comput. Phys. 68 (1987) 1–24.
- [160] N. Okong'o, J. Bellan, Consistent boundary conditions for multicomponent real gas mixtures based on characteristic waves, J. Comput. Phys. 176 (2002) 330–344.
- [161] C. Tam, Z. Dong, Radiation and outflow boundary conditions for direct computation of acoustic and flow disturbances in a nonuniform mean flow, J. Comput. Acous. 4 (2) (1996) 175–201.
- [162] F. Menter, Improved two-equation  $k-\omega$  turbulence models for aerodynamic flows, Technical Memorandum 103975, NASA (1992).
- [163] P. Spalart, S. Allmaras, A one-equation turbulence model for aerodynamic flows, in: 30th aerospace sciences meeting and exhibit, 1992, p. 439.
- [164] B. Baldwin, H. Lomax, Thin-layer approximation and algebraic model for separated turbulentflows, in: 16th aerospace sciences meeting, 1978, p. 257.
- [165] E. Rinaldi, R. Pecnik, P. Colonna, Unsteady operation of a highly supersonic organic Rankine cycle turbine, ASME J. Turbomachinery 138 (12) (2016) 121010.
- [166] B. Obert, P. Cinnella, Comparison of steady and unsteady RANS CFD simulation of a supersonic ORC turbine, Energy Procedia 129 (2017) 1063–1070.
- [167] C. Matar, P. Cinnella, X. Gloerfelt, F. Reinker, S. aus der Wiesche, Investigation of non-ideal gas flows around a circular cylinder, Energy 268 (2023) 126563.
- [168] J. Smagorinsky, General circulation experiments with the primitive equations: I. the basic experiment, Mon. Weath. Rev. 91 (1963) 99–163.
- [169] F. Nicoud, F. Ducros, Subgrid-scale stress modelling based on the square of the velocity gradient tensor, Flow Turbulence Combust. 62 (3) (1999) 183–200.
- [170] C. Zhang, Z. Yuan, L. Duan, Y. Wang, J. Wang, Dynamic iterative approximate deconvolution model for large-eddy simulation of dense gas compressible turbulence, Phys. Fluids 34 (12) (2022).
- [171] G. Aubard, P. Stefanin Volpiani, X. Gloerfelt, J.-C. Robinet, Comparison of subgrid-scale viscosity models and selective filtering strategy for large-eddy simulations, Flow Turbulence Combust. 91 (3) (2013) 497–518.
- [172] X. Gloerfelt, P. Cinnella, Large eddy simulation requirements for the flow over periodic hills, Flow Turbulence Combust. 103 (2019) 55–91.
- [173] M. L. Shur, P. R. Spalart, M. K. Strelets, A. K. Travin, An enhanced version of DES with rapid transition from RANS to LES in separated flows, Flow Turbulence Combust. 95 (2015) 709–737.
- [174] A. Chakravarthy, Investigation of dense gas effects on transition to turbulence over a flat plate boundary layer, Master's thesis, Delft University of Technology (supervised by R. Pecnik, J. Ren & O. Marxen) (2018).
- [175] X. Gloerfelt, J.-C. Robinet, L. Sciacovelli, P. Cinnella, F. Grasso, Dense gas effects on compressible boundary layer stability, J. Fluid Mech. 893 (2020) A19.

- [176] J. Ren, O. Marxen, R. Pecnik, Boundary-layer stability of supercritical fluids in the vicinity of the Widom line, *J. Fluid Mech.* 871 (2019) 831–864.
- [177] J. Ren, S. Fu, R. Pecnik, Linear instability of Poiseuille flows with highly non-ideal fluids, *J. Fluid Mech.* 859 (2019) 89–125.
- [178] R. Govindarajan, K. Sahu, Instabilities in viscosity-stratified flow, *Ann. Rev. Fluid Mech.* 46 (2014) 331–353.
- [179] B. Saika, A. Ramachandran, K. Sinha, R. Govindarajan, Effects of viscosity and conductivity stratification on the linear stability and transient growth within compressible Couette flow, *Phys. Fluids* 29 (2017) 024105.
- [180] A. Kluwick, Interacting laminar boundary layers of dense gases, *Acta Mechanica [Suppl.]* 4 (1994) 335–349.
- [181] A. Kluwick, Non-ideal compressible fluid dynamics: a challenge for theory, *J. Phys.: Conf. Ser.* 821 (1) (2017) 012001.
- [182] L. Mack, Boundary layer linear stability theory, *Tech. rep.* 709, AGARD (1984).
- [183] N. Bitter, J. Shepherd, Stability of highly cooled hypervelocity boundary layers, *J. Fluid Mech.* 778 (2015) 586–620.
- [184] C. Knisely, X. Zhong, Sound radiation by supersonic unstable modes in hypersonic blunt cone boundary layers. I. Linear stability theory, *Phys. Fluids* 31 (2019) 024103.
- [185] A. Fedorov, A. Tumin, High-speed boundary-layer instability: old terminology and a new framework, *AIAA J.* 49 (8) (2011) 1647–1657.
- [186] J. Ren, S. Fu, Study of the discrete spectrum in a Mach 4.5 Görtler flow, *Flow Turbulence Combust.* 94 (2015) 339–357.
- [187] X. Gloerfelt, L. Sciacovelli, P. Cinnella, F. Grasso, Supersonic-mode transition in a dense-gas boundary layer at Mach 6, *3rd International Seminar on Non-Ideal Compressible-Fluid Dynamics for Propulsion & Power (NICFD2020), 29-30 October, Delfs, Netherlands* (2020).
- [188] K. Franko, S. Lele, Breakdown mechanisms and heat transfer overshoot in hypersonic zero pressure gradient boundary layers, *J. Fluid Mech.* 730 (2013) 491–532.
- [189] L. Hake, S. aus der Wiesche, S. Sundermeier, A. Biennner, X. Gloerfelt, P. Cinnella, Grid-generated decaying turbulence in an organic vapour flow, in: M. White, T. El Samad, I. Karathanassis, A. Sayma, M. Pini, A. Guardone (Eds.), *Proceedings of the 4th International Seminar on Non-Ideal Compressible Fluid Dynamics for Propulsion and Power (NICFD 2022)*, Vol. 29 of ERCOFTAC series, Springer, 2023, pp. 181–190.
- [190] P. Durbin, X. Wu, Transition beneath vortical disturbances, *Ann. Rev. Fluid Mech.* 39 (2007) 107–128.
- [191] T. Zaki, From streaks to spots and on to turbulence: exploring the dynamics of boundary layer transition, *Flow Turbulence Combust.* 91 (2013) 451–473.
- [192] J. A. Redford, N. D. Sandham, G. T. Roberts, Numerical simulations of turbulent spots in supersonic boundary layers: effects of Mach number and wall temperature, *Progr. Aerosp. Sci.* 52 (2012) 67–79.
- [193] T. Passot, A. Pouquet, Numerical simulation of compressible homogeneous flows in the turbulent regime, *J. Fluid Mech.* 181 (1987) 441–466.
- [194] M. Lesieur, *Turbulence in fluids, Fluid Mechanics and its Applications*, Springer, Dordrecht, 2008.
- [195] A. Patel, J. Peeters, B. Boersma, R. Pecnik, Semi-local scaling and turbulence modulation in variable property turbulent channel flows, *Phys. Fluids* 27 (9) (2015) 095101.
- [196] E. Van Driest, Turbulent boundary layer in compressible fluids, *Journal of the Aeronautical Sciences* 18 (3) (1951) 145–160.
- [197] A. Trettel, J. Larsson, Mean velocity scaling for compressible wall turbulence with heat transfer, *Phys. Fluids* 28 (2) (2016) 026102.
- [198] L. Sciacovelli, P. Cinnella, X. Gloerfelt, A priori tests of RANS models for turbulent channel flows of a dense gas, *Flow Turbulence Combust.* 101 (2) (2018) 295–315.
- [199] X. Wu, P. Moin, Direct numerical simulation of turbulence in a nominally zero-pressure-gradient flat-plate boundary layer, *J. Fluid Mech.* 360 (2009) 5–41.
- [200] C. Wenzel, B. Selent, M. Kloker, U. Rist, DNS of compressible turbulent boundary layers and assessment of data/scaling-law quality, *J. Fluid Mech.* 842 (2018) 428–468.
- [201] P. Schlatter, R. Örlü, Assessment of direct numerical simulation data of turbulent boundary layers, *J. Fluid Mech.* 659 (2010) 116–126.
- [202] F. Pizzi, Development and assesment of physical based profile loss model for ORC turbine based on boundary layer analysis, Master's thesis, Politecnico di Milano (supervised by P. Gaetani & M. Pini) (2017).
- [203] D. Dijkshoorn, Simulation of two-dimensional steady state boundary layers applied to nonideal gas flows, Master's thesis, Delft University of Technology (supervised by C. De Servi, A. Head & R. Pecnik) (2020).
- [204] M. Pini, C. De Servi, Entropy generation in laminar boundary layers of non-ideal fluid flows, in: F. di Mare, A. Spinelli, M. Pini (Eds.), *Selected Contributions from the 2nd International Seminar on Non-Ideal Compressible Fluid Dynamics for Propulsion and Power, NICFD 2018*, Springer, 2020, pp. 104–117.
- [205] E. Achenbach, Distribution of local pressure and skin friction around a circular cylinder in cross-flow up to  $Re = 5 \times 10^6$ , *J. Fluid Mech.* 34 (1968) 625–639.
- [206] M. Zdravkovich, *Flow around Circular Cylinders. Fundamentals*, Vol. 1, Oxford University Press, Oxford, 1997.
- [207] C. H. Sieverding, M. Stanislaski, J. Snoeck, The Base Pressure Problem in Transonic Turbine Cascades, *Journal of Engineering for Power* 102 (1980) 711–718.
- [208] F. Gowen, E. Perkins, Drag of circular cylinders for a wide range of Reynolds numbers and Mach numbers, RM A52C20, NACA (1953).
- [209] J. Macha, Drag of circular cylinders at transonic Mach numbers, *Journal of Aircraft* 14 (6) (1977) 605–607.
- [210] O. Rodriguez, The circular cylinder in subsonic and transonic flow, *AIAA J.* 22 (12) (1984) 1713–1718.
- [211] R. Hong, Z. Xia, Y. Shi, Z. Xiao, S. Chen, Constrained large-eddy simulation of compressible flow past a circular cylinder, *Communication Computational Physics* 15 (2) (2014) 388–421.
- [212] C. Xu, L. Chen, X. Lu, Effect of Mach number on transonic flow past a circular cylinder, *Chinese Science Bulletin* 54 (2009) 1886–1893.
- [213] Z. Xia, Z. Xiao, Y. Shi, S. Chen, Mach number effect of compressible flow around a circular cylinder, *AIAA J.* 54 (6) (2016) 2004–2009.
- [214] R. D. Sandberg, V. Michelassi, Fluid dynamics of axial turbomachinery: Blade-and stage-level simulations and models, *Ann. Rev. Fluid Mech.* 54 (2022) 255–285.
- [215] J.-C. Hoarau, P. Cinnella, X. Gloerfelt, Large eddy simulations of strongly non-ideal compressible flows through a transonic cascade, *Energies* 14 (3) (2021) 772.
- [216] A. Biennner, X. Gloerfelt, P. Cinnella, L. Hake, S. aus der Wiesche, High-fidelity simulation of a transonic dense gas flow over an idealized

- blade vane configuration, in: ORC2023 - 7th International Seminar on Organic Rankine Cycle Power Systems, Seville, Spain, 2023, pp. 1–8.
- [217] M. Passman, Experimentelle untersuchungen zu transsonischen schaufel-spaltströmungen in axialturbinen, Ph.D. thesis, Universität der Bundeswehr Hamburg (2021).
  - [218] D. Baumgärtner, J. Otter, A. Wheeler, The effect of isentropic exponent on transonic turbine performance, ASME J. Turbomachinery 142 (8) (2020) 081007.
  - [219] C. Matar, P. Cinnella, X. Gloerfelt, Large eddy simulation of a dense organic vapor flow through a supersonic turbine vane, in: ETMM14 - 14th International ERCOFTAC Symposium on Engineering Turbulence Modelling and Measurements, Barcelona, Spain, 2023, pp. 1–6.
  - [220] A. S. Wheeler, High-fidelity simulations of dense vapor flows, in: Proceedings of PARCFD 2022, 25-27 May, Alba, Italy, 2022, p. Paper 39.

## Graphical Abstract

**Insights into the turbulent flow of dense gases through high-fidelity simulations**

P. Cinnella, X. Gloerfelt

## Highlights

### **Insights into the turbulent flow of dense gases through high-fidelity simulations**

P. Cinnella, X. Gloerfelt

- Recent works on high-fidelity simulations of dense gas flows are reviewed
- An overview of numerical methods and models for dense gases is also provided
- Focus is on numerical solvers using high-order methods and advanced modeling
- High-fidelity models play a crucial role for the physical understanding of dense gas turbulence and for future improved design